Fabrication and Overgrowth of Semi-polar and Non-polar GaN on Sapphire for Advanced III-nitride Optoelectronics

By Kun Xing

A Thesis Submitted for the Degree of Doctor of Philosophy (Ph.D.)

Department of Electronic and Electrical Engineering

The University of Sheffield

March, 2015

Abstract

Fabrication of nano-rod and micro-rod array templates and then overgrowth of semi-polar (11-22) and non-polar (11-20) GaN on the templates on sapphire have been performed. Two simple but cost-effective fabrication techniques based on self-organized nano-masks and ultraviolet (UV) photolithography approaches have been developed, respectively. Optimization in the fabrication of non-/semi-polar nano-rod structures and semi-polar micro-rod structures has been systematically performed. The GaN nano-rod and micro-rod arrays with high reproducibility and good uniformity across two inch wafers have been achieved.

Metal organic chemical vapour deposition (MOCVD) has been employed to conduct GaN overgrowth on the semi-polar or non-polar GaN nano-rod array templates which are fabricated based on standard semi-polar or non-polar GaN on r-plane (for non-polar) or m-plane (for semi-polar) sapphire prepared using MOCVD. Great improvements in crystal quality for both semi-polar and non-polar GaN have been achieved, which have been confirmed by both x-ray and transmission electron microscopy (TEM) measurements. It has been found that the diameter of nano-rods plays a significant role in reducing dislocation density. With increasing diameter of nano-rods, the dislocation density of the overgrown GaN is reduced. By using the self-organized masks, a quick coalescence with a less than 1 μm thick layer has been achieved, which is much less than those using any conventional overgrowth techniques (typically 10-20 μm).

An approach to the fabrication of semi-polar micro-rod GaN array structures has been developed, which is based on the combination of mask design and UV photolithography techniques. A systematic study on the overgrowth of semi-polar GaN on the semi-polar micro-rod GaN array structures have been performed as a function of the diameter of the micro-rods. A further reduction in the dislocation densities and especially basal stacking faults has been achieved compared with that using self-organized nano-mask approach.

The mechanism for defect reduction in the GaN overgrown on nano-rod/micro-rod templates has been investigated by detailed TEM studies. The dislocations are either terminated by the SiO_2 masks or the residue voids formed due to the large GaN lateral growth rate. The propagation of basal stacking fault can be blocked during the coalescence initiated from the sidewall of the adjacent nano-rods or micro-rods.

InGaN/GaN multiple quantum wells (MQWs) have been grown on the semi-polar and non-polar overgrown GaN, respectively. The temperature dependent photoluminescence (PL) measurements demonstrate a significant enhancement in the internal quantum efficiency of InGaN/GaN MQWs grown on the overgrown GaN compared with that grown on as-grown c-plane, non-polar, and semi-polar GaN, respectively, as a result of the huge improvement in crystal quality and elimination or mitigation of the quantum confined Stark effect, which has been confirmed by excitation power dependent PL measurements.

InGaN/GaN MQWs with a significant enhancement in indium incorporation have been achieved, demonstrating a major advantage of utilisation of semi-polar GaN for the growth of long wavelength emitters. So far, high optical performance with an emission wavelength of up to 590 nm has been demonstrated.

Acknowledgements

It has been a great honour for me to spend four years in the UK's pioneering research group on Nitrides and working in the EPSRC national centre for III-V technologies. During these times, there are a number of people who offered me great help and support, without whom this work could not have been completed. Therefore, I wish to take this opportunity to express my sincere gratitude to everyone mentioned here.

First and foremost, I would like to show my deepest appreciation to my supervisor, Professor Tao Wang for providing me with this great opportunity to pursue my interest and dreams, and for always giving me constant courage and full guidance during the research. I was amazed by his enduring enthusiasm for scientific exploration and depth of knowledge. Without his support, the work could not have been possible. More importantly, I cannot say thank you enough for spending a huge amount of valuable time changing my personality and making me form a good habit when performing the scientific research. I believe these experiences are the most precious treasure in my whole life.

I would like to especially thank Dr. Jie Bai for training me to operate a variety of device fabrication machines and fabricate the nano-/micro-structures, and for proofreading this PhD thesis. She is a highly accomplished scientist and I have learnt a great deal from her, not just the knowledge, but the attitude towards work and life.

I am very much indebted to Dr. Yipin Gong for training me to operate the MOCVD and use the XRD, AFM and PL system. I am also very grateful to him for teaching me the MOCVD growth skills. When I started to change my project orientation to the nanostructure fabrication, I am very thankful to him for growing many samples for me. His great help makes my work go much more smoothly.

I would like to acknowledge Dr. Yaonan Hou for providing me with great ideas and experiences in the nanostructure fabrication, and without him I would have struggled to fabricate the high quality and reproducible nanostructures. In addition, I owe a big thank you for proofreading the thesis for me.

There are some people who closely work with me on the project, Mr. Yu Xiang, Mr. Benbo Xu, Mr. Qingping Zeng, Mr. Ling Jiu, Mr. Shuoheng Shen and Mr. Zhi Li. I am very grateful

to work with them. It has always been very good to have discussion with them and share opinions and experiences. Especially I want to thank Mr. Yu Xiang and Mr. Benbo Xu for providing various experimental results for my thesis. The thesis cannot have been completed without your help.

I am very fortunate to work in the MOCVD growth lab and device fabrication lab as a team, and it was my pleasure to share the experiences with our team members: Dr. Bin Liu, Dr. Taeki Kim, Dr. Paul Renwick, Dr. Richard Smith, Dr. Jon Benton, Mr. Medestos Athanasiou, Mr. Fernando, Miss. Tang Hao and Mr. Yun Zhang. Thank you all for broadening my horizons and approach things in a different way.

Many thanks go to Mr. Paul Haines for maintaining and fixing the MOCVD system, all the fabrication machines and characterization systems in the cleanroom, and for teaching me to solve some technical problems of the machines.

I owe a special thank you to Dr. Ken Kennedy, Dr. Rob Airey and Mr. Jon Milner for giving me some good tips of using the fabrication machines, and for performing the device lab maintenance.

I wish to thank David Morris for performing the cleanroom induction for me, thank you also to Mrs Hilary Levesley for providing me with the experimental logbooks and for solving any administrative problems, which all make my life much easier.

I would like to especially say thank you to Mr. Gordon Askwith for refilling the solvents and acids in the chemical bench, for maintaining the hygiene in the cleanroom every day, and for teaching me to speak with a British accent. I wish to thank my friends, from UK and China for giving me a lot of support and for always sharing the happiness and sorrow with me. You are all so important to me.

Finally, I would like to deeply thank my family. The great belief and value you have given me enable me to get through the toughest time. Nothing in my life would have been possible without your love, support and encouragement.

Publications

• Journal Publications

1. **K. Xing**, Y. Gong, X. Yu, J. Bai, and T. Wang, *Improved crystal quality of (11-22) semi-polar GaN grown on a nano-rod template*, Jpn J. Appl. Phys. **52**, 08JC03 (2013)
2. J. Bai, Y. Gong, **K. Xing**, X. Yu, and T. Wang, *Efficient reduction of defects in (11-20) non-polar and (11-22) semi-polar GaN grown on nano-rod templates*, Appl. Phys. Lett. **102**, 101906 (2013).
3. Y. Gong, **K. Xing**, J. Bai, and T. Wang, *Greatly improved crystal quality of non-polar GaN grown on a-plane GaN nano-rod template obtained using self-organised nano-masks*, Phys. Status Solidi C **9**, 564 (2012).
4. **K. Xing**, Y. Gong, J. Bai, and T. Wang, *InGaN/GaN quantum well structures with greatly enhanced performance on a-plane GaN grown using self-organized nano-masks*, Appl. Phys. Lett. **99**, 181907 (2011).
5. Y. Gong, **K. Xing**, and T. Wang, *Influence of high temperature AlN buffer on optical gain in AlGaN/AlGaN multiple quantum well structures*, Appl. Phys. Lett. **99**, 171912 (2011).

• Conference Contributions

1. Y. Gong, **K. Xing**, B. Xu, X. Yu, Q. Zeng, R. Smith, J. Bai, and T. Wang, *High efficiency long-wavelength emission from InGaN/GaN MQWs on semi-polar (11-22) GaN overgrown on micro-rod templates*, UK Nitrides Consortium (UKNC) Winter Conference, University of Nottingham, UK (2015).
2. B. Xu, X. Yu, Y. Gong, **K. Xing**, B. Liu, J. Bai, and T. Wang, *Study of High Quality (11-22) Semi-polar GaN Grown On Nano-rod Templates,* International Workshop on Nitride Semiconductors (IWN), *Wroclaw, Poland* (2014).
3. **K. Xing**, Y. Gong, X. Yu, J. Bai, and T. Wang, *Improved crystal quality of (11-22) semi-polar GaN grown on semi-polar nano-rod template,* International Workshop on Nitride Semiconductors (IWN), Sapporo, Japan (2012).

4. **K. Xing**, Y. Gong, X. Yu, J. Bai, and T. Wang, *Study of overgrowth of non-polar GaN grown on a-plane GaN nano-rod template*, UK Nitrides Consortium (UKNC) Winter Conference, University of Bath, UK (2012).
5. P. Renwick, H. Tang, Y. Gong, **K. Xing**, J. Bai, and T. Wang, *Study of LO-phonon and exciton interaction in GaN/InGaN MQW nano-rod structures*, UK Nitrides Consortium (UKNC) Winter Conference, University of Bath, UK (2012).
6. Y. Gong, **K. Xing**, J. Bai, and T. Wang, *Greatly improved crystal quality of non-polar GaN grown on a-plane GaN nano-rod template obtained using a self-organised nano-mask*, International Conference on Nitride Semiconductors (ICNS), Strathclyde, UK (2011).
7. **K. Xing**, Y. Gong, Q. Wang, and T. Wang, *Investigation of strain of GaN grown on high temperature AlN buffer*, UK Nitrides Consortium (UKNC) Winter Conference, University of Manchester, UK (2011).
8. Y. Gong, **K. Xing**, Q. Wang, and T. Wang, *Influence of high temperature AlN buffer on optical gain in AlGaN/AlGaN multiple quantum well structures*, UK Nitrides Consortium (UKNC) Winter Conference, University of Manchester, UK (2011).

Contents

Chapter 1

Introduction

1.1. Introduction to III-nitride Semiconductors

III-nitride compound semiconductor materials, GaN, AlN, InN and their alloys, have broad potential applications in semiconductor optoelectronic devices. This is due to their unique chemical and physical properties such as direct bandgap, chemical and thermal stability, etc. The bandgaps of III-nitride semiconductors cover a wide spectral range from deep ultraviolet, through visible, to infrared, which are unavailable for any other conventional semiconductors. The last two decades have seen major advances in the development of growth technologies required for III-nitrides with device performance, mainly leading to commercialization of violet/blue LEDs [1-4] and LDs [5, 6]. Blue LEDs are a key component for the fabrication of white lighting sources for general illumination due to their high efficiency, compact size and long life-time. In addition, III-nitride based LEDs have a wide range of applications in many areas, such as large display, backlighting, traffic lights, environmental protection, life-science, medical instrument, water-purification, visible light communication, etc. However, there still exist a number of fundamental challenges, such as crystal quality, green/yellow gap, efficiency droop, low efficiency in the UV spectral region, etc. Therefore, it is still critically important to further devote substantial effort to this area. Clearly, all the issues are directly related to the crystal quality of GaN and its alloy as a result of lack of suitable substrates.

1.2. History of III-nitride Semiconductors

GaN materials in the form of powder were firstly prepared in 1932, by passing ammonia (NH_3) over a piece of hot gallium metal. [7] In 1969, single crystalline GaN was prepared on a sapphire substrate by hydride vapour phase epitaxy (HVPE) [8]. Four years later, the first III-nitride LED was demonstrated based on this growth method [9], although the device performance was far from satisfactory due to the very low crystal quality. Since then GaN began to attract more attention to act as a good candidate for optical emitters. This story has

not been changed until 1986 when Amano and Akasaki developed a two-step growth method, namely, initial deposition of a thin AlN nucleation layer at 550^{o}C [10], followed by GaN growth at a high temperature, leading to for the first time achieving an atomically flat surface of GaN on sapphire. In 1991, Nakamura used a low temperature GaN layer as the nucleation layer prior to high temperature growth of GaN [11], also enabling the deposition of GaN with a relatively low defect density (~10^{9}cm^{-2}) and surface morphology with mirror-like flatness. Another major breakthrough is due to achieving p-type GaN realized by Akasaki and Amano [12], namely, the p-type GaN doped with magnesium (Mg) can be obtained by being activated by low energy electron beam irradiation (LEEBI) treatment. Later on, Nakamura developed a very cost-effective approach to obtaining p-GaN, i.e., annealing magnesium doped GaN at a high temperature under nitrogen ambient, meaning that a mass production of GaN-based LEDs becomes possible. In 1993, Nakamura [3, 5] succeeded in manufacturing first GaN-based high-brightness LED on a candela level. In 2014, Akasaki, Amano and Nakamura have been awarded the Nobel Prize due to their contribution as stated above.

1.3. Challenges

1.3.1. Substrate Issue

Ideally, homoepitaxial growth of GaN is best. Unfortunately, homoepitaxial growth of GaN is extremely expensive, as free-standing GaN substrates is currently obtained only through combination of growing a thick GaN by using HVPE and a subsequent laser lift-off process [13]. Hence it is not realistic for mass production, although great performance of nitride-based devices on free-standing GaN substrates has been demonstrated in laboratories [14]. An alternative way is to grow GaN films on cost-effective but lattice-mismatched foreign substrates, known as heteroepitaxial growth. Silicon (Si), silicon carbide (SiC) and sapphires are the three most commonly used substrates for heteroepitaxial growth of GaN. Si is advantageous as a result of its low cost and mature integrated circuit (IC) technologies. However, there is a large lattice mismatch (17%) between Si and GaN. Furthermore, a large difference of thermal expansion coefficients between silicon and GaN further worsens the situation, easily causing a severe cracking issue. Moreover, GaN grown on Si at a high temperature suffers from a melt-back etching [15], which can be avoided by using AlN buffer technology. SiC/GaN has a much smaller lattice mismatch (~3.5%) compared with Si/GaN,

but the expensive cost of SiC makes GaN-on-SiC less competitive for mass production. Among all these substrates, c-plane (0001) sapphire is a good substrate for GaN heteroepitaxial growth. In fact, c-plane sapphire becomes the mostly used substrate for GaN epitaxial growth although the lattice-mismatch between GaN and sapphire is still up to 16%. As a result, GaN grown on sapphire substrate suffers from a high density of extended defects. It has been demonstrated that threading dislocations (TD) and basal stacking faults (BSF) are presented as predominant defects in GaN which can deteriorate the device performance, as TDs act as non-radiative recombination centres and charge scattering centres [16, 17].

1.3.2. Green/Yellow Gap

One of the major challenges in solid state lighting is that optical devices with high performance across the visible spectrum have to be achieved in order to compete with the conventional lighting in terms of efficiency. III-nitride based LEDs are an excellent candidate because the composition of the alloys (Al, Ga, In) N can be adjusted to enable the emission covering a wide spectrum ranging from deep UV to infrared, including the full visible spectrum. Usually, In composition determines the emission wavelength in the visible region for commonly used InGaN/GaN quantum wells (QWs) serving as the optical active area. However, as the emission moves towards a longer wavelength by increasing indium composition, the optical efficiency significantly reduces. The problem becomes more serious when the emission wavelength moves towards the green, yellow, and orange spectral regions (>500nm) [18]. This is because InGaN with high indium composition needs to be grown at a low temperature, which results in a high density of defects. Moreover, with increasing indium composition, the lattice mismatch between InGaN and GaN becomes larger, leading to larger compressive strain in the QWs. This strain introduces large piezoelectric field induced polarization across the QWs, leading to a reduction in overlap of electron and hole wavefunction and thus decrease in optical efficiency. The external quantum efficiency (EQE) of GaN-based LED as a function of emission wavelength is illustrated in Figure 1.1, where the efficiency reduction with increasing emission wavelength has been demonstrated. Group III-P materials such as GaP and AlP have narrower band gaps than III-nitride materials, potentially giving emission with longer wavelength. However, they are a group of indirect

band gap materials with a low radiative recombination efficiency, which constrains its practical applications.

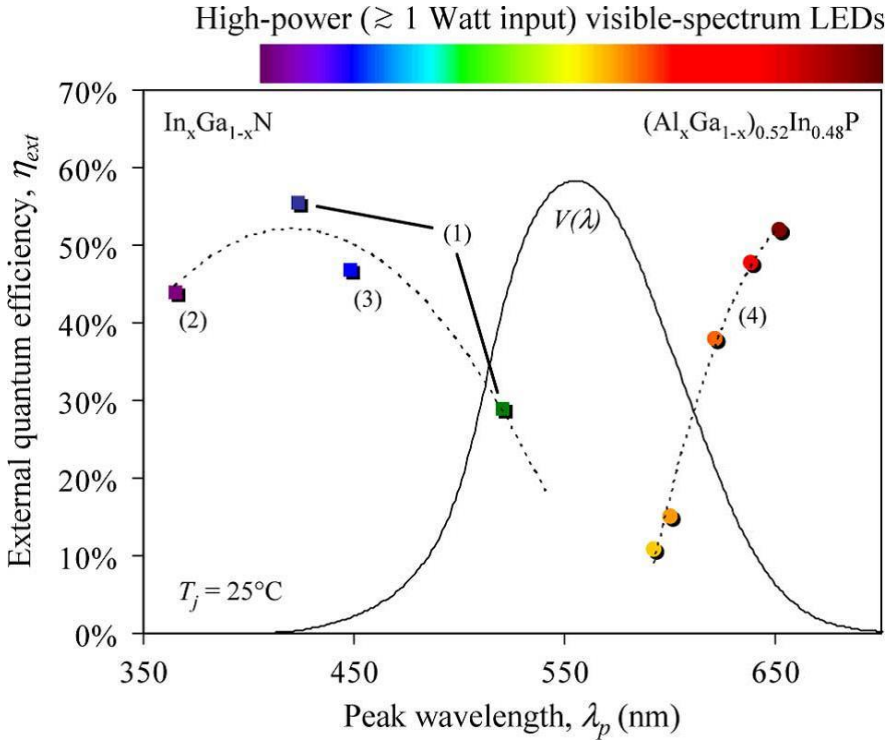

Fig. 1.1: External quantum efficiency of high-power visible-spectrum LEDs as a function of the emission wavelength, where V (λ) represents human eye response [19].

1.3.3. Other Fundamental Issues

(a) Quantum Confined Stark Effect

Owing to the structural inversion asymmetry, a spontaneous polarization is induced along c-direction in III-nitride materials [20]. Currently, the lattice mismatch will introduce a strong piezoelectric polarization. The discontinuities of polarizations induce internal electric fields across the QW structure, pulling the electron and hole wave functions apart from each other. The reduction in overlaps between the wave functions means a lowered recombination rate and a redshift of emission peak, namely, quantum confined Stark effect (QCSE) [21]. This effect poses a major challenge for further improvement of the optical efficiency of the III-nitride emitters, and becomes even more prominent with higher indium composition due to an increased strain-induced piezoelectric field.

(b) Efficiency Droop

Another challenge for III-nitride based LEDs is the so called efficiency droop. With increasing injected current density continuously, the EQE first reaches a maximum value and then decreases significantly. For example, the IQE can drop up to 50% from its peak value with the increase of the current required for practical applications. This problem becomes more prominent as the emission wavelength moves towards the green/yellow spectral region. This is also one pressing issue which hinders the further improvement of blue emitters efficiency. Figure 1.2 illustrates the normalized EQE as a function of the injection current for a typical blue LED emitting at a wavelength of 460 nm. It can be observed that when the injection current exceeds 10 mA, the EQE drops tremendously. It is notable the LED is injected by a pulsed current, the thermal effect was excluded.

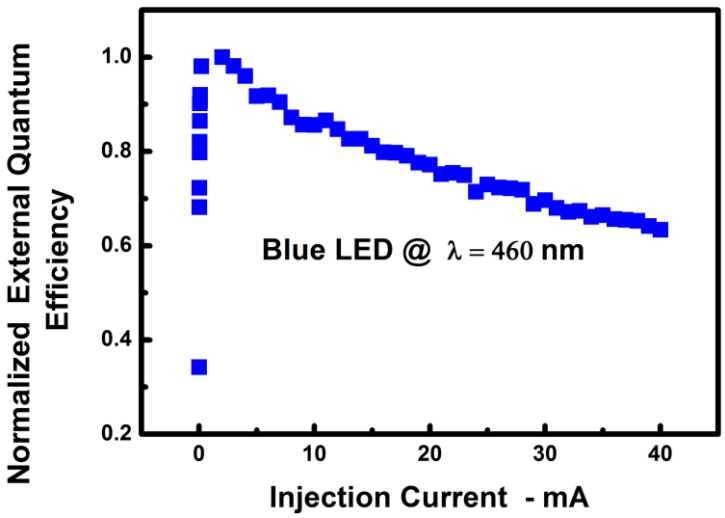

Fig. 1.2: The normalized external quantum efficiency as a function of the injection current. [22]

The mechanism of efficiency droop remains under debate. Usually, current overflow, crystal quality, polarization mismatch, defects, Auger recombination and poor hole transport have been proposed, but have not yet come to a conclusion. Some recent experimental studies revealed that the Auger recombination may be the main reason responsible for the efficiency droop [23]. Auger recombination can be simply illustrated by Figure 1.3. When an electron recombines with a hole, it releases energy in the form of a photon. Before emitted into free space, the released photon is reabsorbed by a second electron, allowing it to be excited to a higher energy level [24]. Auger recombination process exhausts useful electron-hole pairs, resulting in reduced optical efficiency in LEDs.

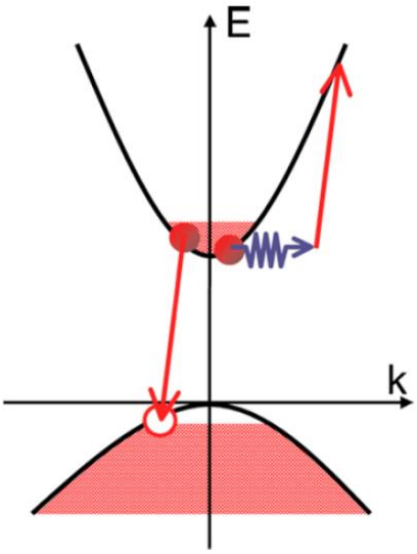

Fig. 1.3: Schematic diagram of the Auger recombination [25].

1.4. Motivation and Aim

As discussed in section 1.3, III-nitride based LEDs are facing a number of challenges such as QCSE and green/yellow gap. These negative effects could have a significant impact on LED optical performance and need to be solved. It is known that GaN grown along a non-polar or semi-polar direction can eliminate or partially reduce the QCSE [26]. Furthermore, it has been reported that significantly enhanced indium incorporation can be archived on semi-polar GaN, in particular (11-22) GaN, compared with c-plane GaN, which seems very promising to overcome the 'green gap' [27]. However, the crystal quality of non-polar and semi-polar GaN grown on sapphire is far from satisfactory. Therefore, the aim of the research presented in the thesis is to achieve high material quality non-polar and semi-polar epitaxial GaN films with an ultra-low defect density, high reproducibility and good uniformity across 2-inch wafers, meeting the requirement for mass production.

1.5. Thesis Overview

The thesis is divided into 7 Chapters:

Chapter 1 includes a brief introduction and a history of development of III-nitride based semiconductors. The challenges and motivation of this project are briefly discussed.

Chapter 2 presents a detailed background including the semiconductor theories related to III-nitrides. A detailed introduction of non-polar and semi-polar GaN, epitaxial overgrowth of GaN and etching of GaN are conducted.

Chapter 3 covers all the material characterization techniques used in this research, including in-situ laser reflectivity, X-ray diffractometer (XRD), scanning electron microscopy (SEM), transmission electron microscopy (TEM), atomic force microscopy (AFM), and photoluminescence (PL). A number of semiconductor fabrication techniques including physical vapour deposition (PVD), chemical vapour deposition (CVD), rapid thermal annealing (RTA) and a few dry etching techniques are introduced.

Chapter 4 reports two kinds of fabrication techniques which have been successfully developed: semi-/non-polar GaN nano-rod array templates fabricated by self-organized nickel masks and semi-polar GaN micro-rod array templates fabricated using UV photolithography. The detailed optimization of the two approaches has been provided, and optical and structural characterization of the templates has been investigated.

Chapter 5 studies the semi-polar and non-polar GaN overgrown on the nano-rod templates. The mechanism of defect reduction in the overgrown GaN is explored. InGaN/GaN QW structures with significantly enhanced optical and electrical properties are grown on the overgrown GaN in order to demonstrate greatly improved crystal quality of the overgrown GaN.

Chapter 6 investigates the structural and optical properties of semi-polar GaN overgrown on the micro-rod templates. The mechanisms of the overgrowth and defect reduction in the semi-polar GaN are explored in detail. The InGaN/GaN QW structures with long wavelengths from green to orange have been successfully obtained by growth on the massively improved semi-polar GaN, demonstrating considerably high internal quantum efficiency.

Chapter 7 summarizes all the results involved in this thesis and discusses a future plan.

References

1. T. Nishida, H. Saito, and N. Kobayashi, Appl. Phys. Lett. **79**, 711 (2001).
2. S. Nakamura, M. Senoh, and T. Mukai, Appl. Phys. Lett. **62**, 2390 (1993).
3. S. Nakamura, T. Mukai, and M. Senoh, Appl. Phys. Lett. **64**, 1687 (1994).
4. S. Nakamura, M. Senoh, N. Iwasa, and S. Nagahama, Jpn. J. Appl. Phys. **34**, L797 (1995).
5. S. Nakamura, M. Senoh, S. Nagahama, N. Iwasa, T. Yamada, T. Matsushita, H. Kiyoku, and Y. Sugimoto, Jpn. J. Appl. Phys. **35**, L74 (1996).
6. J. K. Park**,** M. A. Lim**,** C. H. Kim**,** H. D. Park, J. T. Park, and S. Y. Choi, Appl. Phys. Lett. **82**, 683 (2003).
7. W. C. Johnson, J. Parsons, and M. C. Crew, J. Phys. Chem. **36**, 2561 (1932).
8. H. P. Maruska, and J. J. Tietjen, Appl. Phys. Lett. **15**, 327 (1969).
9. J. I. Pankove, E. A. Miller, and J. E. Berkeyheiser, RCA Review **32**, 383 (1971).
10. H. Amano, N. Sawaki, I. Akasaki, and Y. Toyoda, Appl. Phys. Lett. **48**, 353 (1986).
11. S. Nakamura, Jpn. J. Appl. Phys. **30**, 1705 (1991).
12. H. Amano, M. Kito, K. Hiramatsu, and I. Akasaki, Jpn. J. Appl. Phys. **28**, L2112 (1989).
13. X. A. Cao, S. F. LeBoeuf, M. P. D'Evelyn, S. D. Arthur, J. Kretchmer, C. H. Yan, and Z. H. Yang, Appl. Phys. Lett. **84**, 4313 (2004).
14. P. Roussel, Cs Mantech Conference 231 (2006).
15. H. Ishikawa, G. Zhao, N. Nakada, T. Egawa, T. Jimbo and M. Umeno, Jpn. J. Appl. Phys. **38**, L492 (1999).
16. J. S. Speck and S. J. Rosner, Physica B **24-32**, 273 (1999).
17. D. Cherns, S. J. Henley, and F. A. Ponce, Appl. Phys. Lett. **78**, 2691 (2001).
18. J. Hwang, R. Hashimoto, S. Saito, and S. Nunoue, Jpn. J. Appl. Phys. **52**, 08JL13 (2013).
19. S. Pleasants, Appl. Phys. Express **6**, 062102 (2013).
20. M. R. Krames, O. B. Shchekin, R. Mueller-Mach, G.O. Mueller, L. Zhou, G. Barbers, and M. G. Craford, J. Display Technol. **3**, 160 (2007).
21. F. Bernardini, V. Fiorentini, and D. Vanderbilt, Phys. Rev. B **56**, R10024 (1997).
22. H. P. T. Nguyen, S. Zhang, K. Cui, X. Han, S. Fathololoumi, M. Couillard, G. A. Botton, and Z. Mi, Nano Lett. **11**, 1919 (2011).
23. J. Iveland, L. Martinelli, J. Peretti, J. S. Speck, and C. Weisbuch, Phys. Rev. Lett. **110**, 177406 (2013).

24. Y. C. Shen, G. O. Mueller, S. Watanabe, N. F. Gardner, A. Munkholm, and M. R. Krames, Appl. Phys. Lett. **91**, 141101 (2007).
25. E. Kioupakis, P. Rinke, K. Delaney, and C. Van de Walle, Appl. Phys. Lett. **98**, 161107 (2011).
26. P. Waltereit, O. Brandt, A. Trampert, H. T. Grahn, J. Menninger, M. Ramsteiner, M. Reiche, and K. H. Ploog, Nature (London) **406**, 865 (2000).
27. P. D. Mierry, T. Guehne, M. Nemoz, S. Chenot, E. Beraudo, and G. Nataf, Jpn J. Appl. Phys. **48**, 031002 (2009).

Chapter 2

Background

2.1. Semiconductors

2.1.1. Introduction

Materials can be classified into three groups in terms of their electrical properties, which are insulators, semiconductors and conductors. In an insulating material, the electrically charged carriers cannot move freely, while a conducting material allows flow of electric charges. Semiconductors are a group of crystalline materials which have an intermediate conductivity between those of a conductor and an insulator. An effective way to visualize the difference between materials is to introduce the energy bands theory. Basically there are three band regions, i.e. valence band, conduction band and band gap (as shown in Figure 2.1). In the valence band, the electrons are tightly bound to the atoms and cannot move freely, whereas the carriers are free to move throughout the crystal lattice in the conduction band. Thus, electrons in the conduction band have higher energy level compared with the valence band. The energy difference between the minimum energy in the conduction band and the maximum energy in the valence band is defined as the band gap. Therefore, a semiconductor generally has a relatively smaller band gap than an insulator.

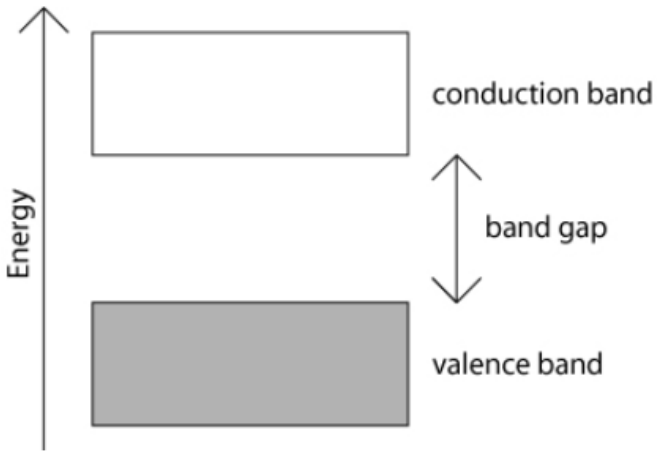

Fig. 2.1: Schematic diagram of electronic band structure [1].

2.1.2. Direct and Indirect Band Gap

In a semiconductor, the minimum energy in the conduction band and the maximum energy in the valence band may not be at the same momentum, and this semiconductor is defined as an indirect band gap semi-conductor. In contrast, for a direct band gap semiconductor, the minimum energy of the conduction band and the maximum energy of the valence band have the same momentum. The schematic diagram of the direct and indirect band gap semiconductors are illustrated in Figure 2.2. In a direct band gap semiconductor, an electron-hole pair can be easily generated by a photon with high energy as it does not require momentum change; whereas it is more difficult for an electron-hole pair to be generated in an indirect band gap semiconductor because it not only needs the excitation of electron by a photon but also requires a lattice vibration in order to change momentum under conservation laws. The electron-hole recombination process in direct band gap and indirect band gap semiconductors have the similar manners. From this point of view, the direct band gap semiconductors, which have much higher radiative recombination efficiencies than those of the indirect band gap semiconductors, are more suitable for fabrication of optical emitters.

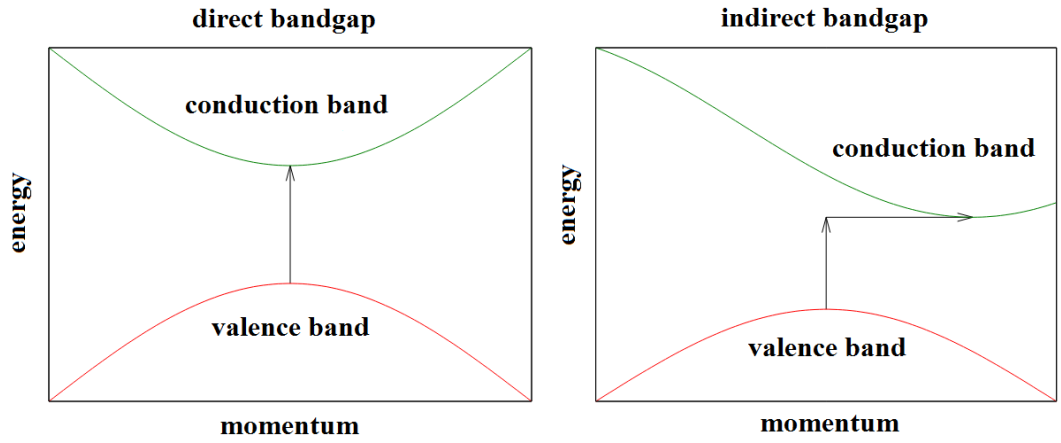

Fig. 2.2: Schematic diagram of the direct and indirect band gap semiconductors [2].

2.1.3. III-nitride Semiconductors

Figure 2.3 shows the band gap energies of common semiconductors against their lattice constant. III-nitride semiconductors have direct band gaps ranging from 0.7 eV (InN) to 6.2 eV (AlN) [3], covering a very broad spectrum from infrared to deep ultraviolet. In

comparison, the band gaps of other semiconductors only occupy a very limited spectrum region, either in the relatively short wavelength region (II-VI compounds) or in the very long wavelength region (III-Arsenides and III-Phosphides). Therefore, III-nitride based materials are ideal semiconductors for band gap engineering in order to realize optical emitters with various emission wavelengths, especially in the blue and ultraviolet regions.

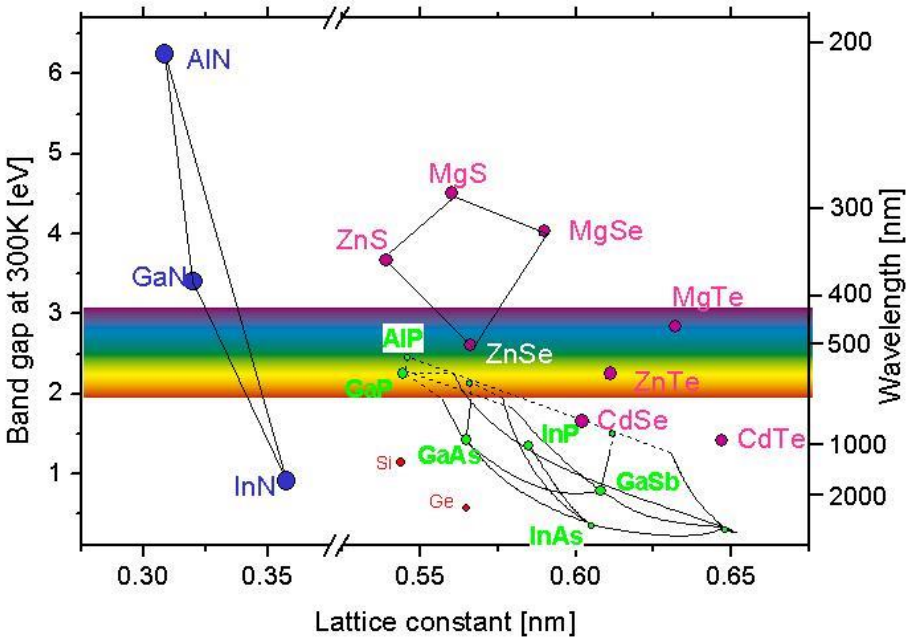

Fig. 2.3: Band gap energies of various semiconductors against their lattice constant [4].

2.2. Defects in Semiconductors

Crystal defects, the major cause for degradation in the optical property of optoelectronic devices, implies the imperfection in crystal lattices which are composed by periodically atomic arrangements. The defects in semiconductors can be classified into three categories according to their dimensions: zero-dimensional defects (point defects), one-dimensional defects (dislocations or linear defects) and two-dimensional defects (interfaces).

A point defect means the condition of missing of an atom or an atom being in irregular place in the crystal lattice, including vacancy, self-interstitial atom, interstitial impurity atom and substitution impurity atom. An illustration of a point defect is shown in Figure 2.4. A vacancy is where an atom is missing from the lattice. A self-interstitial atom is an extra atom which is crowded into the bulk atoms from a lattice. An interstitial impurity atom is a different type of

atom fitting into the voids between the original atoms. A substitution impurity atom is a different type of atom substituting the bulk atom in the crystal lattice.

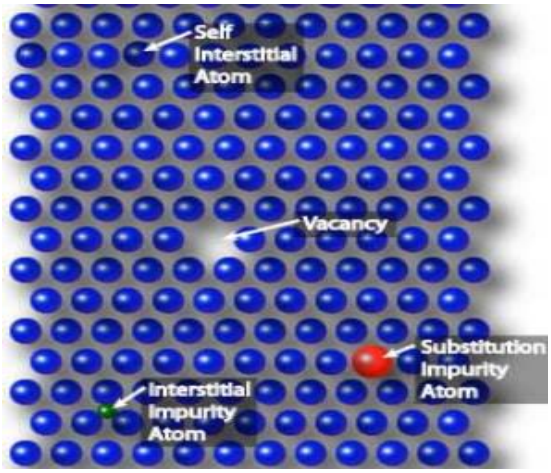

Fig. 2.4: Schematic diagram of different types of point defects [5].

Dislocations are the line defects where the atoms are out of position. There are basically two types of dislocations: edge and screw dislocations. But in most cases, the dislocations are a hybrid of edge and screw dislocations, which are named as mixed dislocations. The schematic representations of the edge and screw dislocations are shown in Figure 2.5(a). The edge dislocation is visualized as an extra half plane generated in a lattice. The direction of edge dislocation is perpendicular to the extra half plane. The screw dislocation can be seen as atoms slipping from the crystal by a lattice vector and forming a boundary plane. It is parallel to the orientation in which the crystal is distorted.

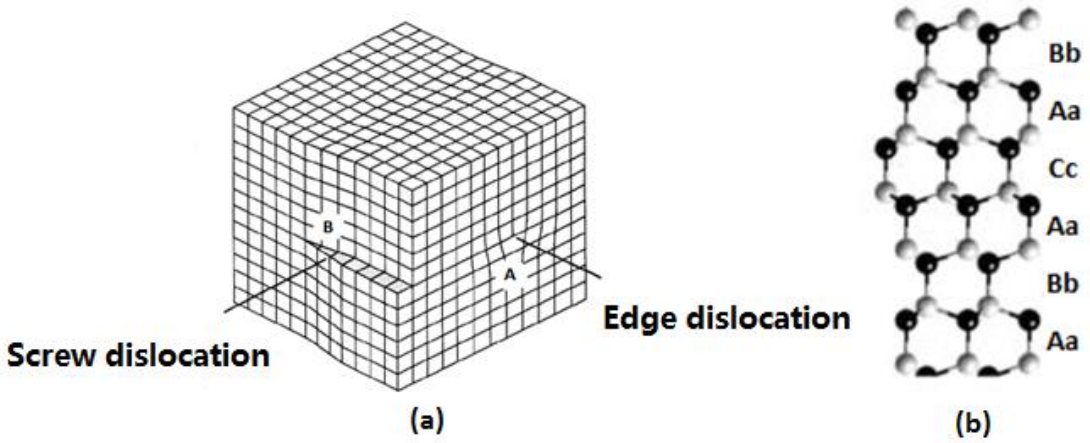

Fig. 2.5: Schematic illustration of (a) edge and screw dislocation; and (b) atom sequence model for a type of stacking fault [6].

A stacking fault, a typical planar defect in hexagonal non-polar and semi-polar GaN, is defined as a change in the stacking sequence of atomic planes in a crystal. An example of a stacking fault is schematically shown in Figure 2.5(b). The initial stacking sequence of the structure is denoted as AaBb. However, there is an extra layer of atoms Cc which suddenly changes the regular arrangement to AaBbCcAaBb, forming a stacking fault.

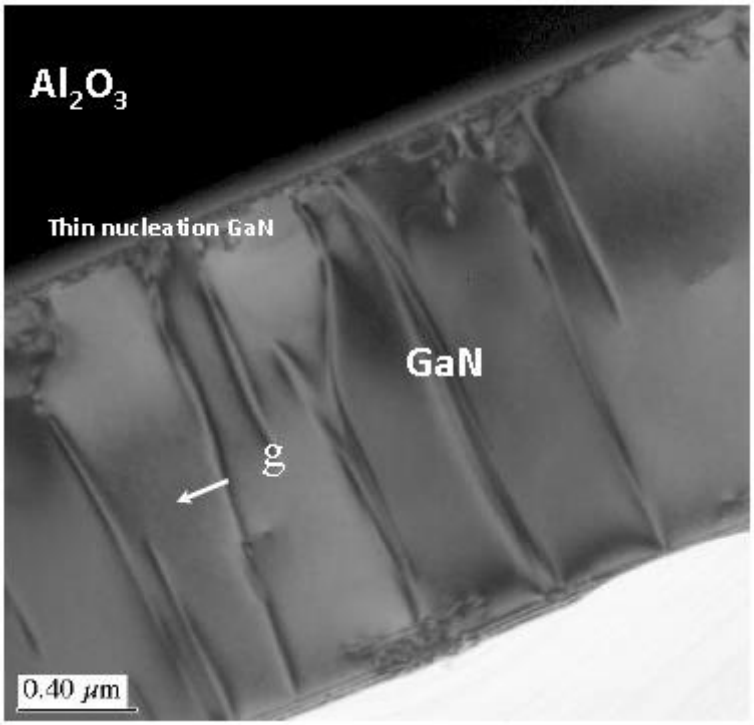

Fig. 2.6: The cross-sectional two-beam bright-field TEM image of dislocations [7].

The most common defects which appear in c-plane GaN are screw dislocations, edge dislocations or a mixed type of both. Apart from edge and screw dislocations, non-polar and semi-polar GaN also have a high density of basal stacking faults [8]. Reports have shown that the dislocation density and basal stacking fault density of non-polar and semi-polar GaN are ~10^{10} cm^{-2} and ~10^{5} cm^{-1}, respectively [8]. As shown in Figure 2.6, the defects can be observed in the nucleation layer of GaN by transmission electron microscopy (TEM), which will be detailed introduced in Chapter 3.

2.3. Epitaxial Growth Technologies

The epitaxial growth techniques of III-nitride semiconductors have been developed during the last 30 years. Molecular beam epitaxy (MBE) [9, 10] and metal organic chemical vapour deposition (MOCVD) [11-13] are the typical facilities for growth of advanced semiconductors. MBE has been successfully employed in growth of conventional III-V semiconductors, such as GaAs, GaSb, etc. However, due to the intrinsic limits of MBE (lack of N source), it is extremely difficult to grow III-nitride semiconductors [14]. Up to date, MBE is less attractive to III-nitride industry.

Metalorganic chemical vapor deposition (MOCVD), also known as metal organic vapor phase epitaxy (MOVPE), is designed to grow thin crystalline layers on the top of solid substrates via chemical reactions. A high growth temperature exceeding 1000^{o}C can be easily obtained by MOCVD, which is essential for growth of high-quality GaN. Unlike MBE, the growth rate of MOCVD for GaN is normally fast benefited from the high flow rate of gases. MOCVD is most widely used for the growth of III-nitride semiconductors due to its precision in deposition of uniform thin films (with accuracy better than monolayer), good flexibility, and ability to grow nitride-based alloys in a single growth machine. In addition, MOCVD is also advantageous due to its relatively low running & maintenance cost and hence its availability for mass production. Thus, it is feasible to create commercially available, high quality GaN crystals and their related device structures by employing MOCVD [9].

There are basically two types of techniques for MOCVD growth in terms of configuration, vertical reactor such as close coupled showerhead reactor [12] and horizontal reactor technology [15]. They are based on different flowing patterns and resultant growth characteristics. In the horizontal reactor, the sources are inserted laterally to a slowly rotating susceptor. Normally the substrate has a small angle of inclination to the horizontal direction in order to achieve a uniform crystalline structure. In a close coupled showerhead reactor, the chemicals are introduced vertically through a showerhead like reactor ceiling. The susceptor is rotating at a fast speed (~100 rpm) during the growth to improve the wafer uniformity. In this thesis, only the close coupled showerhead reactor MOCVD will be employed.

In the MOCVD growth, the atomic arrangement of the growing films follows the crystal structure of substrate. Therefore, the ideal substrate should have the same crystal type, similar lattice parameters and thermal expansion coefficient as the growing film. If GaN is grown on

a native GaN substrate, then it is defined as homoepitaxial growth; if it is grown on a foreign substrate, then it is named heteroepitaxy. In this thesis, sapphire substrates with different orientations are employed for growth of c-plane, non-polar and semi-polar GaN, respectively.

2.4. Crystal Structure of III-nitrides

The III-nitrides can be crystallized into three different kinds of structures: wurtzite [16], zinc-blende [17] and rock-salt [18]. The latter two are not suitable for practical applications as they are only stable in some particular circumstances. In contrast, the wurtzite III-nitrides are thermodynamically stable and currently the most commonly used type of crystal structure for MOCVD growth. In this thesis, we only focus on the investigation of wurtzite III-nitrides.

In III-nitrides, each nitrogen atom is bound to four group-III atoms, and similarly, each group-III atom is coordinated by four nitrogen atoms, hence forming a hexagonal closely packed unit cell, which could be simply depicted by the typical wurtzite lattice presented in Figure 2.7. The facets of the lattice could be denoted by Miller indexes in a hexagonal coordinate system, (a_1, a_2, a_3, a_4). Three most important facets are frequently used for the GaN epitaxial growth. They are c-plane (0001), m-plane (10-10) and a-plane (11-20) facets, respectively, as shown in the shadowed region in Figure 2.7.

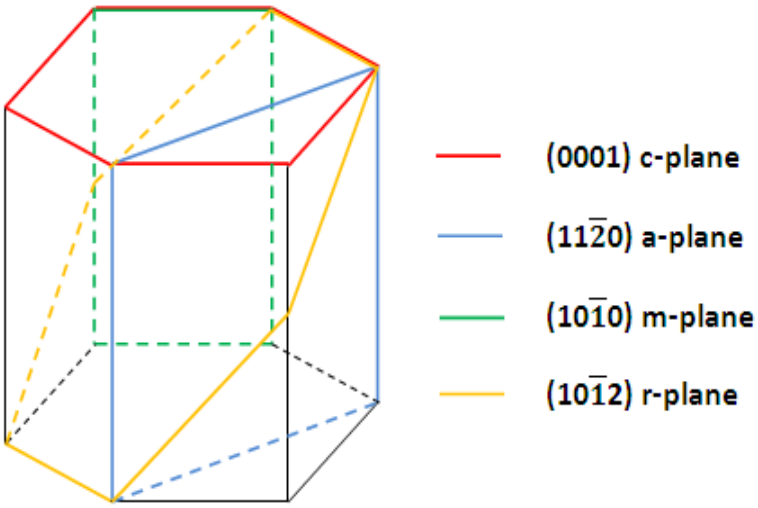

Fig. 2.7: Crystal structure of wurtzite III-nitride materials [19].

In the case of c-plane GaN growth on (0001) sapphire, the lattice mismatch in basal planes can reach ~33%, which generates a big tensile strain. However, it has been found that GaN basal plane tends to rotate 30^{o} around the c-axis to minimize the lattice mismatches in the actual epitaxial growth. Under this situation, the lattice mismatch is reduced to ~16%, with a compressive strain [20]. The stacking mode between GaN and the c-plane sapphire is schematically shown in Figure 2.8.

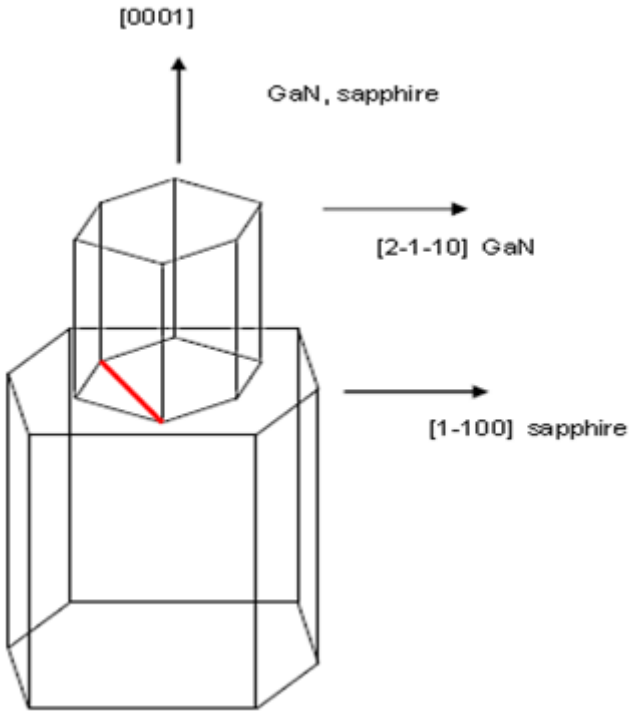

Fig. 2.8: Stacking sequence of c-plane GaN grown on (0001) sapphire [21].

2.5. Material Properties of III-nitrides

2.5.1. Electrical Properties and Doping

When an electric field is applied to a semiconductor, negatively charged (electrons) and positively charged free carriers (holes) are accelerated in particular directions, which leads to electric current. Theoretically, in pure GaN material at room temperature, the number of thermally excited electrons is quite small due to its large band gap. Hence, the resistivity in pure GaN material is relatively high. But if a small amount of group-IV impurity atoms is doped in GaN, its conductivity will increase tremendously. This is because some Ga atoms

can be substituted by Si atoms during the growth, which can provide an additional valence electron compared to Ga atoms. Each additional electron is weakly bound to the introduced impurity atom and can easily be excited to the conduction band at room temperature, hence greatly enhance its conductivity. This material is called n-type GaN. Silicon is a typical dopant to achieve n-type GaN. Similarly, if Ga atoms were substituted by group-II impurity atoms, as there is one less valence electron for each Ga atom, holes will be introduced into the valence band. This type of material is named p-type GaN. Magnesium is a typical p-type dopant. Generally, unintentionally doped GaN exhibits n-type because of the existence of a large number of defects such as Ga or N vacancies [22].

When a semiconductor is under the influence of an electric field, electrons and holes will move in particular direction, and can be described by their mobilities. The mobility of a carrier in a semiconductor is dependent on defect concentration and carrier concentration. Mobility is a very important parameter for evaluation of semiconductor materials, and it is very useful parameter for evaluating the GaN defect density. Table 2.1 presents some electrical properties of GaN as well as some other Group III-V semiconductors.

Material	Bandgap at 300 K (*eV*)	Electron Mobility *(cm^2/Vs)*	Thermal Conductivity *(W/cm^0C)*	Breakdown Field *(MV/cm)*
GaN	3.4	900	2.3	3.3
GaAs	1.4	8500	0.4	0.4
InP	1.3	5400	0.68	0.5

Table 2.1: Some electrical properties of Group III-V semiconductors.

Compared with other Group III-V semiconductors, GaN is advantageous for its wide bandgap, high thermal conductivity and high breakdown voltage. These make it more competitive in a wide range of applications in the optoelectronics field.

2.5.2. Chemical Properties

III-nitride materials such as GaN have excellent chemical and thermal stabilities. They are highly resistive to chemical solution and can stand high temperatures. The chemical etching and processing of GaN structures are thus very difficult. For example, even heated HCl/HNO_3 solutions cannot react with GaN; KOH can only etch GaN though attacking the defects in GaN and the etch rate becomes even slower as the GaN crystalline quality improves. Therefore, III-nitride materials can be used under some harsh environments. Table 2.1 presents some material properties for III-nitride materials, where the lattice constant, bandgap, thermal expansion coefficient and the refractive index of III-nitride materials are listed.

Material	Lattice constant at 300K ($\AA$)	Bandgap (eV)	Thermal expansion coefficient (K^{-1})	Refractive index	Melting Point (^oC)
AlN	a=3.111, c=4.978	6.2	4.15×10^{-6}	2.15	3000
GaN	a=3.189, c=5.185	3.4	5.59×10^{-6}	2.39	2500
InN	a=3.544. c=5.718	0.7	5.70×10^{-6}	2.93	2146

Table 2.2: Some material parameters of III-nitride based materials [23, 24].

2.6. Non-polar and Semi-polar GaN

2.6.1. Theory of Quantum Confined Stark Effects (QCSE)

III-nitride based emitters in the short wavelength region have developed during the past 25 years, leading to commercialisation of InGaN-based light emitting diodes (LEDs) and laser diodes (LDs) with high optical performances [25-27]. So far, these achievements are still limited to III-nitrides grown on c-plane sapphire substrates. However, one of the most pressing problems, which hinder further improvement of the device performance for c-plane III-nitrides-based optical devices, is the presence of the internal electric field caused as a result of spontaneous and piezoelectric polarization. The spontaneous polarization results

from the non-symmetry of wurtzite structure along the c-direction. Waltereit et al. reported that the spontaneous polarization of GaN and AlN are both directed towards the [000-1] direction and calculated to be 0.029 and 0.081 C/m^2, respectively [28]. The piezoeletric polarization is caused by the bi-axial mechanical stress between heterojunctions due to the lattice mismatch. The direction of piezoeletric polarization is along [000-1] direction for tensile strain and [0001] for compressive strain [29]. The net polarization leads to an internal electric field, causing tilting of the energy band of the quantum well (QW) structure and spatial separation of the electron and hole wavefunctions. Figure 2.9 (a) illustrates the schematic diagram of the band structure of c-plane InGaN/GaN QWs, where the electron and hole wavefunctions have a less overlap. The probability of the radiative recombination of electrons and holes is lower. Thus, the radiative recombination is suppressed and the optical performance is reduced. Moreover, the band tilting can give rise to a redshift in the emission wavelength, resulting in the Quantum Confined Stark Effect [30]. This negative effect becomes more serious especially when the emission wavelength is longer due to larger piezoelectric effects. Therefore, it is necessary to grow III-nitrides with eliminated or reduced internal electric fields in order to further improve the optical performance.

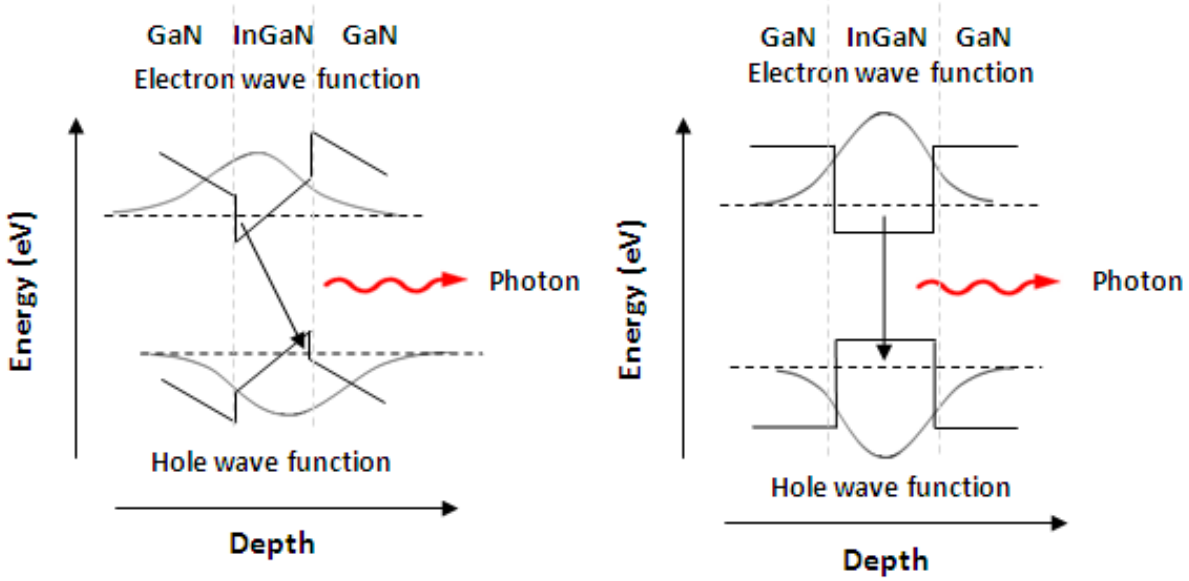

Fig. 2.9: (a) Band structure of c-plane InGaN/GaN quantum well, and (b) band structure of non-polar InGaN/GaN quantum well.

One of the most promising approaches to eliminate or partially reduce the polarization induced electric field is to grow non-polar or semi-polar GaN films. This is mainly because

the spontaneous and piezoelectric fields along different orientations vary dramatically. Researches show that the GaN along the non-polar orientation is totally free of the built-in electric fields [31], as the planes that are orthogonal to the c-plane will be theoretically free of QCSE. The band structure of non-polar InGaN/GaN quantum wells is shown in Figure 2.9 (b), in which a 'flat energy band' is obtained. As strain-induced polarization depends on the nature of piezoelectric coupling and the strain status, the peizoelectric polarization on different orientations varies dramatically. In order to calculate the orientation dependent piezoelectric field, we can transform the conventional (x, y, z) coordinate system into the new (x', y', z') coordiante system with the polar angle ϑ. Normally, due to the distinct space group symmetric $P6_3mc$ of wurtzite III-Nitrides, the piezoelectric polarization is related to strains as:

$$P^{pz} = \begin{pmatrix} 0 & 0 & 0 & 0 & e_{15} & 0 \\ 0 & 0 & 0 & e_{15} & 0 & 0 \\ e_{31} & e_{31} & e_{33} & 0 & 0 & 0 \end{pmatrix} \begin{pmatrix} \epsilon_{xx} \\ \epsilon_{yy} \\ \varepsilon_{zz} \\ \varepsilon_{yz} \\ \varepsilon_{xz} \\ \varepsilon_{xy} \end{pmatrix} = \begin{pmatrix} e_{15}\varepsilon_{xz} \\ e_{15}\varepsilon_{yz} \\ e_{31}(\epsilon_{xx} + \epsilon_{yy}) + e_{33}\varepsilon_{zz} \end{pmatrix}$$

with the elements e_{ij} of the piezoelectric tensor in Voigt notation. So the longitudinal piezoelectric polarization component $P_{Lz'}^{pz}$ can be written by:

$$\begin{aligned} P_{Lz'}^{pz} = {} & e_{31}cos\vartheta\epsilon_{x'x'} + \left(e_{31}cos^3\vartheta + \frac{e_{33} - e_{15}}{2} sin\vartheta\ sin2\vartheta\right)\epsilon_{y'y'} \\ & + \left(\frac{e_{33} + e_{15}}{2} sin\vartheta\ sin2\vartheta + e_{31}cos^3\vartheta\right)\epsilon_{z'z'} \\ & + [(e_{31} - e_{33})cos\vartheta\ sin2\vartheta + e_{15}sin\vartheta\ cos2\vartheta\ ]\epsilon_{y'z'} \end{aligned}$$

where all strains are defined in the new (x', y', z') coordinate system by using transformation. And the polarization component, which is responsible for surface charge density, should be determined by:

$$\Delta P_{z'} = P_{z'}^{pz} + (P_L^{sp} - P_T^{sp})cos\vartheta \quad [32]$$

where P_L^{sp} and P_T^{sp} are the spontaneous polarizations for the layer and the template, and $P_{z'}^{pz}$ is the piezoelectric polarization; ϑ represents the angle between the c direction and the surface normal. The calculation results of longitudinal polarization $P_{z'}^{pz}$ and total change of polarization at the InGaN/GaN interface $\Delta P_{z'}$ are presented in Figure 2.10.

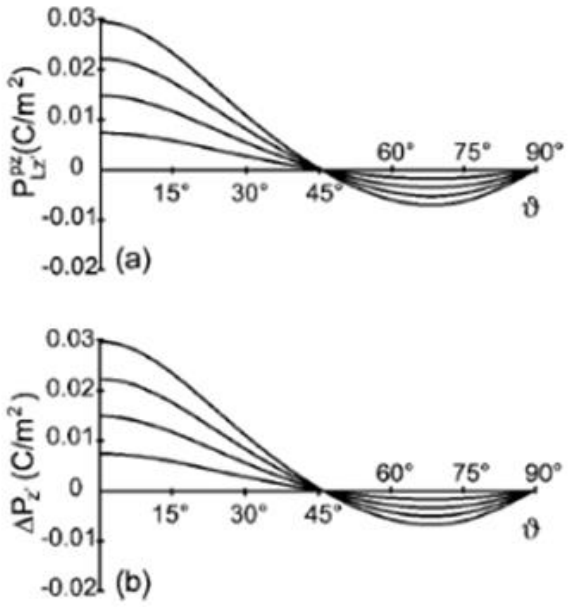

Fig. 2.10: Dependence of (a) piezoelectric polarization and (b) total polarization on the orientation [32].

InGaN epilayers grown on the (10-10) or (11-20) non-polar directions, the polarization along the surface normal is eliminated completely. If they are grown on the (11-22) semi-polar directions, which is 58^0 tilted with respect to c-plane, the piezoelectric induced polarization can be significantly suppressed [33, 34]. Reduced longitudinal piezoelectric fields in both semi-polar and non-polar InGaN/GaN MQWs structures result in more overlapping of electrons and holes wave functions and hence improvement of the internal quantum efficiency.

2.6.2. Current Status of Non-polar and Semi-polar GaN

The most promising solution to eliminate or reducing the QCSE is to grow the III-nitride based material along non-polar and semi-polar orientations. Non-polar and semi-polar GaN with low defects can be grown using free-standing non-polar or semi-polar GaN substrates, which can be obtained only though cleaving thick c-plane GaN with a few millimetres thickness prepared by HVPE along non-polar or semi-polar direction. Therefore, the free-standing non-polar and semi-polar GaN substrates only with a small size are possibly available, and thus they are extremely expensive. Previous attempts to grow non-polar and

semi-polar GaN by MOCVD have been performed on sapphire substrates. Sasaki et al. reported the a-plane non-polar GaN grown on a (10-12) r-plane sapphire substrate [35]. A smooth GaN surface morphology with fine ridge-like facets can be obtained. Other planes of non-polar GaN such as m-plane GaN can also be grown by using m-plane sapphire [36]. Semi-polar GaN such as (11-22) and (10-13) planes can be obtained by using m-plane sapphire [37, 38]. Nakamura et al. reported that (10-13) orientated GaN is dominant when using high temperature nitridation, whereas lower temperature nitridation leads to GaN with (11-22) orientation [39]. Pure (11-22) GaN is expected since the (10-13) orientated GaN surface is rough due to twinned crystalline. Sun et al. reported that the mixed phase of semi-polar GaN can be suppressed by the nitridation process, which is able to break surface symmetry of m-plane sapphire and make the nucleation of (11-22) GaN much easier [40]. [11-22] GaN surface can be grown with a smooth morphology as opposed to (10-13) orientation.

Due to the large lattice-mismatch between GaN and sapphire, the non-polar and semi-polar GaN grown on sapphire suffers from a high density of extended defects. These defects act as non-radiative recombination centres and charge scattering centres and can tremendously deteriorate the device performance [41, 42]. The x-ray rocking curves of the non-polar and semi-polar GaN on sapphire are both very broad, which are mostly related to the high dislocation densities and stacking fault densities. Therefore, up to now, it is the major challenge to improve the crystal quality of the non-/semi-polar GaN film in order to achieve high performance III-nitride devices.

2.6.3. Crystal Structure

Figure 2.11 shows the schematic hexagonal lattices of some commonly used planes in the non-polar (a and b) and semi-polar (c and d) GaN. The most common non-polar planes of wurtzite GaN include (11-20) and (10-10) planes, and semi-polar planes including (11-22) and (10-13) planes, respectively.

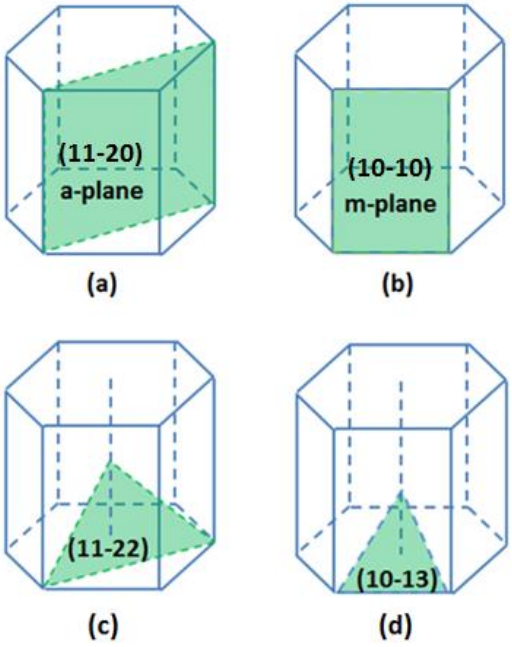

Fig. 2.11: Schematic hexagonal lattices of some commonly used planes in non-polar and semi-polar GaN.

2.6.4. Substrate Issue

Free-standing GaN, Silicon, Silicon Carbide (SiC) and sapphire are the four main substrates for the GaN epitaxial growth. The free-standing GaN substrate is ideal for GaN growth because the homoepitaxial growth mode theoretically leads to no extended defects of the epitaxial layers. In addition, GaN grown on this substrate undergoes no bi-axial strain, and hence is technically free of the piezoelectric polarization induced electric field. Accordingly, free-standing GaN serving as the substrate leads to the best performance GaN-based emitters. However, this substrate is extremely expensive and very difficult to grow so that it is still commercially unavailable. In a remarkable contrast with the free-standing GaN substrate, the silicon substrate is advantageous for its low cost. Its physical properties and availability make it a very good candidate as a good substrate for growth of GaN. Unfortunately, due to the large mismatch between silicon and GaN in terms of both lattice constant and thermal expansion coefficient, the crystal quality and surface morphology of the GaN are far from satisfactory. SiC is a good alternative for free-standing GaN substrate due to the relatively

low lattice mismatch to GaN. Nevertheless, it is still very expensive, making it much less attractive for the mass production.

Sapphire (Al_2O_3) is the most commonly used substrate for epitaxial growth of GaN which offers the best compromise between achievable crystal quality and price. It is generally considered as the most suitable substrate because of its widespread availability, good thermal stability, mature manufacturing technology, relatively low cost and lattice matching with GaN. Moreover, since the bulk sapphire crystal is attainable, it can be cut in various crystalline orientations, making it possible to serve as substrates for growth of non-polar and semi-polar GaN. So far, the (10-12) r-plane and (10-10) m-plane sapphire are employed to grow non-polar and semi-polar GaN, respectively.

2.6.5. Crystal Quality Issue

The schematic diagram of the a-plane non-polar GaN grown on r-plane sapphire substrate is shown in Figure 2.12, where orientations of both GaN and sapphire are highlighted. Owing to the asymmetrical growth nature, the lattice mismatches between a-plane GaN and r-plane sapphire along c- and m-axes are different (~1% along c-axis and 16% along m-axis). The epitaxial relationship between the semi-polar GaN and m-plane sapphire is illustrated in Figure 2.13. The GaN c-plane is inclined to the sapphire surface by 58.4 °, and the projection of the [0001] GaN on the sapphire surface is parallel to the sapphire c-axis. The lattice mismatches between GaN and sapphire along the c-projection and m-direction are ~ 6.7% and 15.9%, respectively.

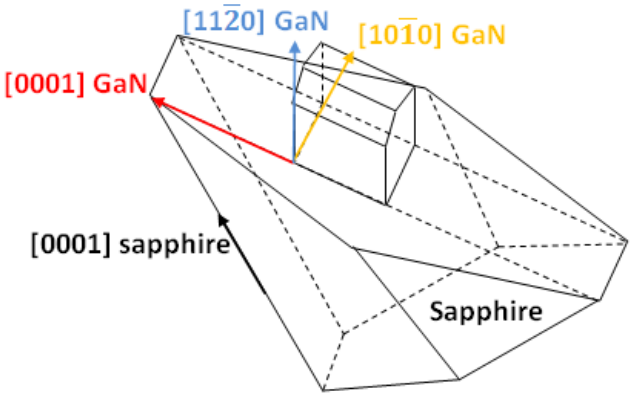

Fig. 2.12: Schematic representation of non-polar a-plane GaN grown on r-plane sapphire.

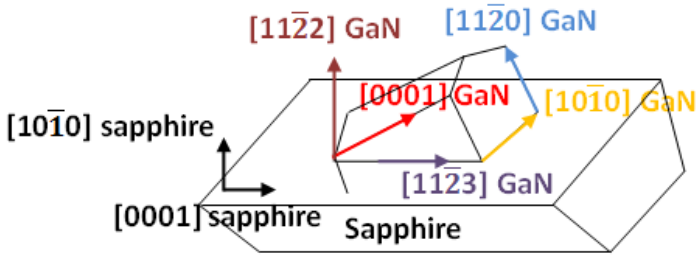

Fig. 2.13: Epitaxial relationship between (11-22) GaN and m-plane sapphire.

Due to the large lattice mismatch between GaN and sapphire, the non-polar and semi-polar GaN grown on sapphire substrates suffer from a high density of defects such as threading dislocations (TDs) (~10^{10} cm^{-2}) and basal stacking faults (BSFs) (~10^{5} cm^{-1}). Figure 2.14 (a) shows the full width at maximum (FWHM) of X-ray rocking curves for non-polar GaN along different azimuth angles, where the crystal quality is fairly poor, with a value typically above 600 arc sec. The best report achieved so far reduces it down to ~400 arc sec [43]. The dense dislocations and stacking faults act as non-radiative recombination centres and charge scattering centres and can tremendously deteriorate the optical properties, as shown in Figure 2.14 (b). The near band edge emission (NBE) is much lower than the emission from the basal stacking fault (BSF) and donor-acceptor pair (DAP). Therefore, it is crucial to improve the GaN film crystalline quality.

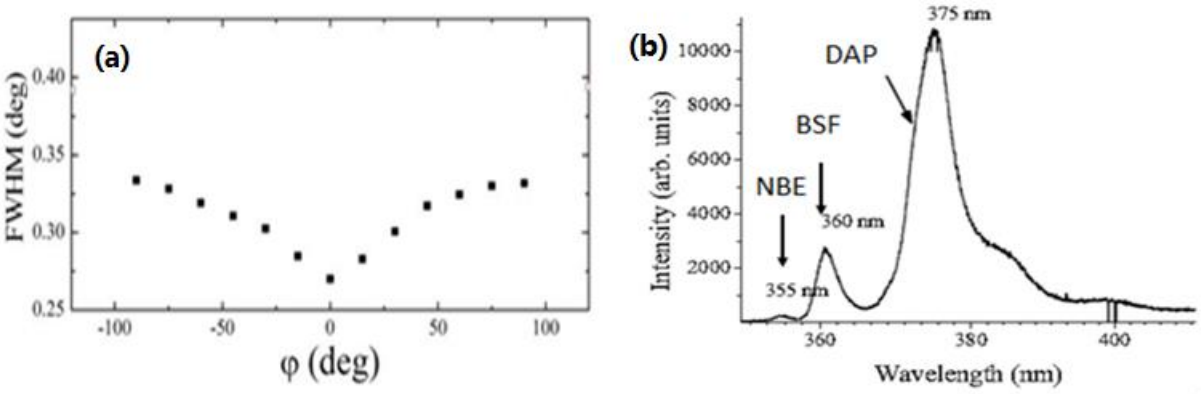

Fig. 2.14: (a) XRD rocking curves of non-polar GaN grown on r-plane sapphire, (b) low temperature photoluminescence (10K) of non-polar GaN on r-plane sapphire. Note the BSF (basal stacking fault) and DAP (donor-acceptor pair luminescence) emission dominate the spectrum. [44]

2.6.6. Epitaxial Growth Issue

As stated in 2.6.4, sapphire substrates have been well accepted for growth of GaN films despite the big mismatches. However, high quality GaN epitaxial films were difficult to be obtained at early times. In 1986, H. Amano invented a two-step growth method and obtained crack-free film for the first time, as shown in Figure 2.15 (e) [13]. The basic idea is illustrated by Figure 2.15(e). Simply, a thin AlN was deposited at low temperature (500-600^{o}) on the substrate (Figure 2.15(b)). Then temperature was increased to over 1000^{o} to perform GaN growth. Under the subsequent high temperature, the AlN buffer will form polycrystalline nano-islands which act as the nucleation layer for the GaN epitaxial layer growth, as shown in Figure 2.15(c). By using this method, they finally obtained crack-free GaN film with a low dislocation density, which is verified by the XRD rocking curves as shown in Figure 2.15(d). This method has been successful in c-plane GaN growth.

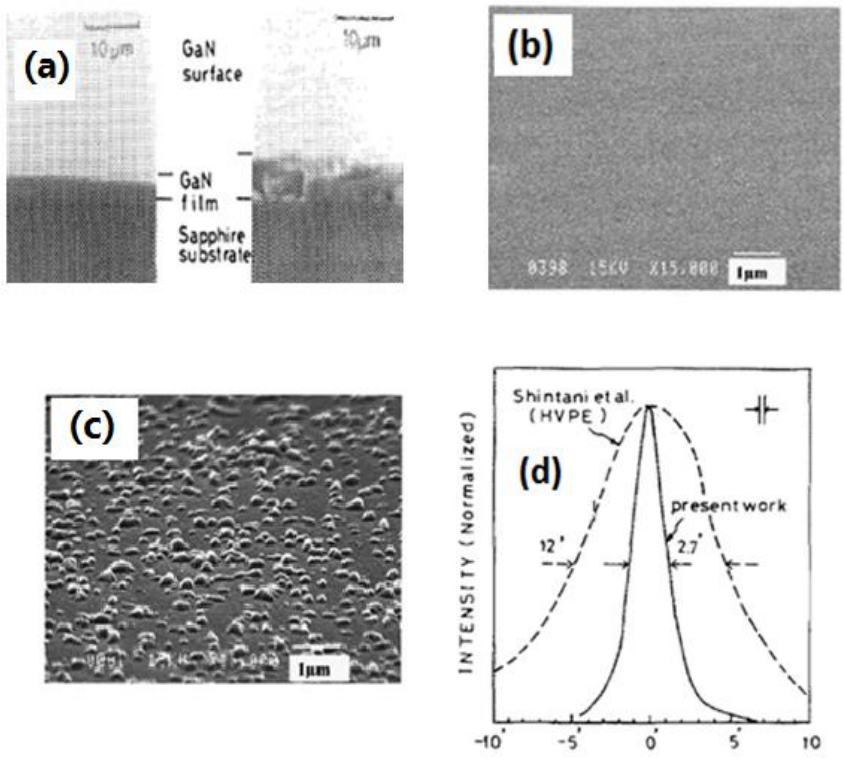

Fig. 2.15: (a) Optically flat and crack-free GaN film obtained for the first time, (b) polycrystalline AlN after high-temp annealing, (c) AlN deposited at low temperature, and (d) FWHM of XRD rocking curve massively reduced by two-step growth [13].

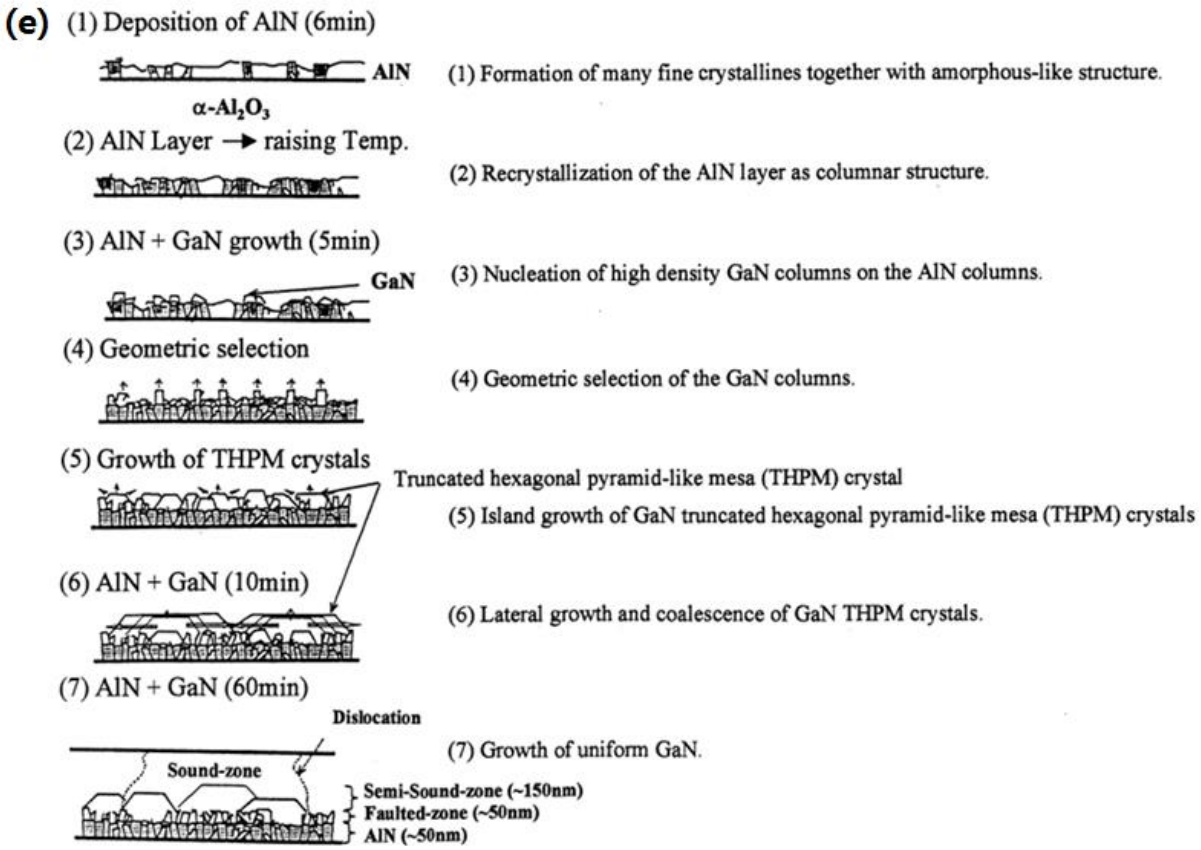

Fig. 2.15 (e): Schematic of two-step growth method [45].

In order to further reduce the dislocations introduced by the low quality AlN layer in two-step method, the Sheffield team has developed high temperature (HT) AlN buffer technology. As shown in Figure 2.16, the dislocation density can be reduced massively in the overlying GaN film [46]. There are two techniques for the growth of HT AlN buffer, namely the "GaN interlayer" technique [47] and the "multiple AlN buffer" technique [48]. For the "GaN interlayer" technique, by introducing a thin GaN interlayer on the standard high temperature (HT) AlN buffer layer prior to the growth of GaN, the dislocation penetration can be blocked by the GaN interlayer effectively. For the "multiple AlN buffer" technique, a so-called "porous AlN layer" is introduced prior to the HT AlN layer. By growing porous/HT AlN pair, the porous AlN can effectively reduce the dislocation density in the HT AlN layer.

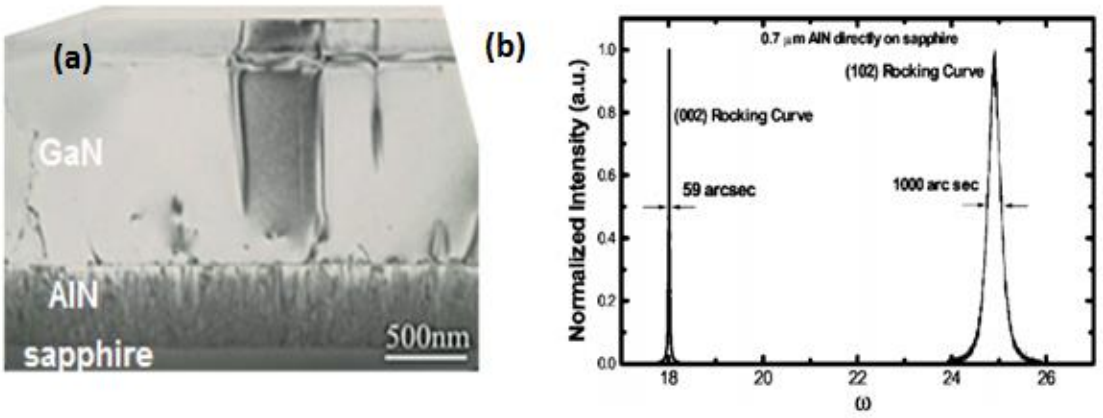

Fig. 2.16: (a) TEM image of the GaN grown on high temperature AlN layer. The dislocations density is effectively decreased in the GaN epitaxial layer; (b) XRD rocking curve, showing an extremely narrow FWHM, agrees well with the TEM observation. [49]

These AlN buffer technologies have also been applied onto the growth of non-polar and semi-polar GaN [50], where r-plane and m-plane sapphire are employed as substrates. The GaN layers grown on r-plane sapphire yields the pure a-plane crystallography, whereas the GaN grown on m-plane sapphire exhibits (11-22) and (10-13) mixed phases. It has been reported that this mixed phase of semi-polar GaN can be suppressed by the nitridation process, which is able to break surface symmetry of m-plane sapphire and make the nucleation of (11-22) GaN much easier [50, 51].

2.7. Epitaxial Overgrowth of GaN

2.7.1. Introduction and History

In order to significantly decrease the defects in the epitaxial layers, epitaxial lateral overgrowth (ELOG) techniques have been developed. The idea is to initiate the GaN growth at defined local areas of the template. When a critical thickness is achieved, GaN will coalesce in the lateral direction to form flat epitaxial films. ELOG and other growth techniques evolved from ELOG are effective approaches to achieve high-quality non-polar and semi-polar GaN on sapphire substrates, which otherwise suffer from a high density of extended defects due to the lattice-mismatches. The ELOG techniques are based on selective

area overgrowth, which requires an ex-situ surface-coating with a dielectric mask fabricated by standard photolithography and deposition methods.

In the early stage, the most common approaches for the ELOG are single step ELOG [52, 53] and double step ELOG [54]. The schematic diagrams of the growth/fabrication processes are illustrated in Figure 2.17 (a) and (b). The mask opening (mask free region) is defined as the window regions and the area on top of the masks defined as the wing region. The single step ELOG is based on the patterned SiO_2 mask and the GaN overgrowth can only initiate from the window region. The preparation of the template is comparatively simple and does not include complicated fabrication steps. However, the main drawback of this approach is that the dislocation density only in the wing region can be effectively reduced whilst threading dislocations can still penetrate through the window region. Therefore, it is difficult to realize a uniform epitaxial film by one-step ELOG in terms of crystal quality.

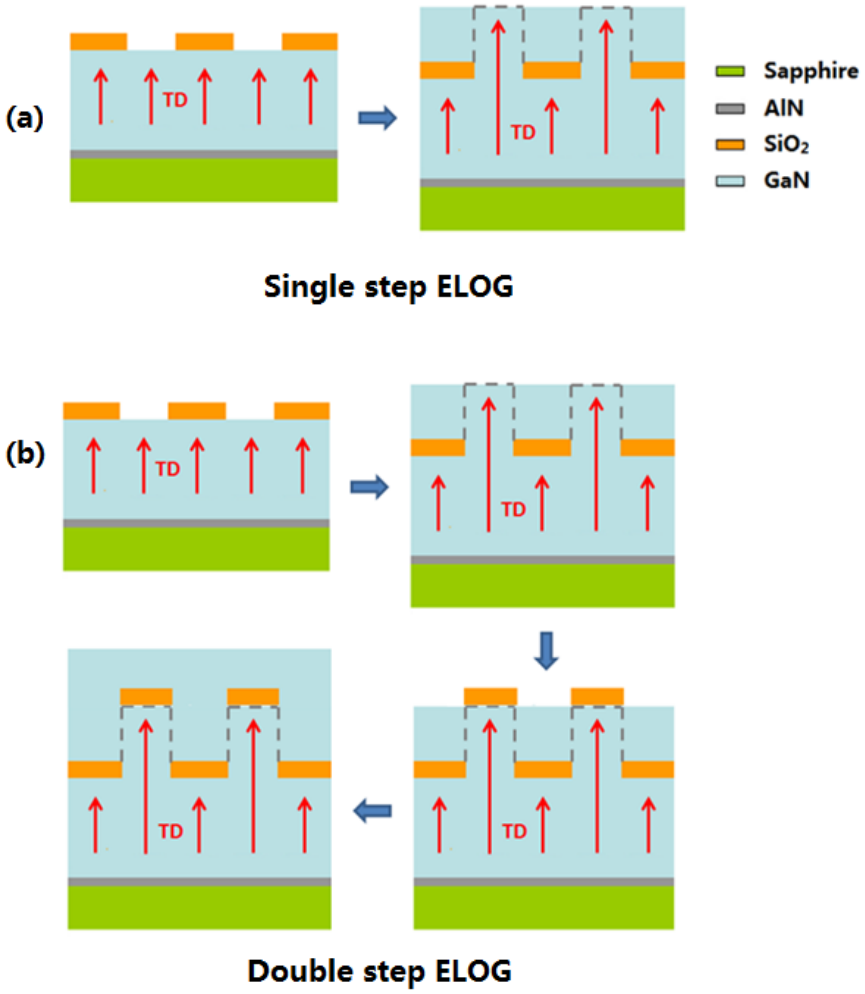

Fig. 2.17: The schematic diagram of (a) single step ELOG and (b) double step ELOG.

The double step ELOG approach includes an extra mask layer fabrication and MOCVD overgrowth. As shown in Figure 2.17 (b), the second time SiO_2 mask deposition are performed only on top of the window region which have been used for the first overgrowth. As a result, all the dislocations from the lower layers will be effectively blocked in theory. Therefore, both the sample crystal quality and uniformity can be massively improved. However, the double step ELOG is very complicated which involves three MOCVD growth runs and two fabrication steps. Besides, the reproducibility by this approach is low due to the difficulty in mask fabrication. These all make this approach less attractive and competitive.

In order to overcome the drawbacks of single and double step ELOG, another approach called sidewall ELOG has been developed [55-57]. The schematic diagram of this approach is illustrated in Figure 2.18 (a) – (d). In this approach, the GaN/AlN film is etched by inductively coupled plasma (ICP) etching through the mask opening down to the sapphire substrate. SiO_2 acts as the mask for the further epitaxial growth. The essence of this approach is to ensure the GaN growth can only be initiated from the exposed sidewalls instead of sapphire substrate or elsewhere. This approach possesses obvious advantages compared with the ELOG approaches presented above, which can be concluded as below:

1) The film crystal quality can be improved and is uniform across the whole 2-inch wafer.
2) The fabrication is very simple and effective.
3) Sapphire serves as the substrate for growth of GaN and thus it is more cost effective.

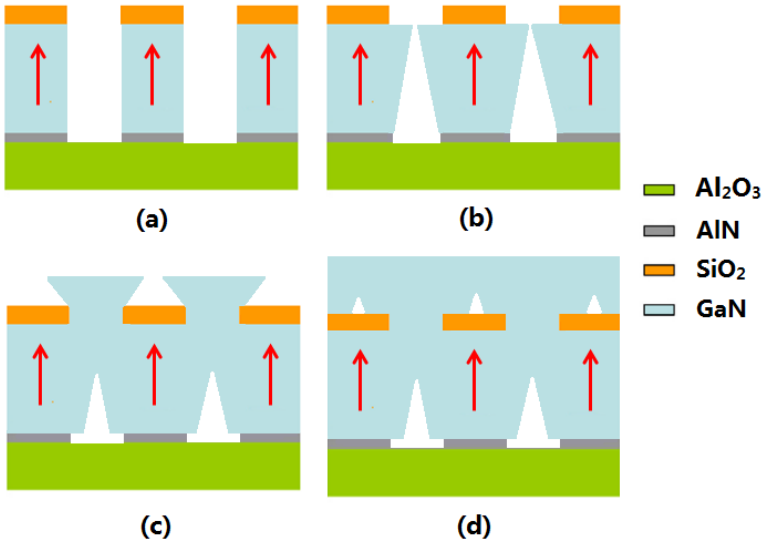

Fig. 2.18: The schematic diagram of the sidewall ELOG: (a) stripe feature showing mask openings, (b) GaN growth from the sidewall, (c) GaN growth along vertical direction after first coalescence, and (d) lateral growth over the mask and second coalescence.

2.7.2. Major Challenges

As the conventional ELOG approaches involve the overgrowth on GaN patterned with tens of micro-scaled striped feature, the dislocations only in the region under the mask stripes are effectively blocked. The growth process potentially causes a non-uniformity issue in terms of crystal quality. Furthermore, an atomically flat surface cannot be obtained till the overgrown layer reaches 10-20 μm thickness. These drawbacks make these techniques less competitive. Very recently, a simple ELOG using self-organized nano-masks has been proposed for growth of non-polar GaN (a-plane GaN) and some good results have been achieved [58, 59]. However, further improvement is still required in order to compete with the conventional ELOG approaches.

2.8. Etching of GaN

2.8.1. General Introduction

Owing to the chemical inertness and high hardness, GaN is an ideal semiconductor for being used in harsh environments and under extreme conditions. However, these features also pose a major challenge for the structure and device processing. Currently, dry etching and wet etching are commonly used for GaN structure processing. Dry etching techniques include Ion Beam Etching (IBE), Gaseous Chemical Etch (GCE), reactive ion etching (RIE), and inductively coupled plasma (ICP). Wet etching methods include chemical etching, photochemical etching, and photoelectrical chemical etching. In this section, various etching techniques are reviewed and their advantages and disadvantages are comparatively discussed.

2.8.2. Dry Etching

Dry etching is often realized by removal of a material by exposing the semiconductor under bombardment of the reactive ions. Compared with wet etching, dry etching techniques are preferred for the GaN structure and device processing due to good material selectivity, high etch rate, flexible control of the etch process and high anisotropy [60]. The dry etching process normally involves chemical (GCE) or physical (IBE) process or a combination of both (RIE, ICP). The chemical etching process refers to removal of material by chemical

reaction between the etchants and the material surface. This type of etching is isotropic and has a high selectivity. Physical etching process involves bombardment of the high energy ions to the material surface. The physical etching is anisotropic and the selectivity of the material over the mask is comparatively low. The most common dry etching techniques for III-nitride materials are performed by RIE and ICP [61, 62]. The RIE etching involves both chemical and physical interactions by using high kinetic energy reactive gases. In the RIE etching, the gases are ionized and accelerated towards the sample by a strong electric field, followed by the bombardment and chemical reaction with the target material. The ICP etching refers to a system where the plasma is generated by an RF source and confined in a small volume by an inductance coil to form a high density; meanwhile an extra RF source is applied to the lower electrode to accelerate the ions to the substrate to enhance the ion bombardment process. Therefore, the plasma density and the plasma energy can be controlled independently in the ICP system. The ICP etching also includes both chemical and physical processes. Compared with RIE etching, ICP etching can achieve a faster etching rate because of the higher ion density and a reduced surface damage due to the lower ion energy [63]. A more detailed introduction of RIE and ICP etching is discussed in Chapter 3.

Sheu et al have reported that GaN films could be etched by ICP using Cl_2/Ar [64], with a high anisotropy and a fast etch rate. In this process, the Cl radicals are generated by the RF power, which can chemically react with GaN and form volatile etch products. The Ar can physically bombard the GaN along vertical direction in order to achieve anisotropic etching [67]. However, this physical etching process can lead to the serious damage on the sample surface, which may have a negative effect on the following fabrication or device performance. One possible way to eliminate this negative effect is to perform an extra wet etching so that the damaged surface can be dissolved into the etchants.

2.8.3. Wet Etching

In general, wet etching in semiconductors refers to the oxidation of the semiconductor, followed by the dissolution of the oxides into the solvent. So far, the wet etching method has been extensively used for processing and characterizing GaN. First of all, the wet etching techniques can be used for evaluation of the defects density in GaN, as defect has a faster etch rate than the defect-free region. Secondly, wet etching is used to heal the damaged GaN

surface associated with the dry etching. This will be intensively discussed in Chapter 5. Furthermore, etchants such as KOH can be used to identify the polarity of GaN surface [66]. Based on different etching mechanisms, wet etching of semiconductor materials can be classified into two types: chemical etching and photoelectrical chemical etching. In chemical etching, the reactive species from the etchants can break the bonds of a semiconductor and form the oxidised material [69], which can be dissolved into the etchants. In some cases, an extra light source can also be hit onto the etchants in order to assist the etching process, either to enhance the etch rate or to analyse and visualize the defects. This is named photo-assisted chemical etching (PCE). One typical etchant for GaN is aqueous potassium hydroxide (KOH). Some groups have reported that only the N-polar GaN can be etched by KOH solution at 26^{o}C, where triangular shaped pyramids can be formed; whereas the morphology of the Ga-face GaN does not change under the same etching conditions [67]. The schematic representation of the N-polar GaN etched by KOH is illustrated in Figure 2.19. The hydroxide ions (OH^-) are adsorbed on the sample surface, followed by reaction with Ga to form gallium oxide (Ga_2O_3). For Ga-face GaN, when KOH removes the first Ga layer, each nitrogen atom on the surface layer has three dangling bonds, which can effectively repulse the OH^- and stop the further etching. That is the reason why KOH cannot etch the Ga-face GaN. On the other hand, for N-face GaN, when the first layer of Ga is removed by KOH, each nitrogen atom has only one dangling bond. Therefore, the Ga atoms in the next layers can be etched continuously [68].

Another type of etchant for GaN is phosphoric acid (H_3PO_4), which produces similar results as for KOH etching of GaN. The N-face GaN can be etched very quickly, while only defects in the Ga-face GaN can be etched by H_3PO_4 with the defect-free regions remaining unchanged [69]. The wet etching process have several advantages over dry etching: low cost, easy to implement, high etch rate, low surface damage and high etching selectivity. However, one major limit of the wet etching is the isotropic etch in materials, which greatly hinders its applications especially in creating patterned structures.

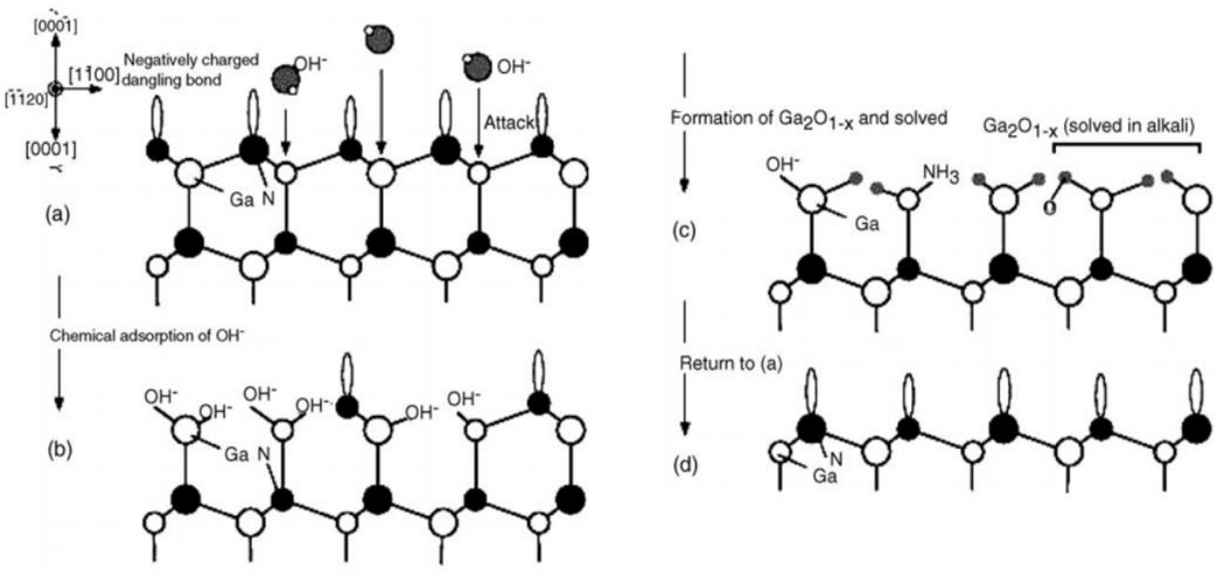

Fig. 2.19: Schematic representation of the N-face GaN etched by KOH solution [68]

References

1. http://www.doitpoms.ac.uk/tlplib/semiconductors/energy_band_intro.php
2. http://www.digplanet.com/wiki/Direct_and_indirect_band_gaps
3. J. Li, K. B. Nam, M. L. Nakarmi, J. Y. Lin, H. X. Jiang, P. Carrier, and S. Wei, Appl. Phys. Lett. **83**, 5163 (2003).
4. http://gorgia.no-ip.com/phd/html/thesis/phd_html/node4.html
5. https://www.nde-ed.org/EducationResources/CommunityCollege/Materials/Structure/point_defects.htm
6. http://oregonstate.edu/instruct/engr322/Exams/Previous/S98/ENGR322MT2.html
7. J. Bai, T. Wang, P. J. Parbrook, and A. G. Cullis, Appl. Phys. Lett. **89**, 131925 (2006).
8. C. Stampfl, and C. G. Van de Walle, Phys. Rev. B **57**, R2033 (1998).
9. R. J. Malik, "III-V Semiconductor Materials and devices", north-Holand (1989).
10. S. C. Jain, M. Willander, J. Narayan, and R. Van Overstraeten, J. Appl. Phys. **87**, 965 (2000).
11. R. J. Molnar, W. Götz, L. T. Romano, and N. M. Johnson, J. Cryst. Growth **178**, 147 (1997).
12. S. Nakamura, Y. Harada, and M. Seno, Appl. Phys. Lett. **58**, 2021 (1991).
13. H. Amano, N. Sawaki, I. Akasaki, and Y. Toyoda, Appl. Phys. Lett. **48**, 353 (1986).
14. M. A. L. Johnson, Z. Yu, J. D. Brown, F. A. Koeck, N. A. El-Masry, H. S. Kong, J. A. Edmond, J. W. Cook, and J. F. Schezina, MRS Internet J. Nitride Semicond. Res. **4S1**, G5.10 (1999).
15. H. Moffat, and K. F. Jensen, J. Cryst. Growth **77**, 108 (1986).
16. H. P. Maruska, and J. J. Tietjen, Appl. Phys. Lett. **15**, 327 (1969).
17. N. Kuwano, Y. Nagatomo, K. Kobayashi, K. Oki, S. Miyoshi, H. Yaguchi, K. Onabe, and Y. Shiraki, Jpn. J. Appl. Phys. **33**, 18 (1994).
18. H. Xia, Q. Xia, and A.L. Ruoff, Phys. Rev. B **47**, 12925 (1993).
19. H. Morkoc, ''General Properties of Nitrides'', Wiley online Library (2009).
20. S. A. Kukushkin, A. V. Osipov, V. N. Bessolov, B. K. Medvedev, V. K. Nevolin, and K. A. Tcarik, Rev. Adv. Mater. Sci. **17**, 1 (2008).
21. Lecture note for EEE6217, Department of Electronic and Electrical Engineering, The University of Sheffield, UK.
22. M. L. Nakarmi, N. Nepal, J. Y. Lin, and H. X. Jiang, Appl. Phys. Lett. **86**, 261902 (2005).

23. J. Li, K. B. Nam, M. L. Nakarmi, J. Y. Lin, H. X. Jiang, P. Carrier, and S. Wei, Appl. Phys. Lett. **83**, 5163 (2003).
24. J. Wu, W. Walukiewicz, K. M. Yu, J. W. Ager, E. E. Haller, H. Lu, W. J. Schaff, Y. Saito, and Y.Nanishi, Appl. Phys. Lett. **80**, 3967 (2002).
25. S. Nakamura, M. Senoh, and T. Mukai, Jpn. J. Appl. Phys., **32**, L8 (1993).
26. Y. Narukawa, M. Ichikawa, D. Sanga, M. Sano, and T. Mukai, J. Phys. D: Appl. Phys. **43**, 354002 (2010).
27. S. Nakamura and G. Fasol, The Blue Laser Diode: GaN Based Light Emitters and Lasers (Springer, Berlin, 1997).
28. P. Waltereit, O. Brandt, A. Trampert, H. T. Grahn, J. Menninger, M. Ramsteiner, M. Reiche, and K. H. Ploog, Nature (London) **406**, 865–868 (2000).
29. F. Bernardini, V. Fiorentini, and D. Vanderbilt, Phys. Rev. B **56**, R10024 (1997).
30. D. A. B. Miller, D. S. Chemla, T. C. Damen, A. C. Gossard, W. Wiegmann, T. H. Wood, and C. A. Burrus, Phys. Rev. Lett. **53**, 2173 (1984).
31. T. Takeuchi, H. Amano, and I. Akasaki, Jpn. J. Appl. Phys. **39**, 413 (2000).
32. A. E. Romanov, T. J. Baker, S. Nakamura, and J. S. Speck, J. Appl. Phys. **100**, 023522 (2006).
33. Y. Zhao, Q. Yan, C. Y. Huang, S. C. Huang, P. S. Hsu, S. Tanaka, C. C. Pan, Y. Kawaguchi, K. Fujito, C. G. Van de Walle, J. S. Speck, S. P. DenBaars, S. Nakamura, and D. Feezell, Appl. Phys. Lett. **100**, 201108 (2012).
34. P. D. Mierry, T. Guehne, M. Nemoz, S. Chenot, E. Beraudo, and G. Nataf, Jpn J. Appl. Phys. Part 2 **48**, 031002 (2009).
35. T. Sasaki and S. Zembutsu, J. Appl. Phys. **61**, 2533 (1986).
36. R. Armitage and H. Hirayama, Appl. Phys. Lett. **92**, 092121 (2008).
37. 10. M. Frentrup, S. Ploch, M. Pristovsek, and M. Kneissl, Phys. Status Solidi B **248**, 583 (2011).
38. Z. Bougrioua, M. Laügt, P. Vennégues, I. Cestier, T. Gühne, E. Frayssinet, P. Gibart, and M. Leroux, Phys. Status Solidi A **204**, 282–289 (2007).
39. S. Ploch, M. Frentrup, T. Wernicke, M. Pristovsek, M. Weyers, and M. Kneissl, J. Cryst. Growth **312**, 2171 (2010).
40. Q. Sun, B. Leung, C. D. Yerino, Y. Zhang, and J. Han, Appl. Phys. Lett. **95**, 231904 (2009).
41. J. S. Speck and S. J. Rosner, Physica B **24-32**, 273 (1999).
42. D. Cherns, S. J. Henley, and F. A. Ponce, Appl. Phys. Lett. **78**, 2691 (2001).

43. H. Song, J. Suh, E. K. Kim, K. H. Baik, and S.-M. Hwang, J. Cryst. Growth **312**, 3122 (2010).
44. F. Ranalli, P. J. Parbrook, J. Bai, K. B. Lee, T. Wang and A. G. Cullis, Phys. Stat. Soli. C, **6,** S780-S783, (2009).
45. K. Hiramatsu, S. Itoh, H. Amano, I. Akasaki, N. Kuwano, T. Shiraishi, and K. Oki, J. Crystal Growth **115**, 628 (1991).
46. T. Wang, K. B. Lee, J. Bai, P. J. Parbrook, R. J. Airey, Q. Wang, G. Hill, F. Ranalli and A. G. Cullis Appl. Phys. Lett. **89**, 081126 (2006).
47. Q. Wang, Y. P. Gong, J. F. Zhang, J. Bai, F. Ranalli and T. Wang Appl. Phys. Lett. **95**, 161904 (2009).
48. T. Wang, J. Bai, P. J. Parbrook and A. G. Cullis Appl. Phys. Lett. **87**, 151906 (2005).
49. X. Ni, Y. Fu, Y. T. Moon, N. Biyikli, and H. Morko ç J. Cryst. Growth **290**, 166 (2006).
50. Q. Sun, B. Leung, C. D. Yerino, Y. Zhang, and J. Han, Appl. Phys. Lett. **95**, 231904 (2009).
51. T. Wernicke, C. Netzel, M. Weyers, and M. Kneissl, Phys. Status Solidi C **5**, 1815 (2008).
52. M.D. Craven, S.H. Lim, F. Wu, J.S. Speck, and S.P. DenBaars, Appl. Phys. Lett. **81**, 1201 (2002).
53. B. A. Haskell, F. Wu, M. D. Craven, S. Matsyda, P. T. Fini, T. Fujii, K. Fujito, S. P. DenBaars, J. S. Speck, and S. Nakamura, Appl. Phys. Lett. **83**, 644 (2003).
54. C. Chen, J. Zhang, J. Yang, V. Adivarhan, S. Rai, S. Wu, H. Wang, W. Sun, M. Su, Z. Gong, E. Kuokstis, M. Gaevski, and M.A. Khan, Jpn. J. Appl. Phys. **42**, L818 (2003).
55. K. Linthicum, T. Gehrke, D. Thomson, E. Carlson, P. Rajagopal, T. Smith, D. Batchelor, and R. F. Davis, Appl. Phys. Lett. **75**, 196 (1999).
56. T. S. Zheleva, S. A. Smith, D. B. Thomson, K. J. Linthicum, P. Rajagopal, R. F. Davis, J. Electron. Mater., **28**, L5 (1999).
57. B. Imer, F. Wu, S. P. DenBaars, and J. S. Speck, Appl. Phys. Lett. **88**, 061908 (2006).
58. S. C. Ling, C. L. Chao, J. R. Chen, P. C. Liu, T. S. Ko, T. C. Lu, H. C. Kuo, S. C. Wang, S. J. Cheng, and J. D. Tsay, J. Cryst. Growth **312**, 1316 (2010).
59. S. C. Ling, C. L. Chao, J. R. Chen, P. C. Liu, T. S. Ko, T. C. Lu, H. C. Kuo, S. C. Wang, S. J. Cheng, and J. D. Tsay, Appl. Phys. Lett. **94**, 251912 (2009).
60. S. A. Smith, C. A. Wolden, M. D. Bbremser, A. D. Hanser, R. F. Davis, and W. V. Lampert, Appl. Phys. Lett. **71**, 3631 (1997).

61. M. E. Lin, Z. Ma, F. Y. Huang, Z. F. Fan, L. H. Allen, and H. Morkoc, Appl. Phys. Lett. **64**, 1003 (1994).
62. R. J. Shul, G. B. McClellan, S. A. Casalnuovo, D. J. Rieger, S. J. Pearton, C. Constantine, and C. Barratt, Appl. Phys. Lett. **69**, 1119 (1996).
63. http://wcam.engr.wisc.edu/Public/Reference/PlasmaEtch/Plasma%20paper.pdf
64. J. K. Sheu, Y. K. Su, G. C. Chi, M. J. Jou, C. C. Liu, C. M. Chang, and W. C. Hung, J. Appl. Phys. **85**, 1999 (1970).
65. Y. C. Lin, S. J. Chang, Y. K. Su, S. C. Shei, *and* S. J. Hsu, *Mater. Sci. Eng. B* **98**, 60 *(*2003*).*
66. T. Palacios, F. Calle, M. Varela, C. Ballesteros, E. Monroy, F.B. Naranjo, M.A. Sánchez-Garcia, E. Calleja, E. Munöz, Semicond. Sci. Technol. **15**, 996 (2000).
67. Hock M. Ng, N.G. Weimann, A. Chowdhury, J. Appl. Phys. **94** ,650 (2003).
68. D. Zhuang and J. H. Edgar, Mater. Sci. Eng., R **48**, 1 (2005).
69. Y. Jung, J. Ahn, K. H. Baik, D. Kim, S. J. Pearton, F. Ren, and J. Kim, J. Electrochem. Soc. **159**, H117 (2012).

Chapter 3

Experimental Techniques

3.1. Metal Organic Chemical Vapour Deposition

Up to this date, MOCVD has become one of the most important techniques for growth of III-nitride materials and its alloys. A layout of our MOCVD system is shown in Figure 3.1. Our MOCVD system consists of 5 core parts: gas delivery and flow control system, a reaction chamber, a heater with a susceptor, pump/exhaust system, and source precursors. A schematic diagram of our MOCVD is shown in Figure 3.2. Mass flow controllers (MFC) are used to control the flow rate of reactants and carrier gases. Pressure controllers regulate the pressure of metalorganic (MO) source cylinders. A manifold is a gas switch with a number of inlets and outlets, switching flowing gas into the reactor or vent line. The gas delivery and flow control system is primarily composed of carrier gas lines, source precursor lines, upper/lower run lines, upper/lower vent lines, and makeup lines. The upper/lower vent line is connected to an exhaust system. The primary role of the makeup lines is to stabilize the pressure and gas flow in the run lines during the manifold switching.

Generally there are two main functions of the H_2/N_2 serving as the carrier gases for the Group III and V precursors and transport them to the upper and lower inlet of the showerhead. Additionally, H_2/N_2 is also constantly introduced to some certain areas of the reaction chamber during the growth in order to keep these areas clean and hence avoid contaminations, such as optical purge, reactor purge and heater purge. It is worth mentioning that the H_2 is purified by passing through a heated palladium membrane before entering the MOCVD system.

Fig. 3.1: The picture of our MOCVD.

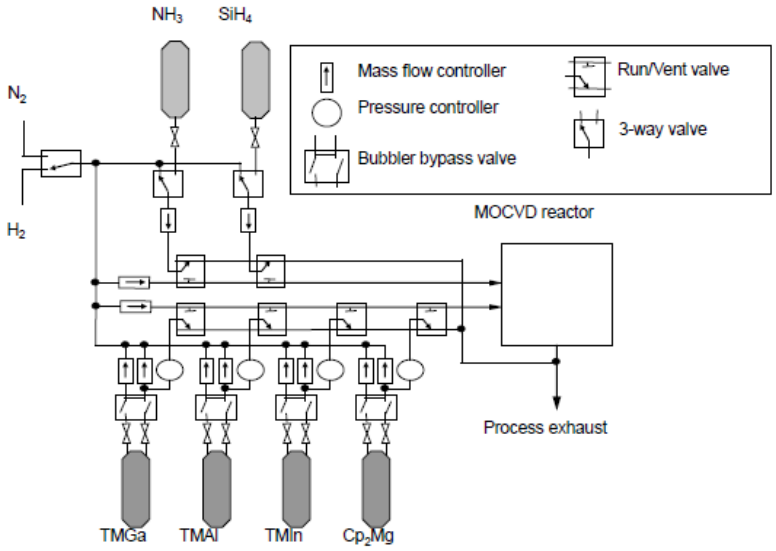

Fig. 3.2: Schematic diagram of our MOCVD set-up [1].

A schematic of a showerhead of our system is illustrated in Figure 3.3. The showerhead is designed with independent upper/lower gas inlets and outlets in order to avoid mixing of the MO sources and NH_3 before entering the reactor. The space between the showerhead gas outlets and the substrate is made to be very small to reduce the gas phase pre-reaction rate of the precursor gases. For the same reason, the cooling water is applied to circulate around the showerhead during the growth. Normally, while the heater temperature is increased up to ~1100-1200^{o}C, the showerhead temperature is only ~150^{o}C. In addition, the cooling water can also keep the temperature of the reaction chamber low, in order to make sure that the MOCVD is operated safely and securely.

Below the showerhead is the MOCVD reaction chamber, a cylindrical cavity made of stainless steel. A susceptor with a capacity of 3×2-inch substrates is installed in the chamber, and wafers are loaded on top of it during the growth. The susceptor is made of graphite and coated with silicon carbide (SiC) in order to avoid the chemical reactions and physical abrasions. It is rotating at a constant speed (100 rpm) during the growth in order to achieve the uniform growth of thin films. A heating element is placed underneath the susceptor in order to provide a high temperature during the growth. A vacuum pump is employed to create a low pressure in the reactor chamber [2].

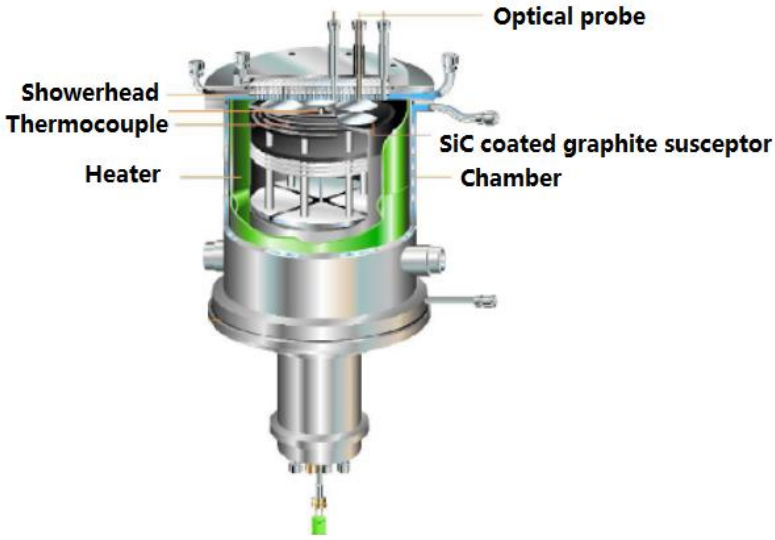

Fig. 3.3: Schematic view of the MOCVD reaction chamber [3].

For growth of III-nitride semiconductors by MOCVD, metalorganic compounds such as trimethylgallium (TMG), trimethylaluminum (TMA) and trimethylindium (TMI) serve as the metal source; and ammonia (NH_3) are used as the nitrogen source. The metalorganic and NH_3 pass through the showerhead and then reach the heated substrate in order to chemically form GaN. During the growth, the substrate temperature has to be increased up to ~1000-1100^{o}C. This is because the bonding energy of NH_3 is quite high, which can only be decomposed at high temperature. Moreover, a high temperature is required in order to enhance the migration of Ga and N. The chemical reaction can be written as follows:

$$(CH_3)_3Ga + NH_3 \xrightarrow[H_2/N_2\ \text{ambient}]{1000 - 1100^{\circ}C} GaN + 3(CH_4)\uparrow$$

3.2. Material Characterization

3.2.1. Bede D1 High Resolution X-ray Diffraction (HRXRD)

X-rays, generated by bombarding a target metal with accelerated electrons, are a powerful way to analyze crystal structure because of its similar wavelength with the lattice constant. In our X-ray diffractometer (XRD), Cu K_α radiation with a wavelength of 1.54 Å is used as the source. The XRD is basically composed of three main parts: an X-ray tube, a sample stage and an X-day detector. A schematic representation of the XRD is shown in Figure 3.4 (a). The X-rays are collimated and directed to the sample attached on the sample stage, followed by X-ray diffraction from different planes of the crystal. These diffracted X-ray beams are then directed to the detector. As shown in Figure 3.4 (b), the principle of XRD can be explained by the Bragg's Law, $a+ b=2d\cdot\sin\theta=k\lambda$, where a+b is equal to the path difference of two waves, d is the distance between atomic layers, k is the order of diffraction and λ is the X-ray wavelength [4]. Therefore, the Bragg angles of GaN for different diffraction planes can be calculated. Typical Bragg angles of c-plane, semi-polar and non-polar planes are listed in Table 3.1.

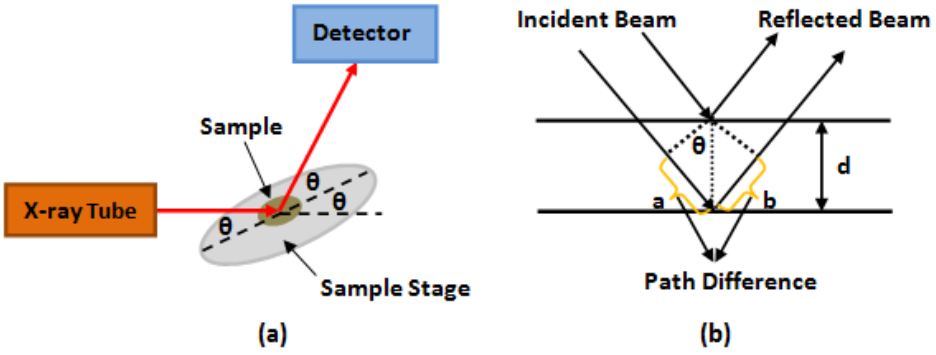

Fig. 3.4: (a) Schematic diagram of our XRD set-up and (b) geometrical diagram of X-ray diffraction.

	Bragg angle (deg)
(0001) c-plane GaN	17.2846
(11-20) non-polar GaN	28.8756
(11-22) semi-polar GaN	34.5294

Table 3.1: Bragg angle of c-plane, non-polar and semi-polar GaN.

The crystal quality of GaN can be evaluated by performing the XRD rocking curve scan, in which the detector is fixed at 2θ position and the sample is scanned around the Bragg angle θ = ω. A diffraction peak can be obtained by applying the rocking curve scan due to constructive interference. The crystal quality of GaN can be evaluated by measuring the full width at half maximum (FWHM) of the rocking curve, and a smaller value of FWHM indicates better crystal quality. If the sample is ideally free from any dislocation, then the rocking curve will theoretically become a straight line and the FWHM will be equal to 0.

As an example, XRD rocking curves for c-plane GaN grown using our high temperature AlN buffer is shown in Figure 3.5. A strong peak can be observed at 17.2846^{o} with FWHM of only 61 arcsec, while the typical FWHM of standard GaN grown on sapphire by the widely used two-step growth approach is around 280 arcsec.

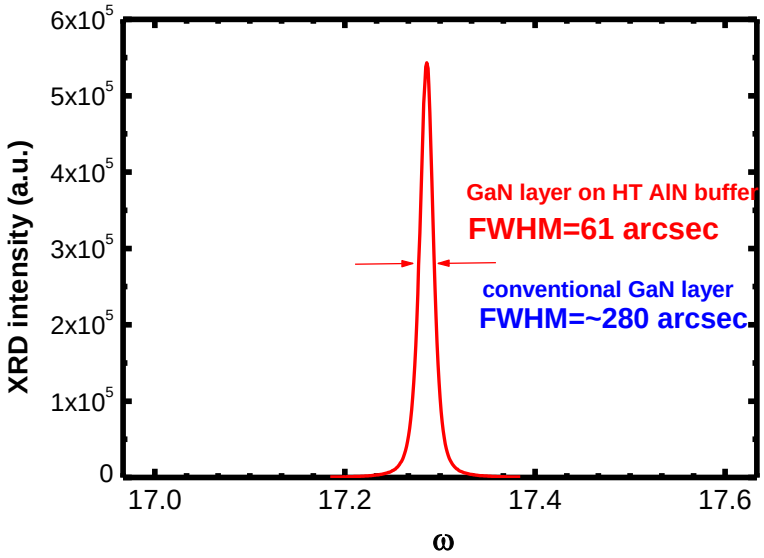

Fig. 3.5: XRD rocking curves for c-plane GaN grown using our developed high temperature AlN buffer.

3.2.2. Optical Microscope

An optical microscope employs visible light to produce magnified images for small features. It consists of an eyepiece lens, an objective lens, a sample stage and an illuminator. It is a very powerful tool for inspecting small features for a wide range of materials. A typical

optical microscope has a magnification from 10 to ~10^4 times, which is able to detect small features on a micrometer scale. An optical microscope is advantageous for low cost, ease of operation and convenience. However, it is unable to inspect features down to a nano-meter scale due to the diffraction limit. Another type of microscopy is known as Nomarski interference Constrast or Nomarski microscopy, which is used to enhance the contrast in unstrained transparent samples. It works by separating a polarized light source into two polarized mutually coherent parts and recombined before observation. It is able to gain information about the optical path length of the sample in order to check invisible features.

3.2.3. Scanning Electron Microscopy

Scanning electron microscopy (SEM) is a very powerful microscope which uses electrons rather than optical methods to produce high resolution images of sample surfaces. Typically, SEM has a magnification ranging from 10 to 10^5 times, which gives the resolution better than 10 nm due to the extremely short wavelength of electron beam. The SEM configuration is illustrated in Figure 3.6 (a). The electron is emitted from the electron gun and is accelerated by the anode. Subsequently, the electron beam is collimated by the condenser lenses. It is then deflected by the scan coils and focused by the objective lenses. The focused primary electrons interact with the sample and create secondary electrons which are collected and detected by the secondary electron detector. These secondary electrons are for imaging the sample surface [5]. The SEM image of the GaN micro-rod array is shown an example in Figure 3.6 (b), where the sample is measured with a 30^o perspective view.

The main advantage of SEM compared with optical microscope is that SEM has much higher resolution and magnification than optical microscope, so it is advantageous for inspection of very small features down to nano-meter scale. The preparation of sample is relatively simple and straightforward and it is also very user-friendly. SEM also has some restrictions: all measurements need to be performed in vacuum (typically 10^{-6} Torr) and samples have to be conductive. Insulating materials are not perfect for SEM measurements because the charges can easily accumulate on the sample surface and thus result in poor imaging and even sample degradation.

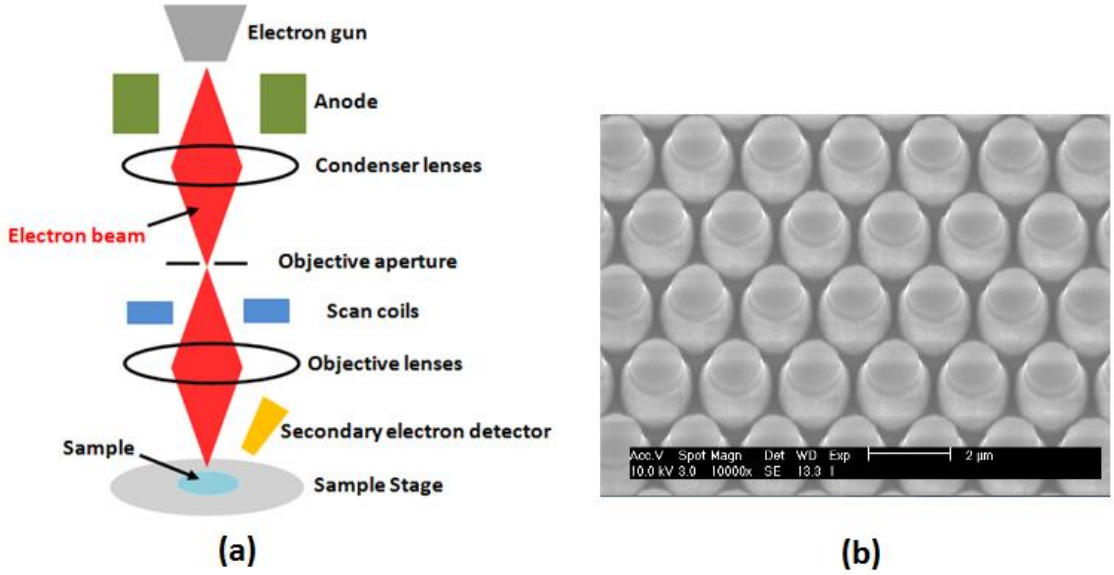

Fig. 3.6: (a) Schematic diagram of the SEM, and (b) images of our micro-rod array structure taken with Philips XL30 FEGSEM.

3.2.4. Atomic Force Microscopy

Atomic force microscopy (AFM), derived from scanning tunneling microscopy (STM), is a type of high-resolution microscope capable of providing three-dimensional information of sample surfaces on an atomic scale for both conductors and insulators. Generally, AFM is designed to be used in two main operation modes: contacting mode and tapping mode. The contacting mode may have a risk of destroying the tip or film surface. For tapping mode, the adhesion of the water film has to be overcome by the cantilever force. AFM basically scans images using a cantilever with a sharp tip at its end, which is normally made of silicon (Si) or silicon nitride (Si_3N_4). The schematic illustration of AFM is demonstrated in Figure 3.7 (a). AFM mainly consists of a laser beam, a sample stage, a position-sensitive photodetector and a feedback system. Once the sample is mounted on the stage, the tip is brought very close to the sample surface ready for the measurements. As the tip scans across the sample, the atomic force between the tip and sample surface leads to the deflection of the cantilever according to Hooke's Law. In the meantime, the laser beam is directed on the back side of the cantilever and is bounced back to the photodetector. The detector essentially measures the degree of deflection of the cantilever, and the feedback system keeps remaining a constant deflection between the tip and sample surface by adjusting the tip position marked as x, y and z. This

position information is recorded and then transferred to computer software to generate the surface morphology of the sample [6]. An example AFM image of our c-plane GaN grown using our high temperature AlN buffer is presented in Figure 3.7 (b), where the atomic steps can be clearly observed.

AFM has several advantages in comparison with SEM: firstly, AFM is capable of providing three-dimensional surface profile whereas the images in SEM is 2D. In addition, AFM can obtain a higher resolution surface than SEM. Furthermore, unlike SEM that requires scanning in high vacuum condition, AFM can be operated at atmospheric pressure. However, AFM also has some drawbacks compared with SEM. The most important one is that SEM can image a much larger area than AFM (approximately 1mm × 1mm and 100μm × 100μm respectively). Moreover, AFM scan is normally much more time-consuming than SEM: it takes at least several minutes to obtain a single AFM image whereas SEM scan can usually finish in seconds.

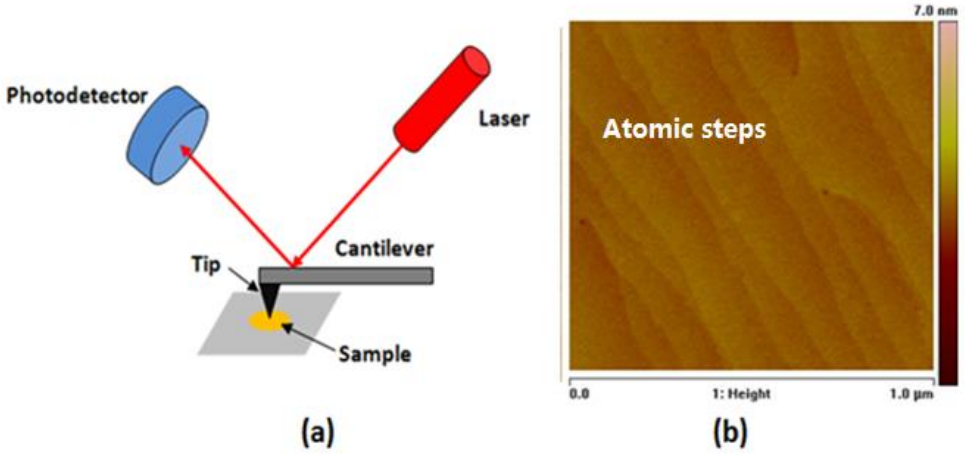

Fig. 3.7: (a) Schematic representation of AFM set-up, and (b) an example of an AFM image of atomically flat GaN epitaxial film grown on a high temperature AlN buffer by our group.

3.2.5. Transmission Electron Microscopy

Transmission electron microscopy (TEM) is a versatile technique where energetic electrons are transmitted through a sample to provide morphological and crystallographic information of the samples. Similar to SEM, TEM is able to image at a much higher resolution than optical microscope, because of the short wavelength of electrons. Generally, TEM can

provide an ultra-high resolution with maximum potential magnification of 10^6. Therefore, TEM is ideal for imaging samples on a molecular level, making it possible for analyzing material structure on a nano-scale. So far, TEM has a wide range of applications in the semiconductor analysis, especially useful for providing the topographical, morphological and crystalline information [7]. In addition, TEM is able to view crystals on a molecular level, so it can be used to detect extended defects such as dislocations and stacking faults, etc. An example of TEM image is presented in Figure 3.8, in which both structure morphology and dislocations can be clearly observed.

TEM mainly includes four parts: illumination system, projection system, object lens and a sample stage. The illuminate system generates electrons which are accelerated to high energies and then directed towards a sample. The electrons interact with the sample and scattered to a detector to form an image. The image is magnified by the projection system for viewing and analysis. The sample stage is inserted into the path of electrons, and hence it has to be very thin in order to let electrons to pass through and mitigate multiple scattering of the electrons.

TEM is a very robust instrument which has a number of advantages: firstly, it is the most powerful microscope which can provide the highest magnification; secondly, TEM is able to gain detailed information on the molecular structure and thus can yield information related to the defects. However, the equipment is very expensive and its operation is relatively complicated. Furthermore, the sample preparation is time consuming, as the sample needs to be specially prepared to a thickness about a few microns which allows electrons to transmit through.

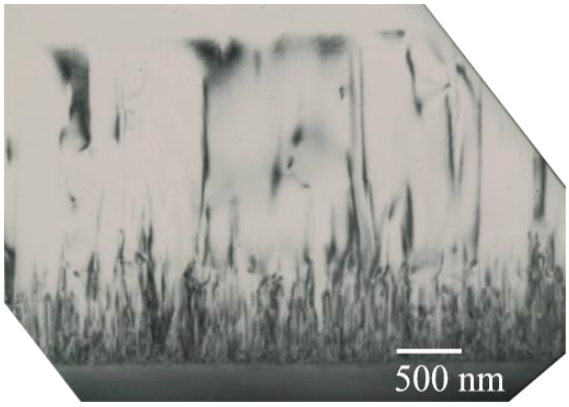

Fig. 3.8: An example TEM image measured by Phillips EM 430 of GaN grown on our porous AlN buffer by our group.

3.2.6. Photoluminescence Spectroscopy

A photoluminescence (PL) system is a very powerful non-destructive tool to study optical properties of semiconductors, and has been widely used for optical characterization of semiconductors. PL emission is defined as the process in which electrons, excited to a higher energy state by an incident electromagnetic radiation (ultraviolet, visible light and infrared), transit to their equilibrium state accompanied by radiation of photons which is detected to study the detailed energy band/level distribution of semiconductors. This radiative process occurred most commonly between states in the conduction band and valence band, and hence the emitted photon energy is equal to the band gap. However, the transition of electrons may release energy in some other forms such as lattice vibrations or electronic excitations rather than photons, which will eventually be transformed into heat energy, and this is defined as non-radiative transitions. The non-radiative process can suppress the luminescence and deteriorate the performances of semiconductor devices [8].

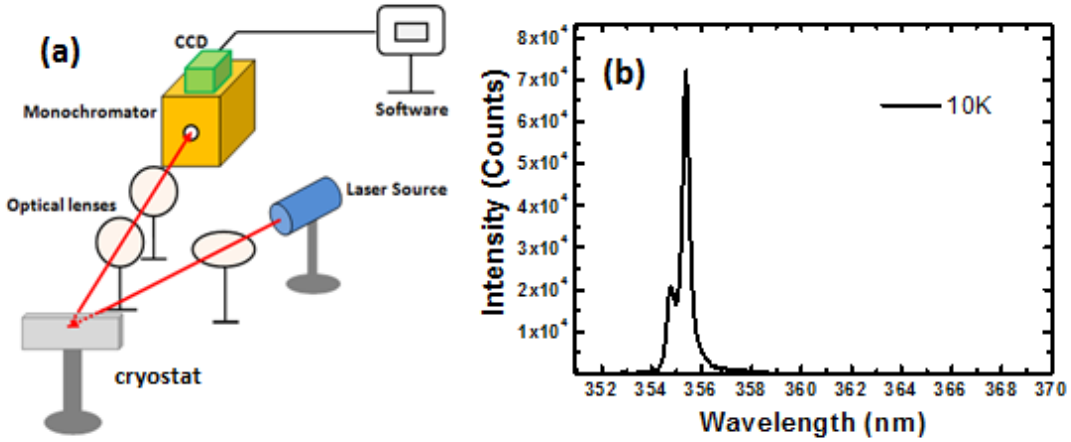

Fig. 3.9: (a) Schematic diagram of our PL set-up, (b) a typical low temperature PL (10K) spectrum of c-plane GaN, where the near band-edge emissions are observed.

PL set-up normally contains five major components: a laser used as an excitation source; optical lenses for light gathering and focusing; a cryostat for cooling sample; sample stage; a monochromator for emission dispersion; and a charge-coupled device (CCD) for luminescence detection. Figure 3.9 (a) demonstrates a schematic of our PL system. Either a 375 nm diode laser or a 325 nm He-Cd laser is used as an excitation sources study optical

properties of InGaN/GaN quantum well and GaN, respectively. The laser is focused by a convex lens and is directed on the sample. The emission from a sample is then focused by a pair of convex lenses and enters the monochromator. Finally, the CCD converts the data into digital value and the software processes the data and draws the figure showing the emission intensity as a function of wavelength.

(a) Temperature Dependent PL

The temperature dependent PL is one of the most commonly used optical measurements for evaluation and investigation of optical properties of a sample. In this set of measurement, the sample is loaded into a special chamber named cryostat which provides a low temperature down to 10 K in a vacuum. With a heating element, PL spectra can be measured in a wide range of temperatures from 10 K to 300 K. The recombination of electron and hole pair either emits photons or phonons, which are defined as radiative and non-radiative recombination, respectively. In principle, non-radiative recombination centres are frozen at a low temperature, such as 10k or below, and thus we can assume that internal quantum efficiency at such a low temperature is approximately unity (100%). Therefore, by performing the temperature dependent PL measurements, one is able to calculate the ratio between the integrated intensity of the PL spectra at 300 K and 10 K, allowing us to estimate the of IQE of a sample at room temperature. This is a widely used method to roughly estimate the IQE of GaN-based sample. As long as samples are measured under identical conditions, the approach allows an accurate comparison of IQE for different samples.

(b) Excitation Power Dependent PL

Power dependent PL is another very important type of PL measurements. Similar to temperature dependent PL, the sample is loaded into the cryostat which is cooled down to 10 K in vacuum. The PL spectra are recorded at different incident laser power (ranging from 0.1mW to 15mW, for example), with the rest of the operating conditions unchanged. By carefully study of peaks/intensities of these PL spectra, one can obtain the useful information of the tested sample. For instance, it is known that MQW structure grown on c-plane GaN suffers from the QCSE, leading to reduced optical efficiency and a red shift in the emission

energy. However, with increasing excitation power, the QCSE will be screened to some extent, thus leading to a blue shift in the emission energy. Therefore, the excitation power dependent PL measurements can be used to study the QCSE by simply examining if there is any blue shift in the emission energy with increasing excitation power.

3.3. Fabrication Techniques

3.3.1. Sample Preparation

All the fabrication procedures for overgrowth are conducted on 2-inch as grown GaN templates grown by MOCVD. As there may be some contaminations on the sample surface, it often needs to be cleaned by certain solvents prior to the fabrication. Firstly, boiling n-butyl acetate is applied to clean the sample as it has excellent solvency for oils, polymers and resins, etc. The sample soaked in n-butyl is firstly placed in the ultrasonic baths for 3 min. Next, the sample is put into acetone for 3min in order to remove the residue n-butyl solution. After that, the sample is then put into isopropyl alcohol (IPA) for another 3 min to remove the residue acetone. Finally, the sample is rinsed by de-ionized water in order to remove IPA and residue particles and impurities.

3.3.2. Physical Vapour Deposition (PVD)

Physical vapour deposition (PVD) is a process by which a thin film is deposited by means of physical evaporation. It mainly consists of three steps: 1) the target material is converted into vapour by pure physical means, either by the bombardment of high energy ions or heating; 2) The material in the gaseous state is transported to a desired substrate under ultra-low pressure; 3) the vaporized material condenses on the substrate. The PVD technique is designed for coating samples with metals such as gold, silver, nickel, etc. Metals deposited using PVD technique is normally quite hard and stable with good adhesion. PVD is also much more environmental friendly compared with the CVD techniques. However, PVD requires deposition at a very low pressure of approximately ~$2x10^{-6}$ Torr in order to minimize the impurity concentration within the chamber and hence improve the quality of the product. The PVD method basically contains two common ways: the sputter deposition which is

implemented by the bombardment of material; and thermal evaporation through heating the target material. In the process of nano-rod fabrication, the sputter deposition is applied to deposit a thin layer of gold and the thermal evaporator is employed to perform the nickel deposition.

(a) Sputter Deposition

The sputter deposition is a common way for depositing thin film materials, which uses high energy particles to bombard the target material. The momentum transfer from the particles to the target material leads to atoms ejected from the material and subsequently depositing on the substrate. The system image and schematic diagram of our direct-current (DC) sputtering chamber are illustrated in Figure 3.10 and 3.11, respectively. The model is called Denton Vacuum Explorer 14. It consists of three target sources: gold (Au), platinum (Pt), and titanium (Ti). In the system, the target material and the substrate are placed on top and bottom of the chamber. A parallel electrode is mounted in the chamber with the cathode on the target material and the substrate attached to the anode. Plasma can be generated by ionizing a sputtering gas, which then bombards the target material and releases atoms from it. Generally, in the sputtering system, the inert gases are employed as the bombarding particles as they are very difficult to undergo chemical reactions. For our sputtering system, argon (Ar) is used as the bombarding particle. Compared with helium (He) and neon (Ne), Ar has a larger mass so that it can provide higher momentum, while conversely, Ar is more cost-effective than krypton (Kr) and xenon (Xe). The sputtering chamber needs to be evacuated to a pressure normally lower than 10^{-6} Torr before deposition. Once the required pressure is achieved, the Ar gas is filled into the chamber and the pressure of the chamber becomes ~10^{-3} Torr. After that, a ~300 V voltage is applied between the electrodes and electrons from the cathode are accelerated towards the anode. These electrons can ionize the Ar atoms so that the positively charged Ar^+ ions are created. The Ar^+ ions are accelerated to the cathode and bombard the target at high energy and hence atoms can be ejected from the target and result in deposition on the substrate.

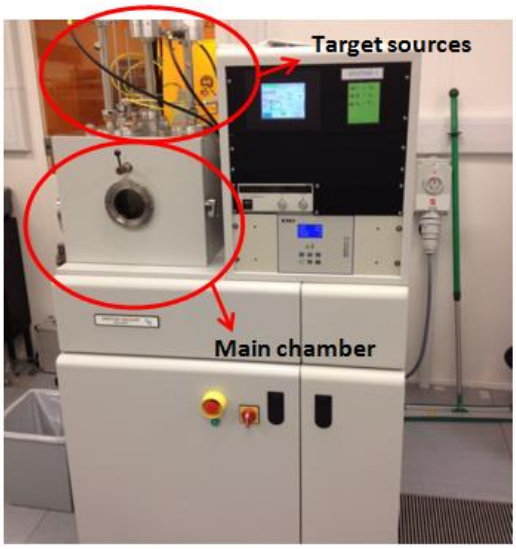

Fig. 3.10: The sputtering system image.

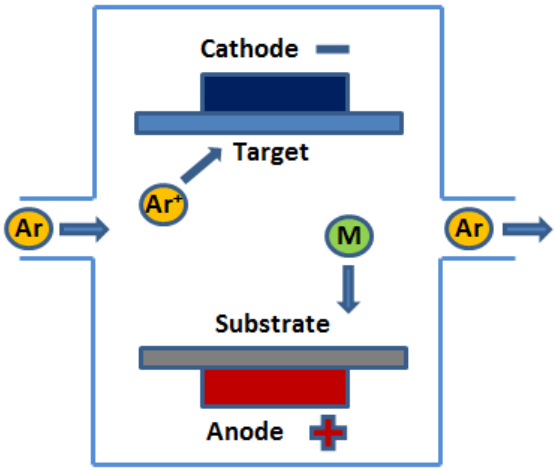

Fig. 3.11: Schematic diagram of the sputtering system.

(b) Resistive Thermal Evaporation

Resistive thermal evaporation is another commonly used technique for metal thin film deposition. The system image is shown in Figure 3.12. The deposition chamber is sealed by a glass bell jar, which is covered by an implosion guard. A combination of rotary pump and diffusion pump are applied to pump the chamber to the required low pressure. The rotary pump is firstly used for rough pump to reach a pressure of approximately $2\text{-}4\times10^{-1}$ Torr. Subsequently, the diffusion pump starts to pump the chamber down to 10^{-6} Torr. Liquid nitrogen needs to be filled through the trap in order to cool down the diffusion pump. The principle of the system consists of heating a filament by passing through large electrical current, which in turn heats the preloaded deposition material to its melting point. The

vaporized material then escapes from the filament and condenses on the cold substrate surface so that a thin film can be formed.

The schematic diagram of our resistive thermal evaporator is shown in Figure 3.13. The metal wire is firstly loaded in the refractory filament, under which the substrate is mounted. The evaporation is usually performed under low pressure of approximately 2×10^{-6} Torr. Once the low pressure is reached, a high current is used to melt the deposition metal. The deposition rate of the metal can be simply adjusted by changing the applied current. Increasing the current corresponds to a faster deposition rate, leading to more material escaping from it. For example, Ni metal can be evaporated at a current of ~30 A. The deposition rate of Ni is kept at ~0.1 nm/sec, which corresponds to a current at approximately 22 A. A crystal detector shown in the image is fitted close to the substrate in order to monitor the deposition rate and thickness.

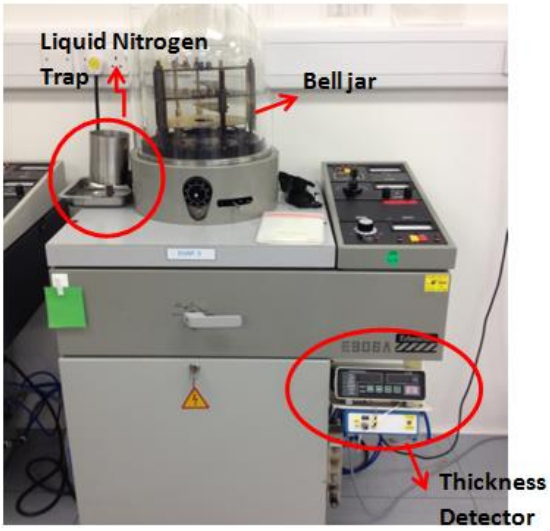

Fig. 3.12: The image of resistive thermal evaporator system.

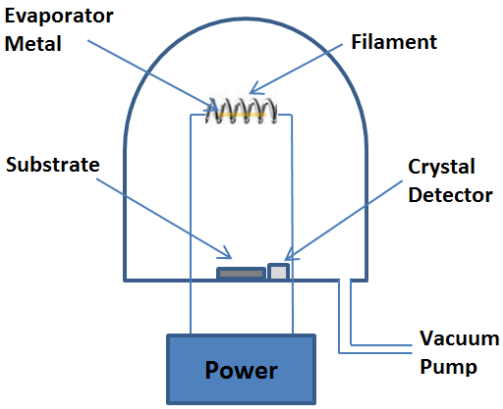

Fig. 3.13: Schematic diagram of the thermal evaporator.

Both the resistive thermal evaporator and sputter deposition can lead to high purity of film due to low deposition pressure. Thermal evaporation is cost-effective and is able to deposit more types of materials than DC sputtering system. However, DC sputtering system is more controllable and can offer a better film uniformity than the thermal evaporator, as different materials have different melting currents and the material deposition rate is very sensitive to current. Therefore, sputtering is advantageous for deposition of extra thin films. Normally, the film deposited by means of sputtering can reach sub-nanometre precision [9].

3.3.3. Plasma Enhanced Chemical Vapour Deposition (PECVD)

Plasma enhanced chemical vapour deposition (PECVD) is a process in which a variety of thin films can be deposited on substrates. The plasma is defined as a partially ionized but electrically neutral mixture which consists of ions, free radicals, free electrons and neutral particles. In the PECVD system, there are two parallel electrodes fitted on top and bottom of the chamber so that the reactant gases can be ionized to form into the plasma state. Therefore, the gas mixture in the plasma state is highly reactive and the chemical reactions can be greatly enhanced, which eventually results in the product deposited on the substrate [6]. Our PECVD model is the plasma-therm 790 series system and the system image is shown in Figure 3.14.

Generally, PECVD is advantageous due to its low operation temperature, fast deposition and high quality of the deposited dielectric films. The deposition temperature of our PECVD is typically ~300 ^{o}C. This is much lower than the standard chemical vapour deposition (CVD) technique which normally needs ~800 ^{o}C to achieve a similar quality film as PECVD. The thin films which can be deposited by PECVD are typically dielectric materials such as silicon dioxide (SiO_2) and silicon nitride (Si_3N_4). During the process of GaN nano-rod fabrication, SiO_2 is normally employed as the mask for the selective dry etching. The reactant gases for SiO_2 deposition are SiH_4, N_2O, and N_2, with their flow rates at 160 sccm, 900 sccm and 240 sccm, respectively. The deposition pressure and power are 900 mTorr and 25 w, and the deposition rate is 40nm/min. Generally, in the standard nano-rod fabrication procedure, a SiO_2 layer of 300 nm is required, that is, deposition time needs ~7.5 min.

Fig. 3.14: Plasma-therm 790 series PECVD system.

3.3.4. Rapid Thermal Annealing (RTA)

Rapid thermal annealing (RTA) is a process in which the annealing temperature can be ramped up (down) to high (low) temperatures (normally up to 1100^{o}C) at a fast rate. Our RTA model is from Mattson technology and is presented in Figure 3.15. The main chamber consists of a framework all made of SiO_2, and a 4-inch Si substrate is mounted on top and is supported by the framework. A 4-inch lid also made of Si is placed on top of the substrate so that the sample is sandwiched by two Si wafers.

Our RTA can achieve a maximum temperature of 900^{o}C. An infrared lamp is applied to heat the wafer, and the required temperature can be attained within tens of seconds. During the cooling down process, the temperature can also be brought down quickly. The available gases are nitrogen, oxygen or a mixed of them. The recipes with different annealing time and gas ambient can be set. The RTA is a very important process in semiconductor device fabrication.

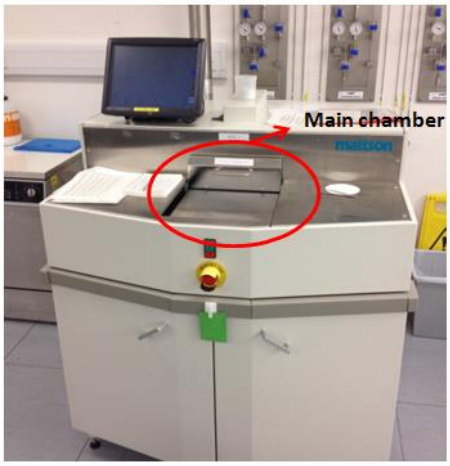

Fig. 3.15: Our RTA system image.

3.3.5. Dry Etching Techniques

(a) Reactive Ion Etching

Reactive ion etching (RIE) is a chemical etching process to remove solid material on wafers to produce volatile materials. The process includes ionizing the molecules to form chemically reactive plasma in order that it can react with the solid material and subsequently remove it. The real system image and schematic representation of our RIE system are shown in Figure 3.16 and 3.17, respectively. The main chamber, control panel and the endpoint laser are all displayed in the image. The wafer is placed between two parallel electrodes, and the chamber is pumped to a low pressure normally under 5 mTorr. Once the pressure is reached, the desired gases are introduced into the chamber. If an electric field is applied between two electrodes, the gases will be ionized and release electrons. These electrons will ionize more atoms by collisions and hence the plasma is formed. Taking the SF_6 gas as an example, when ionized, it will create the plasma containing electrons, mainly positive ions (SF_5^+) and negative ions (F^-). The negative ions (F^-) are accelerated to the wafer and react with the wafer surface, forming the volatile products. Another thing worthy to mention is, due to the applied voltage between the electrodes, the kinetic energies of the ions are very high when reaching the sample surface. This leads to the strong bombardment between ions and sample, which can greatly enhance the etching rate of the material. The ion bombardment is a physical etching process which strengthens with increasing the power. During the RIE etching, the etching power needs to be high enough to provide sufficiently high ion density to enable the chemical etching, while it has to be low enough to reduce this physical process as it can lead to the severe surface damage of the sample [10].

Fig. 3.16: The RIE system image.

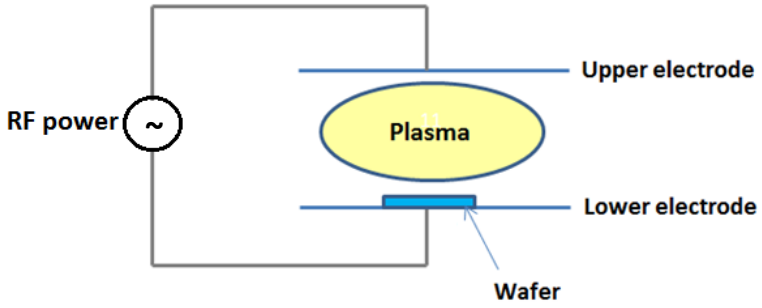

Fig. 3.17: Schematic diagram of the RIE system.

In the process of the nano-rod fabrication which we developed and will be described in detail in chapter 4, SiO_2 acting as a mask is selectively etched by the RIE. CHF_3 and SF_6 are employed as the etchants and their flow rates are set at 30 and 10 sccm, respectively. The etching power of RIE can ranges from 70 W to 150 W which basically influences the SiO_2 etching rate. The etching process is implemented under a pressure of 35 mTorr. In order to monitor the etching process and detect the etching rate, an endpoint laser is employed and directed perpendicular to the sample. It has similar principle to the laser used for the MOCVD growth and can also be explained by the Bragg's Law. During the RIE etching, the thickness of the material is varying constantly, which causes the constructive and destructive interference of the reflected laser. The reflected laser intensity is then recorded by the spectrometer. The wavelength of the endpoint laser is 670 nm, and the refractive index of SiO_2 is ~1.46. Based on the Bragg's Law $2n \cdot d \cdot \sin\theta = k\lambda$ (where n is the refractive index, d is the periodic thickness, θ is the incident angle of laser, k is an integer and λ is the laser wavelength), the thickness of SiO_2 for an oscillation period of laser reflectivity curve can be calculated and is equal to ~230 nm. An example of the endpoint laser reflectivity curve is displayed in Figure 3.18. The top curve is the model for etching of SiO_2 and the bottom one is the real etching curve. The actual SiO_2 deposition thickness is ~200 nm. It can be seen from the bottom curve that after ~550 sec etching, the reflectivity becomes constant meaning the SiO_2 etching has already finished. Normally, a 3-4 min over-etching is applied in order to fully remove the SiO_2 residues. It takes almost an oscillation to finish the etching process which just demonstrates the SiO_2 real thickness ~230 nm. Furthermore, the SiO_2 etching rate can also be estimated and is approximately ~21.8 nm/min. In summary, the endpoint laser enables us to in-situ monitor the etching process and estimate the thickness and etching rate.

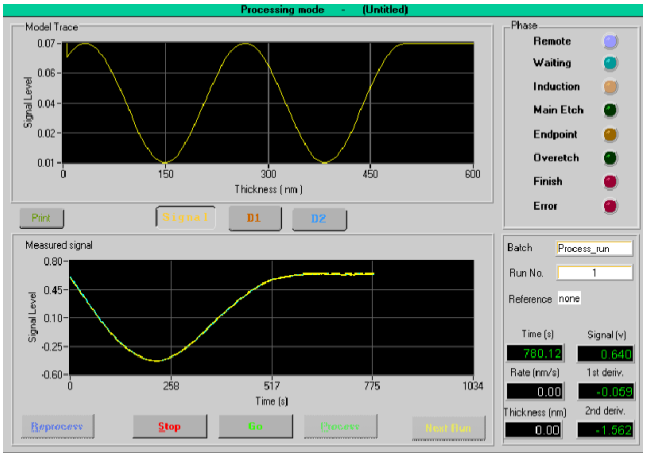

Fig. 3.18: Endpoint laser reflectivity curve.

(b) Inductively Coupled Plasma

Inductively coupled plasma (ICP) is another dry etching technique which employs coils to generate the plasma by inductively coupling. The ICP machine used for our etching process is Oxford plasmalab 100 ICP180 system. The full system image and schematic diagram of our ICP is shown in Figure 3.19 and 3.20, respectively. The sample is firstly placed on a 4-inch Si wafer, which is subsequently loaded into a loadlock chamber. When the loadlock chamber is pumped down to a required pressure (~1.5×10^{-2} Torr), the sample on the Si wafer as a carrier is transferred to the etching chamber to perform the etching process. A similar endpoint laser is applied to monitor the etching process. The wavelength of the laser is 1100nm, which gives a periodic wavelength of ~230 nm for GaN.

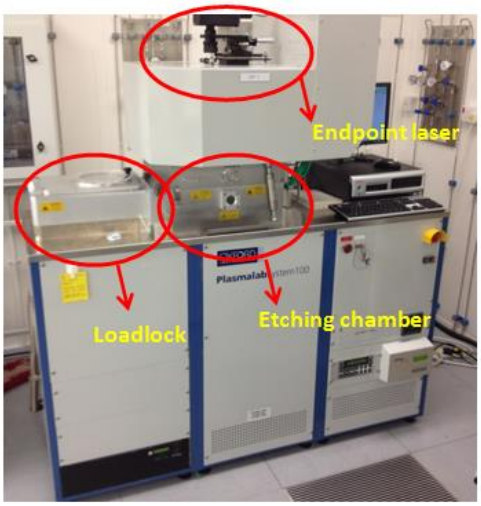

Fig. 3.19: Our ICP system image.

As schematically illustrated in Figure 3.20, a radio frequency (RF) voltage is applied to the coil wrapped around the etching chamber, which induces the magnetic field. The gas mixture in the chamber can be ionized and hence plasma can be created. An extra RF source is applied to the lower electrode to accelerate the ion to the substrate to enhance the ion bombardment process. Therefore, the plasma density and the plasma energy can be controlled independently in the ICP system. Normally, the power applied to the coil (ICP power) has to be high enough to create a high density of plasma. At the same time the power applied to the electrode (sample etching power) needs to be low enough to minimize the damage of the sample surface by ion bombardment. Therefore, compared with RIE etching, ICP etching can achieve a faster etching rate because of the higher ion density and a reduced surface damage due to the lower ion energy [11]. For etching of GaN, the ICP power is kept at 450 W and the etching power is approximately 100W. Cl_2 and Ar are served as the etching gases for GaN, with standard flow rates at 15 and 4 sccm, respectively. Cl_2 can chemically react with GaN to form the volatile gallium chloride whereas Ar can etch GaN physically through ion bombardment. The resultant etching rate of GaN is ~150 nm/min.

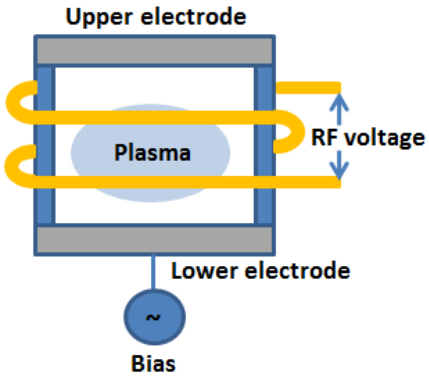

Fig. 3.20: Schematic diagram of the ICP system.

3.3.6. The UV Exposure System - Photolithography

Photolithography is a standard approach which allows us to transfer a desired pattern from a photo mask onto a wafer by means of light exposure. This process involves using a certain type of light-sensitive material named photoresist, which is spin-coated on the wafer followed by exposing the sample through the photo mask with the UV light. Subsequently, the wafer is put into a developer solution. Depending on the type of photoresist (positive or negative), either the exposed area or unexposed area is dissolved. In this way, the pattern from the mask is transferred to the wafer. An image of our UV exposure system is shown in Figure 3.21. As

the photoresist is generally reactive to the light in the UV light, the photolithography has to be implemented in the cleanroom with yellow light only (570 – 590nm).

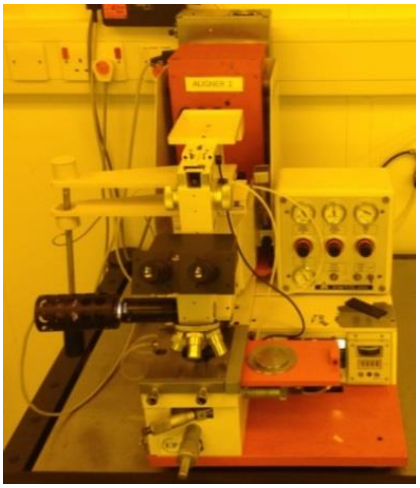

Fig. 3.21: The image of UV exposure system.

A schematic illustration of a standard photolithography process is given in Figure 3.22. Light exposure of the photoresist is performed through a photomask and development is implemented afterwards. Normally, there are two options of the subsequent fabrication when the mask pattern is formed on the sample. The first one is the dry etching process (RIE, ICP etc) where the photoresist serves as the mask. This aims to create some patterned shapes on certain substrates. The other option is to deposit some other materials on top, followed by the lift off process leaving the deposited material only in the 'originally photoresist free area'. This process is normally used for electrodes formation [11].

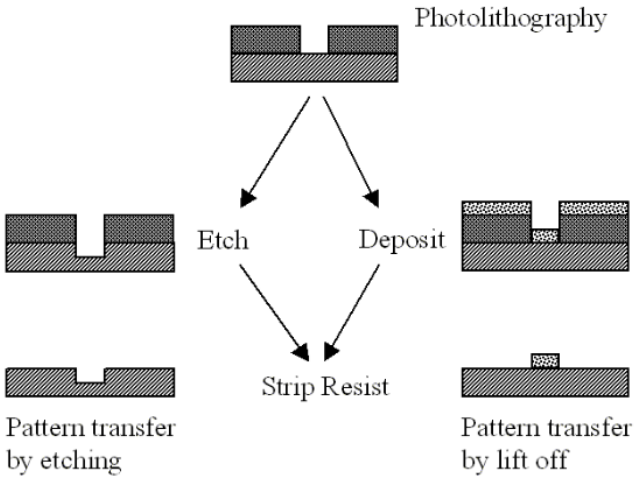

Fig. 3.22: Standard lithography process followed by drying etching or deposition and lift-off [12].

References

1. A. C. Jones, M. L. Hitchman, ‘Chemical Vapour Deposition : Precursors, Processess and Applications’, RSC publishing (2009).
2. C. Martina, M. Dauelsberga,, H. Protzmanna, A. R. Boydb, E. J. Thrushb, M. Heukena, R. A. Talalaevc, E. V. Yakovlevd and A. V. Kondratyev, J. Cryst. Growth **303**, 318 (2007).
3. http://www.slideshare.net/category/feature?category=leadership-management
4. http://www.doitpoms.ac.uk/tlplib/xray-diffraction/bragg.php
5. http://serc.carleton.edu/research_education/geochemsheets/techniques/SEM.html
6. http://www.nanoscience.gatech.edu/zlwang/research/afm.html
7. http://www.microscopemaster.com/transmission-electron-microscope.html
8. K. Okada, Sci. Technol. Adv. Mater. **8**, 624 (2007).
9. D. M. Mattox, ‘Handbook of Physical Vapour Deposition Processing’, William Andrew (2010).
10. D. M. Manos, D. L. Flamm, ‘Plasma Etching, an introduction’, American press (1989).
11. W. E. Soderstrom, ‘Handbook of Photo-lithography’, New York Photo-Lithographers' Association (2011)
12. https://www.memsnet.org/mems/processes/lithography.html

Chapter 4

GaN Nano-rod and Micro-rod Templates Fabrication

4.1. Introduction

With development and optimization of the non-polar and semi-polar GaN growth on sapphire substrates, pits-free samples with smooth surface have been obtained. However, there is still a long way to go to achieve high performance III-nitride emitters based on non-polar/semi-polar GaN, since the material quality remains far from satisfactory due to existing defects in GaN such as dislocations and stacking faults. Therefore, it is necessary to further improve the crystal quality of non-polar/semi-polar GaN grown on the sapphire substrate. One of the most promising approaches to achieve that is to perform the overgrowth on patterned GaN templates. As introduced in Chapter 2, various ELOG techniques based on UV photolithography have been developed, which can significantly reduce the extended defects of overgrown GaN [1-7]. However, the main drawbacks of these approaches are poor uniformity in terms of crystal quality and that the GaN overgrown layer has to be ~10-20 μm thick in order to achieve the surface coalescence. In addition, a poor uniformity in crystal quality of overgrown GaN in the window and wing region also makes these approaches less attractive.

Recently, we developed two simple but cost-effective ELOG approaches, both of which allow us to achieve a quick surface coalescence of samples by the overgrowth of only 1-4 μm. One is using self-organized nano-masks to form a nano-rod template. Compared with conventional ELOG approaches, this self-organized nano-mask methodology has several advantages such as low cost, simple fabrication procedure and good uniformity in crystal quality, making the approach very competitive for commercial mass production. The semi-polar/non-polar GaN overgrown on the nano-rod templates have achieved good results [8, 9], which are presented in chapter 5. Another one is to transfer a micro-rod pattern based on UV mask photolithography. The crystal quality of overgrown GaN on the micro-rod templates is among the best reports using conventional lithography method, which are

discussed in chapter 6. In this chapter, the detailed fabrication techniques and optimization processes are presented for the two kinds of templates. The fundamental equipment involved in the fabrication are introduced in Chapter 3.

4.2. Self-organized Nano-rod Templates

4.2.1. Fabrication Methodology of Self-organized Nano-rods

The GaN templates used for nano-rod fabrication are grown on r-plane or m-plane sapphire substrates by metal organic chemical vapour deposition (MOCVD) using our high temperature AlN buffer technology. A high temperature AlN buffer layer (~100 nm) was first grown at 1180 ℃, followed by the GaN growth with the growth temperature, pressure and V/III ratio at 1100 ℃, 75 Torr and 1600, respectively. The GaN thickness is ~1.3um.

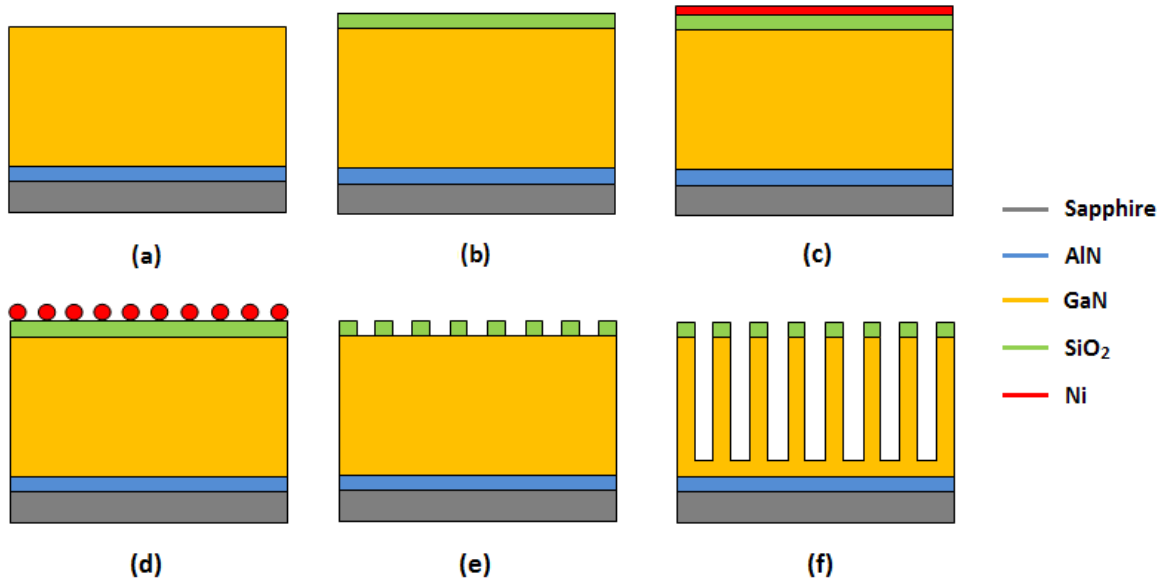

Fig. 4.1: Schematic illustration of nano-rod fabrication procedure: (a) Sample preparation; (b) SiO_2 deposition with PECVD; (c) Ni film deposition; (d) self-assembled Ni islands; (e) SiO_2 etching with RIE; and (f) fabrication GaN nano-rods with ICP.

Figure 4.1 (a)-(f) illustrate the detailed fabrication procedure of our 2-inch GaN template. Firstly, a 200 nm SiO_2 film is deposited on the sample by means of plasma-enhanced chemical vapor deposition (PECVD), where SiH_4, N_2O and N_2 are employed as the reacting gases. The deposition rate of SiO_2 is ~40nm/min. Next, a thin layer of Ni film is deposited on the top of the SiO_2 layer with either thermal evaporator or sputtering deposition system under

high vacuum conditions. The typical pressure for Ni deposition is around 2×10^{-6} Torr. Subsequently, the sample is then annealed using rapid thermal annealing (RTA) at 850˚C in the nitrogen gas ambient for 1 min so that the Ni film is self-assembled to form Ni nano-islands on the top of SiO_2 surface. These Ni nano-islands act as the first nano-masks for etching the SiO_2 film into SiO_2 nano-rod arrays using reactive ion etching (RIE). Finally, SiO_2 nano-rod arrays serving as the second mask, inductively coupled plasma (ICP) is employed to etch the GaN film into GaN nano-rods. The residue Ni mask can be removed by aqua regia. It is worth mentioning that the residue SiO_2 nano-masks are still remained on the top of the GaN nano-rods during the overgrowth. They are crucial to prevent the dislocations penetrating on the overgrowth GaN, and the details will be discussed in Chapter 5.

4.2.2. Formation of Ni Nano-masks

The formation of Ni nano-islands is ascribed to its surface energy and stress induced between the Ni film and the SiO_2 layer underneath. The as deposited Ni film is a continuous film. During the temperature ramp-up process, driven by surface tension, the Ni film on the surface starts to form semispherical islands to lower the total energies [10, 11]. Provided that the film thickness is on the scale of nanometers, it will be self-assembled to form the nano-sized Ni nano-islands.

(a) Nickel Thickness

The average size of the Ni nano-islands is mostly dependent on the initial Ni film thickness. Generally the thicker is the Ni film, the larger the Ni islands are. Figure 5.2 presents the plan-view SEM images of self-organized Ni islands with different Ni deposition thicknesses annealed at 850^{o}C for 1min. A thick Ni film results in Ni islands with larger dimension and lower density while a thin film leads to smaller and denser islands. Thinner Ni film yields more uniform islands than thicker Ni film, i.e. narrower islands size-distribution. Moreover, with increasing the film thickness, self-organized islands become more irregular in shape. A large number of irregular-shaped islands can be observed in Figure 4.2 (c) and (d). It appears that big and irregularly-shaped islands are actually composed of several unseparated smaller islands.

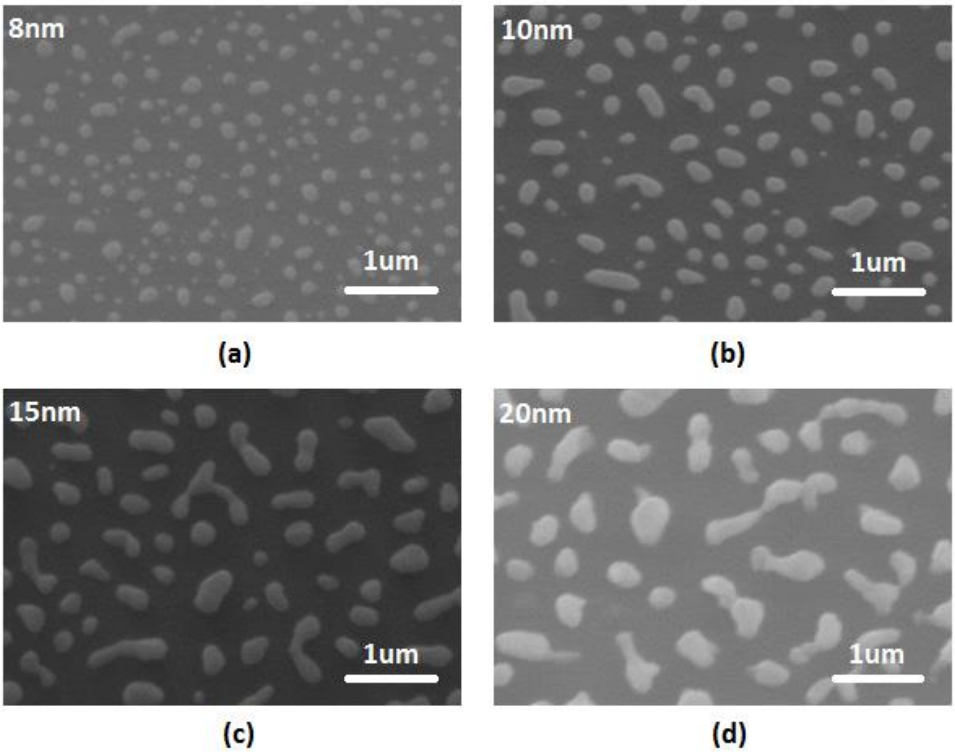

Fig. 4.2: Self-organized Ni islands annealed at 850°C for 1min, with different thicknesses: (a) 8 nm; (b) 10 nm; (c) 15 nm and (d) 20 nm.

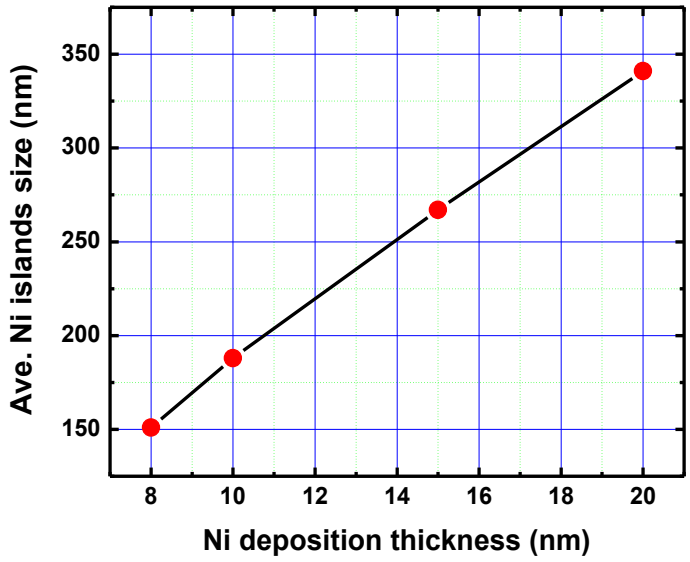

Fig. 4.3: The average size of the Ni islands as a function of the Ni film thickness.

The Image J software is applied in order to calculate the average size of the Ni islands. Figure 4.3 presents the average Ni island size as a function of the Ni deposition thickness. It can be

seen that the average size of Ni islands has a linear relationship with the Ni film thickness. The trend line is calculated as y=15.7x+28.2, indicating that increasing the initial Ni film by 1 nm contributes to the increment of 15.7 nm in the average Ni island size.

(b) Insertion of an Au Layer

The irregular shape and large size distribution for self-organized Ni islands leads to the non-uniformity issue of the GaN nano-rod structure and have a negative impact on the overgrown GaN film crystal quality. Therefore, it is necessary to make improvements in achieving higher quality self-organized nano-masks in terms of shape and uniformity. In theory, if one assumes that SiO_2 surface is perfectly flat and smooth, the surface tension force of Ni islands in each direction will be the same. Hence, the self-organized Ni cluster is supposed to be spherical in shape and similar in size. However, as the SiO_2 surface is not perfectly flat and smooth, the stress that the Ni islands suffer from will anisotropic, resulting in irregular shapes. This becomes more prominent when the Ni film is thicker. Therefore, improving the surface flatness of the SiO_2 is extremely important for formation of uniform Ni islands. Recently, our group has developed an idea based on the 'metal bilayer' method, where an ultra-thin metal interlayer with much lower melting point is deposited on the SiO_2 surface prior to the deposition of the Ni layer. The principle is straightforward: during the temperature ramp up process, the metal interlayer sandwiched between Ni and SiO_2 surface can easily melt and turn to liquid state and distribute uniformly across the sample, which can cancel out the non-uniformity in the surface energy of SiO_2 and help to enhance the Ni migration. Thus, Ni islands with better uniformity can be obtained. The good candidates for the metal interlayer could be gold (Au) or silver (Ag) as their melting points are much lower than Ni. Meanwhile, metals with higher melting points are also investigated in order to make a comparison. In this study, Au and titanium (Ti) with melting points at 1064^oC and 1668^oC (the melting point of Ni is 1455^oC) are chosen as the metal interlayer because of their chemical stability. In order to find the optimum deposition thickness, 1nm, 3nm and 5nm gold film are deposited on the SiO_2 surface prior to 8 nm Ni deposition, which is followed by RTA process. On the other hand, 1nm Ti/ 8nm Ni is deposited on the identical SiO_2 film. The annealing temperatures for all samples above are 850^oC. The surface morphology of Au/Ni is illustrated in Figure 4.4 (a) – (c). It is clear that 1nm Au interlayer leads to the best island uniformity, and with the increase of the Au thickness, the size distribution of the Ni islands

becomes larger. It is noted that many small islands with diameters less than 20 nm can be seen in Figure 4.4 (a). These small islands most likely caused by the gold film can be easily removed by CHF_3/SF_6 plasma during the RIE etching. Figure 4.4 (d) presents the surface morphology of 1 nm Ti/8nm Ni. In a remarkable contrast, the Ni islands are irregular in shape and not uniform in the size. This supports the theory stated above as the melting point of Ti is so high that it can hardly melt and improve the underlying surface flatness.

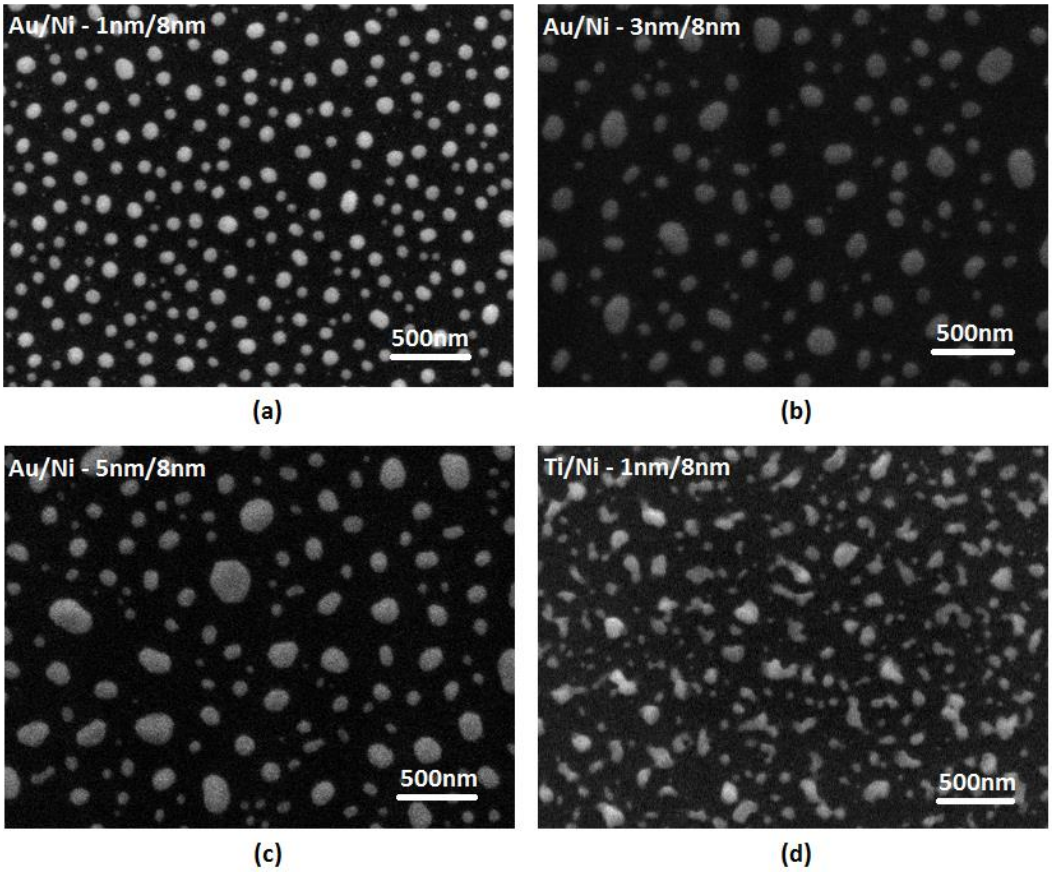

Fig. 4.4: Self-organized Ni islands with (a) - (c) gold interlayer with different gold thicknesses, and (d) Ti interlayer.

Since the ~1 nm Au interlayer has demonstrated the great enhancement of Ni island shape and uniformity compared to the conventional single Ni layer approach, it is further investigated in order to achieve the optimum annealing conditions. The Au/Ni bilayer at 1nm/8nm is annealed by RTA at 700^{o}C, 750^{o}C, 800^{o}C, 850^{o}C, 900^{o}C, and 950^{o}C, respectively for 1 min. The SEM images are shown in Figure 4.5. It can be clearly seen that when the Au/Ni film are annealed at 700^{o}C, the self-organized Ni islands formed are irregular in shape. When the annealing temperature is increased from 750^{o}C - 900^{o}C as shown in Figure 4.5 (b) – (e), the Ni clusters demonstrate tremendous improvement in terms of shape

and uniformity. When the temperature is further raised to 950^{o}C, most of the Ni islands suffer from the 'island tail' issue as can be observed in Figure 4.5 (f), seeming that Ni tends to escape from their original islands and diffuses along random orientations. Henceforth, the annealing temperature has to be sufficiently high to enhance the Ni migration and hence island formation while simultaneously avoiding the 'island tail' issue. The optimum annealing temperature to achieve high quality Ni islands is ~900^{o}C.

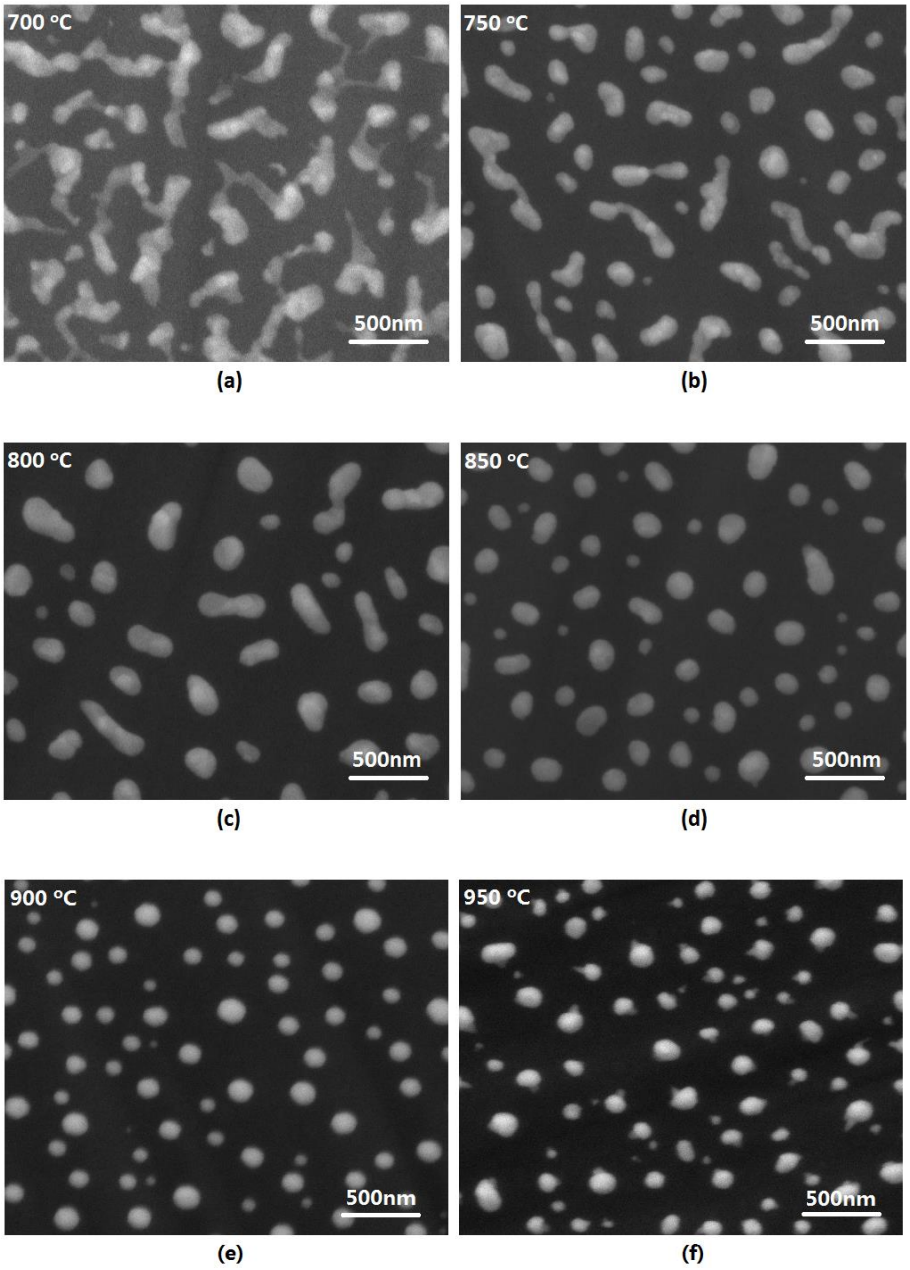

Fig. 4.5: SEM images of Au/Ni layer annealed at different temperatures of (a) 700 ^{o}C to (f) 950 ^{o}C.

In order to achieve a better understanding of the relationship between the Ni islands size and the Ni film deposition thickness, Ni films at different thicknesses are deposited on SiO_2 layers. It is noted that the annealing conditions are all kept the same at 850^{o}C for 1min and the Au interlayer remains at 1nm. The average size of each set of Ni islands is calculated and analyzed by the ImageJ software, and the results are analyzed and are presented in Figure 4.6. It is obvious that with the increase of the Ni film deposition thickness, the average Ni island size becomes larger. This is quite consistent with the results under the Au-free scenario as shown in Figure 4.3, except that the average Ni island sizes tend to saturate with the increase of the Ni film deposition thickness. The data is fitted with a logarithmic trendline by using the software. Further increase of the Ni film thickness can lead to non-uniform islands, and this is probably because the compressive strain induced by thermal expansion difference between two layers are no longer large enough to separate the larger islands into small ones. Our experimental results show that the Ni layer cannot be thicker than ~25 nm in order to obtain uniform islands, at which the average island size is ~350 nm.

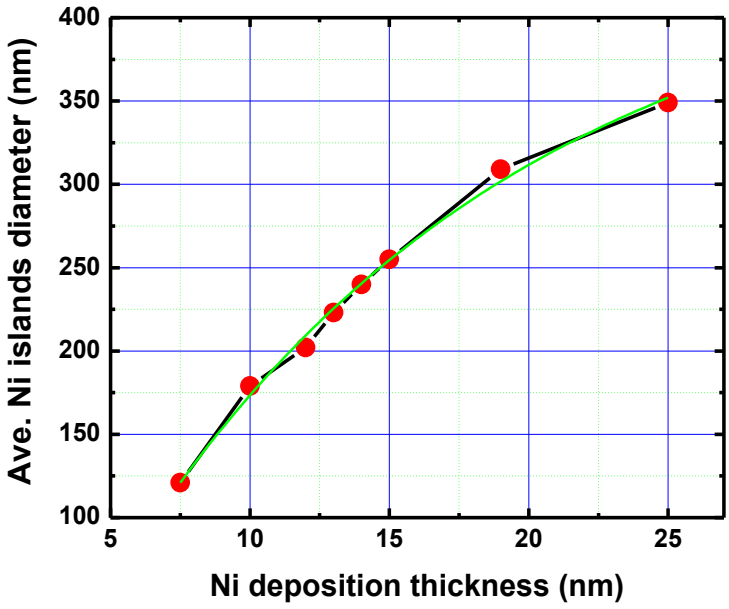

Fig. 4.6: The average size of the Ni islands as a function of Ni film thickness.

Therefore, the introduction of the Au interlayer with appropriate deposition thickness and thermal annealing condition is crucial in improving the Ni island shape and uniformity. It is necessary to obtain the high quality Ni islands because they perform an important role in impacting or even determining the resultant GaN nano-rod morphology.

4.2.3. Optimization of SiO_2 Mask Using Dry Etching

When the self-organized Ni islands are formed, RIE is then employed to etch the SiO_2 layer. The standard recipe for SiO_2 etching is CHF_3/O_2 – 30/5 sccm at 90 W. A SEM image of the SiO_2 nano-mask after RIE etching is shown in Figure 4.7 (a). The sidewalls of SiO_2 nano-rods are a bit concave in the middle part. If only CHF_3 gas is used to perform the etching, then the resultant shape, the average size and gap of SiO_2 mask will be completely different (Figure 4.7 (b)). It is known that the fluorocarbon gases such as CHF_3 can produce some unsaturated compounds in the plasma, resulting in the formation of the polymer [12]. The polymer can be deposited on the sample surface and affect the dry etching process. This explains the 'cone' shape of the SiO_2 nano-masks. The addition of oxygen effectively reduces the polymer formation as it combines with carbon and increases the ratio of fluorine to carbon, which in turn enhances the dry etching process [13]. Therefore, without the 'protection' of the polymer, the SiO_2 masks can be etched easily and form the 'concave cylinder' shape. Therefore, by adding or removing the oxygen plasma during the RIE etching, two types of nano-rods can be created, i.e. either nano-rods with smaller size and larger gap, or nano-rods with larger size and smaller gap.

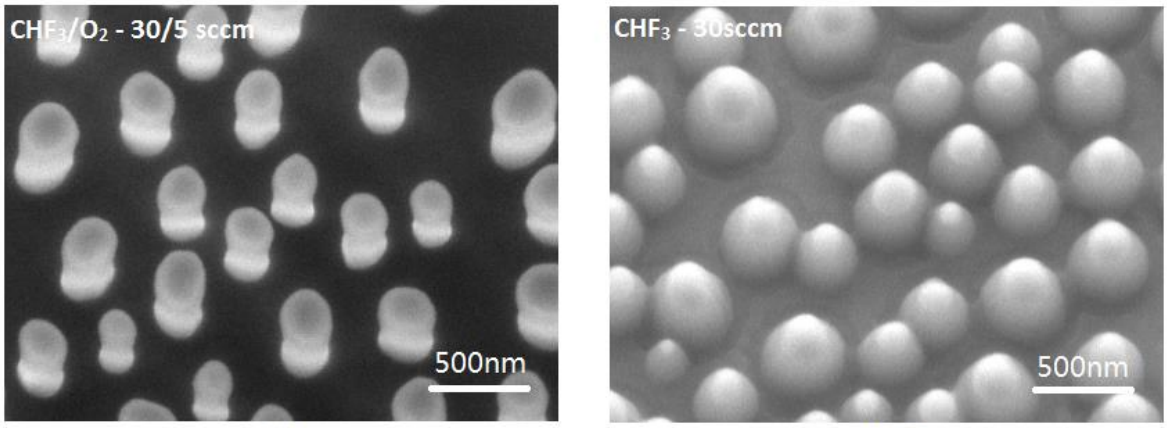

Fig. 4.7: SiO_2 nano-rods etched by RIE using (a) CHF_3=30 sccm and O_2=5 sccm and (b) CHF_3=10 sccm.

Another way to control the size and gap of the GaN nano-rods is to alter the SiO_2 deposition thickness. Figure 4.8 illustrates the schematic diagram of the SiO_2 nano-mask. Assuming the SiO_2 is etched by CHF_3 only, it can be observed that the sample with a thinner SiO_2 layer gives rise to smaller nano-rod and larger gaps whereas the one with a thicker SiO_2 layer

results in larger GaN nano-rod dimension and smaller gaps. This method enables us to perform the systematic study of the overgrowth, where the influence of the nano-rod size and gap on the GaN crystal quality can be investigated, which will be discussed in the next chapter.

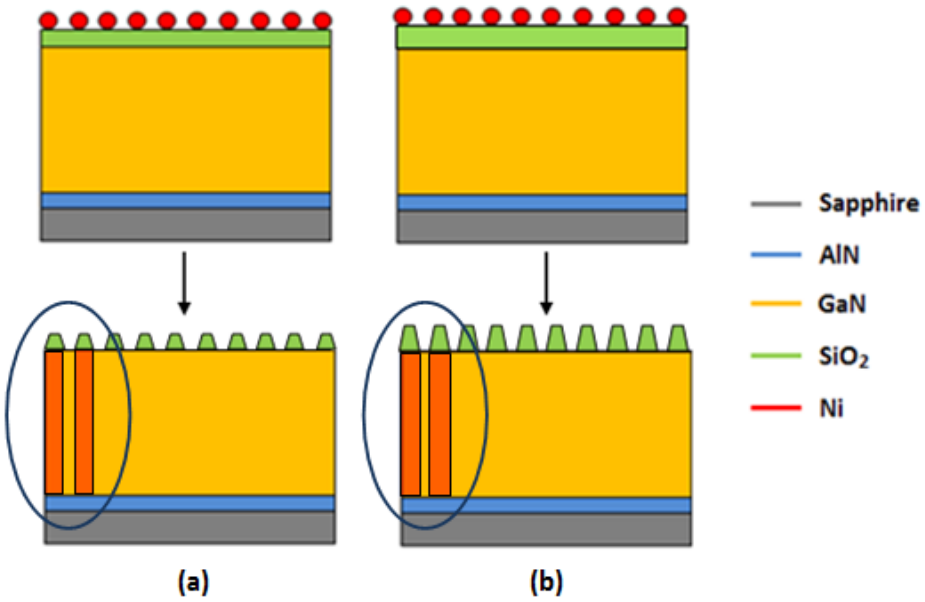

Fig. 4.8: Samples with different initial SiO_2 thickness, (a) thinner SiO_2 (b) thicker SiO_2.

4.2.4. Formation of GaN Nano-rods Using Dry Etching

When the SiO_2 nano-masks are formed, the GaN is then etched by ICP so that the GaN nano-rod structure can be formed. A mixture of chlorine (Cl_2) and argon (Ar) serve as the etchants. The Cl_2 and Ar plasma chemically etches and physically bombards the GaN layer, respectively. The standard flow rates of Cl_2/Ar is 15/4 sccm and the forward/coil power is 100/450w, respectively, both of which determine the GaN etching rate. Increasing or decreasing the power lead to different nano-rod shapes. Figure 4.9 presents the SEM images of samples etched by ICP with 75 W, 100 W, and 150 W, respectively. The etching time for all the samples remains at 8 min. The sample etched at 75 W results in very inclined GaN nano-rod morphology, while increasing the etching power to 150 W leads to concave nano-rods. It is expected that both nano-rod shapes are not desirable. At 75 W, the SiO_2 layer cannot cover the GaN nano-rods very well so that there is a higher chance for threading dislocation to penetrate into the overlying structures; at 150 W, the increased etching due to

Ar bombardment leads to more severe surface damage. Consequently, the ICP power has to be sufficiently high in order to create the straight sidewall and sufficiently low to release the surface damage. At 100 W, the nano-rods are quite straight as shown in Figure 4.9 (b) and the GaN etching rate is ~200 nm/min.

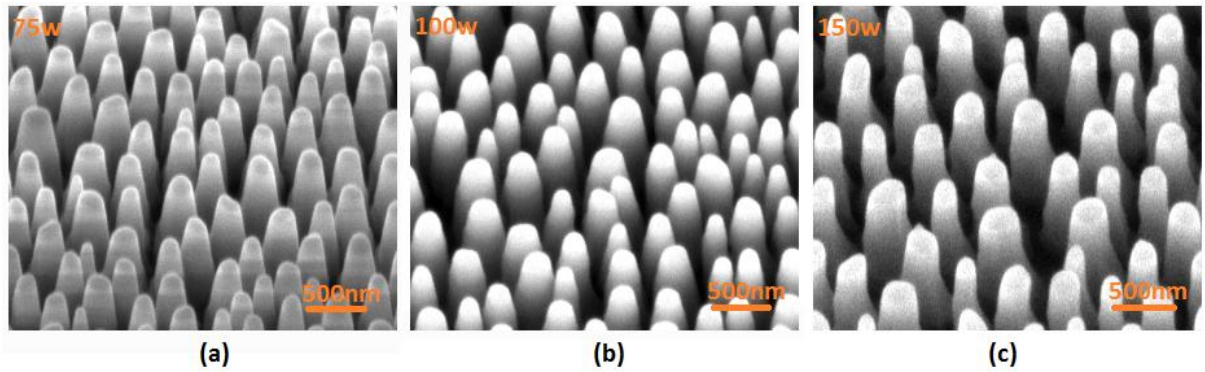

Fig. 4.9: SEM images of GaN nano-rod samples etched at (a) 75W, (b) 100W and (c) 150W by ICP.

It is worth noting that the SiO_2 masks can also be etched by ICP with the etch rate around 30 nm/min at 100 W. This results from the bombardment of the Ar plasma and the SiO_2 etching rate is dependent on the etching power. Therefore, the initial SiO_2 layer has to be sufficiently thick in order to protect the underlying GaN nano-rods from being etched during the ICP etching. Normally the etching depth of the GaN is around 1.5 μm, and the initial SiO_2 film thickness is 350 nm. After the ICP etching, there is still approximately 100-150 nm thick SiO_2 left. This is fundamentally different from other research groups which removed the SiO_2 residue on top of GaN after ICP etching [14]. It is speculated that the SiO_2 residue plays a significant role in reducing threading dislocations in GaN, which is actually confirmed by our TEM images. Details will be discussed specifically in Chapter 5.

4.2.5. Summary

Our standard nano-rod fabrication procedure has been presented, and the fabrication technique has been optimized. With optimization of the self-organized Ni nano-masks, a massive improvement in the nano-rod quality with respect to the shape and uniformity can be achieved. Figure 4.10 (a) illustrates the GaN nano-rod structure fabricated using our current standard procedure. In a remarkable contrast, Figure 4.10 (b) displays the nano-rod morphology fabricated using usual self-organized nano-mask approach. A huge improvement

in the nano-rod shape and uniformity can be seen. Furthermore, the nano-rod size, gap, shape and length can be well controlled by modifying the RIE and ICP etching parameters. Figure 4.11 shows SEM images of GaN nano-rod structures with an average diameter of 250 nm, 400 nm, 650 nm and 900 nm, respectively. It is expected that the GaN nano-rod parameters have a significant impact on the subsequent GaN overgrowth and can thus greatly influence the sample crystal quality and surface morphology.

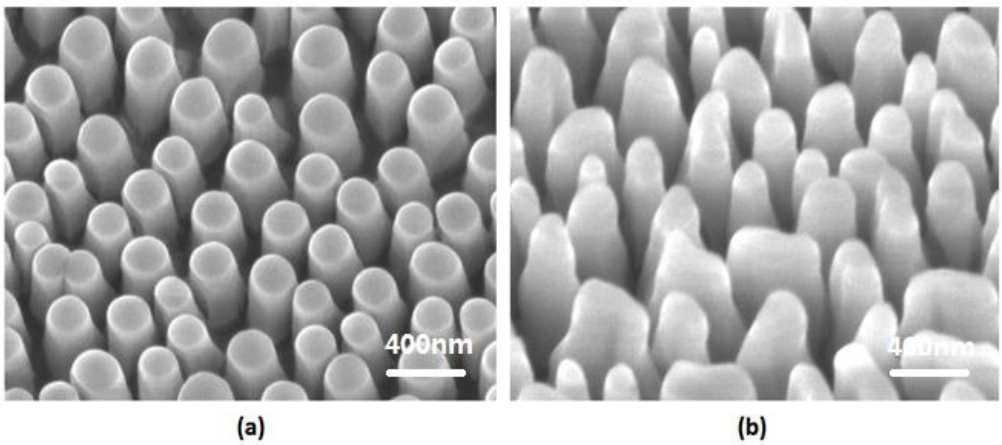

Fig. 4.10 (a) optimized GaN nano-rod structure and (b) GaN nano-rod structure fabricated with usual fabrication procedure.

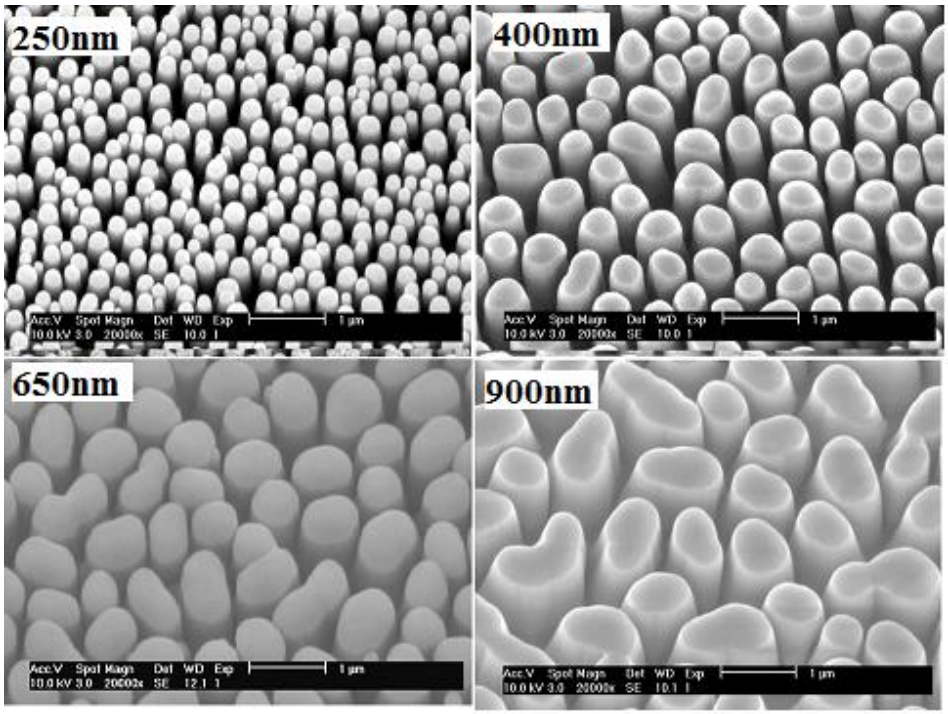

Fig. 4.11 SEM images of GaN nano-rod structures with an average diameter of 250 nm, 400 nm, 650 nm and 900 nm, respectively.

4.3. Micro-rod Templates Based on UV Lithography

In last section, an effective overgrowth approach based on the nano-rod template has been presented. The average size of the nano-rod can be achieved from 200 to 1 μm. However, there are several limitations and disadvantages for this technique. Firstly, it is difficult to apply this approach based on larger-sized (4 or 6 inch) sapphire substrate due to the cracking issue during the process of rapid thermal annealing, which makes it less attractive for mass production. Secondly, the largest attainable GaN nano-rod by using this approach is about 1 μm. However, increasing the average rod size is supposed to effectively reduce the coalescence boundary, hence improving the crystal quality. Therefore, in order to further increase the pattern size, other technology needs to be used. On the other hand, as has been discussed in previous chapter 2, conventional ELOG approaches have a major drawback compared with the self-organized nano-mask approach: an atomically flat GaN layer cannot be achieved until the overgrowth layer is ~10-20 μm thick due to large gaps of the pattern at a scale of tens of micron.

In this section, we present a modified template pattern methodology using UV photolithography with our newly designed mask. The size of the micro-rod is on a micron scale and the diameter and gap of micro-rods can be accurately controlled. The smooth surface of GaN can be achieved within the overgrowth of ~4-5 μm, much thinner than conventional ELOG approaches. And the semi-polar GaN demonstrates a further improvement along m-direction compared with the self-organized nano-mask methodology.

4.3.1. Fabrication Procedure

The (11-22) semi-polar as-grown GaN templates for the ELOG process are grown on m-plane sapphire by MOCVD using our high temperature AlN buffer technology. A high temperature AlN buffer layer (~100 nm) was grown at 1180 ℃ for the nucleation of GaN growth, followed by the GaN growth with the growth temperature, pressure and V/III ratio at 1100 ℃, 75 Torr and 1600, respectively.

The fabrication procedure is simple but effective with high reproducibility. The schematic diagram of the fabrication procedure is illustrated in Figure 4.12 (a) – (f). Firstly, the PECVD is employed to deposit the SiO_2 film with a thickness ~500 nm. This is followed by the spin

coating of the positive photoresist at (BPRS100) on the SiO_2 film, where the spinning speed is set at 4000 rpm. The resultant photoresist thickness is ~1 µm. Subsequently, the sample is placed under the patterned area of the mask and exposed to the UV light for 4.0 sec. Next, the sample is dipped into MF26A developer for 1 min so that the region which is exposed to light is dissolved in the solution. In this way, the mask pattern can be transferred from the mask onto the sample. The O_2 plasma asher is then employed to clean UV-exposed area. After that, the 50 nm Ni is deposited on the sample and the lift-off procedure is then performed. Thus, the Ni clusters are formed on top of the SiO_2 layer. These clusters act as the mask for SiO_2 etching, where a combination of CHF_3 and O_2 plasma serve as the etchants. Finally, the ICP is employed to etch the GaN/AlN layer, with Cl_2 and Ar as the etchants, down to the sapphire such that a micro-rod structure is formed.

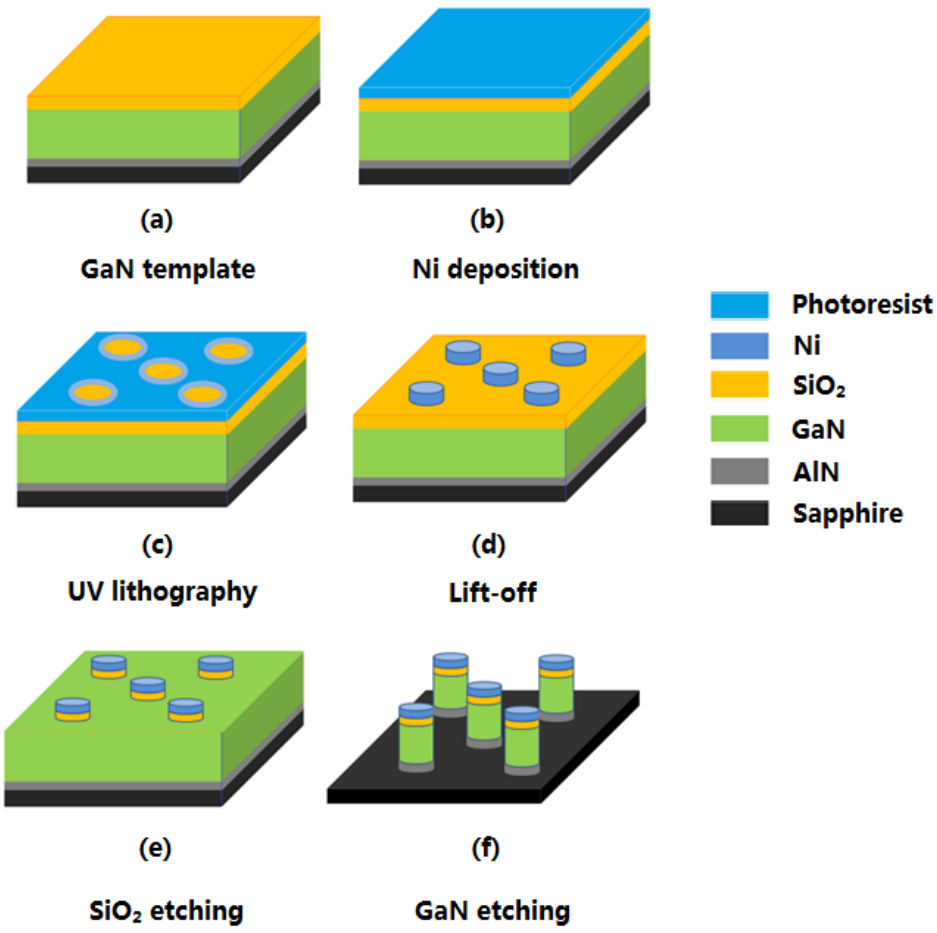

Fig. 4.12: Schematic diagram of the fabrication procedure of the micro-rod template.

4.3.2. Control of Diameter and Gap of Micro-rods

The pattern of the masks designed for the GaN overgrowth is an array of identical circles with a period of 3 μm. The diameter of the circle and the gaps between two neighbouring circles along horizontal/vertical directions are identical and are equal to 1.5 μm. The schematic diagram of the mask pattern is shown in Figure 4.13. The shaded area of the mask is transparent where the light can penetrate through, and the rest part is covered with chromium and is opaque.

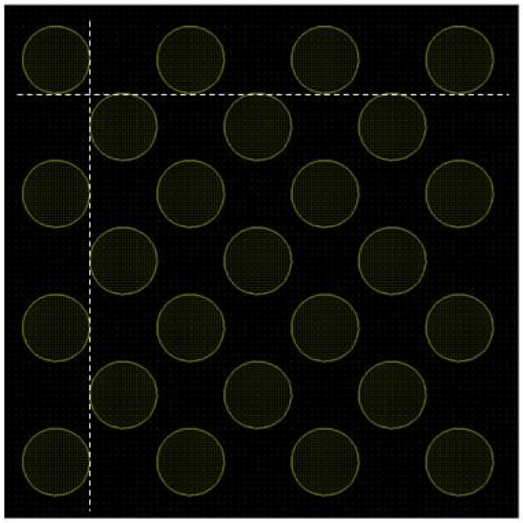

Fig. 4.13: The schematic drawing of the mask pattern.

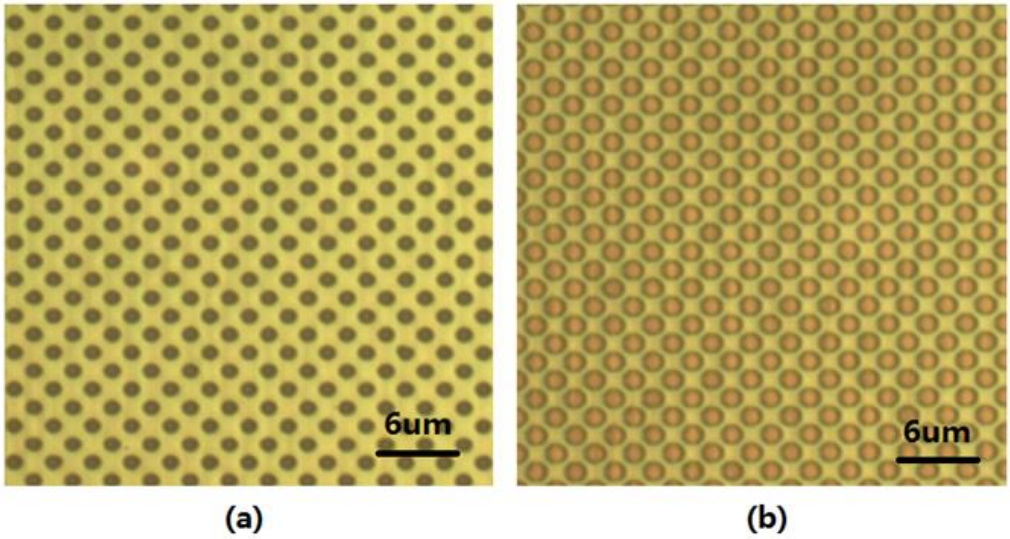

Fig. 4.14: Microscopy images of the sample after UV exposure for 4 sec and MF26A development for (a) 1 min and (b) 1.5 min.

Figure 4.14 (a) presents the microscope image of the sample after 4.0 sec UV exposure and 1 min developing. It can be seen that the resultant pattern shape has an array of circles, with the diameter of the circle close to the size of the gap between two neighbouring circles. Due to the very small size of pattern, the exposure and developing time affect the circle size, that is, longer exposure and developing times lead to larger circles. Figure 4.14 (b) is the microscopy image for the sample after the 1.5 min development. The size of the circular hole increases tremendously and the gap between two neighbouring holes reduces correspondingly, with the pattern period remaining unchanged. Therefore, the size and gap of the micro-rod can be well controlled by using this method.

4.3.3. Uniformity of 2-inch Micro-rod Template

After the pattern is transferred to the photoresist on the sample, a ~50 nm Ni layer is deposited onto it, followed by the lift-off procedure using acetone. Then micro-sized circular Ni clusters can be formed on the SiO_2 surface. Same as that for the self-organized nano-rod fabrication, the function of the Ni micro-mask acts as the first mask for RIE etching of SiO_2.

Figure 4.15 (a) presents the top-view SEM image of the SiO_2 mask of the sample after RIE etching. The gas CHF_3 acts as the etchant and its flow rate is 30 sccm. The etching power and time are 90 W and 20 min, respectively. The average size and gap are both ~1.5 μm. Finally, the ICP is applied to etch the GaN with Cl_2/Ar – 15/4 sccm at 75 W for 9 min through the AlN layer and down to the sapphire substrate. Now, the GaN micro-rods are created. Figure 4.15 (b) illustrates the bird-eye view SEM image of the micro-rod fabricated using the our ELOG approach. Note that the SiO_2 mask still remains on top of the rods prior to the GaN overgrowth. Figure 4.15 (c) is a capture of our 2-inch template. Different areas of the sample including centre part, 1.5 cm from the centre (top, bottom, left and right part) of the sample are all inspected by the SEM. Figure 4.15(d) illustrates SEM images measured across the 2-inch wafer, and it can be seen that the micro-rods are uniformily distributed across the template. It has been confirmed that high uniformity in terms of size, gap and shape across the 2-inch wafer can be achieved by patterning with 1 micron scale based on UV photolithography.

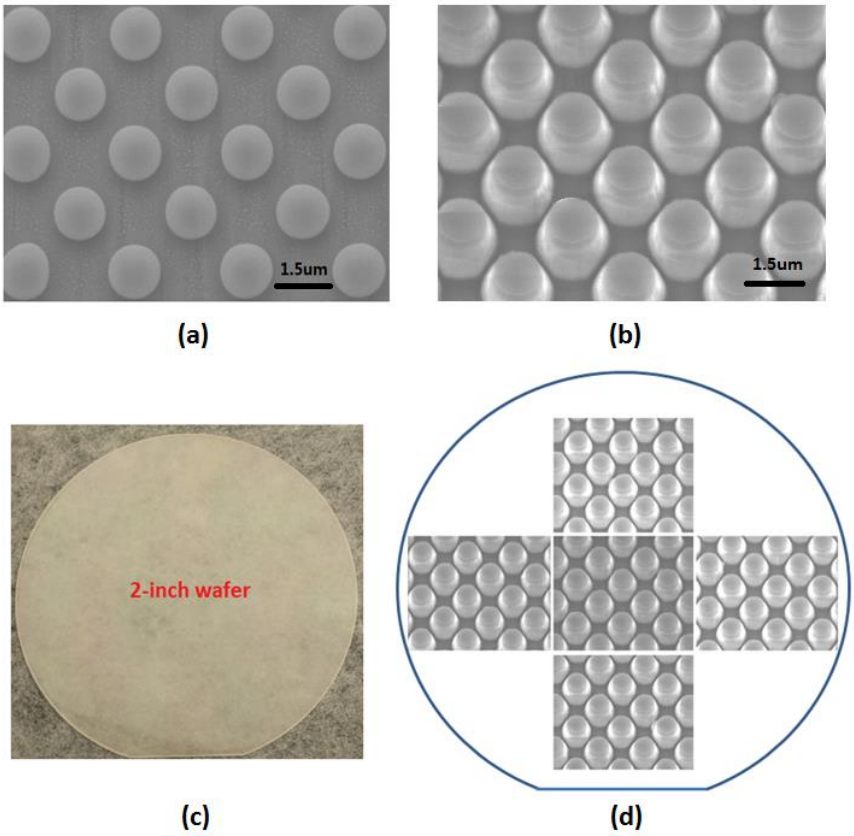

Fig. 4.15: SEM images of (a) The Ni/SiO_2 mask on the GaN surface, (b) micro-rod template for GaN overgrowth, (c) photo of a 2-inch micro-rod template and (d) SEM image of the micro-rod template in different areas demonstrating the good uniformity.

4.3.4. Summary

Semi-polar GaN micro-rod templates for the overgrowth have been achieved based on UV photolithography. The diameter and gap of micro-rods at one micro scale can be accurately controlled by modifying the exposure and developing times while the pattern period remains same, which is very important for optimization of the GaN overgrowth. A very good uinformity has been demonstrated across a 2-inch wafer in terms of size, gap and shape. In the near furture, we are aiming at fabricating the 4-inch and 6-inch template by using this technology in order to meet higher requirements for the mass production. It is expected that the GaN overgrowth using this approach is supposed to lead to better crystal quality of semi-polar GaN compared with nano-rod templates fabricated using the self-organized approach.

References

1. P. Fini, L. Zhao, B. Moran, M. Hansen, H. Marchand, J. P. Ibbetson, S. P. DenBaars, U. K. Mishra, and J. S. Speck, Appl. Phys. Lett. **75**, 1706 (1999).
2. K. Linthicum, T. Gehrke, D. Thomson, E. Carlson, P. Rajagopal, T. Smith, D. Batchelor, and R. Davis, Appl. Phys. Lett. **75**, 196 (1999).
3. Kidoguchi, A. Ishibashi, G. Sugahara, and Y. Ban, Appl. Phys. Lett. **76**, 3768 (2000).
4. K. Hiramatsu, K. Nishiyama, M. Onishi, H. Mizutani, M. Narukawa, A. Motogaito, H. Miyake, Y. Iyechika, and T. Maeda, J. Cryst. Growth **221**, 316 (2000).
5. B. A. Haskell, F. Wu, M. D. Craven, S. Matsuda, P. T. Fini, T. Fujii, K. Fujito, S. P. DenBaars, J. S. Speck, and S. Nakamura, Appl. Phys. Lett. **83**, 644 (2003).
6. B. Imer, F. Wu, S. P. DenBaars, and J. S. Speck, Appl. Phys. Lett. **88**, 061908 (2006).
7. D. Iida, M. Iwaya, S. Kamiyama, H. Amano, and I. Akasaki, J. Cryst. Growth **311**, 2887 (2009).
8. K. Xing, Y. Gong, X. Yu, J. Bai, and T. Wang, Jpn. J. Appl. Phys. **52,** 08JC03 (2013).
9. Y. Gong, K. Xing, J. Bai, T. Wang, Physica. Status Solidi-(c) **9**, 564 (2012).
10. C. Bower, O. Zhou, W. Zhu, D. J. Werder, and S. Jin, Appl. Phys. Lett. **77**, 2767 (2000).
11. J. A. Floro, S. J. Hearne, J. A. Hunter, P. Kotula, E. Chason, S. C. Seel, and C. V. Thompson, J. Appl. Phys. **89**, 4886 (2001).
12. Raghuram, U. (1993). Reactive Ion Etching of Si/SiO_2 by $CHF_3/CH4/O_2$ Gas Mixture. San Jose State University.
13. H. K. Lee, K. S. Chung, and J. S. Yu, J. Kor. Phys. Soc. **54**, 1816 (2009).
14. S. C. Ling, C. L. Chao, J. R. Chen, P. C. Liu, T. S. Ko, T. C. Lu, H. C. Kuo, S. C. Wang, S. J. Cheng, and J. D. Tsay, J. Cryst. Growth **312**, 1316 (2010).

Chapter 5

Semi-polar and Non-polar GaN Overgrowth on Self-organized Nano-rod Templates

5.1. Introduction

During the past two decades, remarkable progress on high efficiency group III nitride-based optical emitters has been achieved, which leads to the commercialization of the visible light emitting diodes (LEDs) and laser diodes (LDs) [1, 2]. However, it is known that the wurtzite III-nitride based optical emitters grown along [0001] direction suffer from reduced optical performance because of the spontaneous and piezoelectric polarization induced electric field [3, 4]. The most effective approach to mitigate or eliminate this negative effect is to grow the GaN along semi-polar or non-polar orientations [5-9]. It has been confirmed that there is no quantum confined Stark effect (QCSE) in non-polar GaN based quantum wells (QWs) while the QCSE in (11-22) semi-polar GaN has been reduced by ~80% compared with the c-plane QWs [9]. Additionally, it has been found that the (11-22) semi-polar QW has a higher indium incorporation rate, demonstrating it a suitable green emitter [10]. Despite the advantages stated above, in the semi-polar or non-polar GaN growth, both the crystal quality and optical efficiency are poorer than those of standard c-plane GaN. Up to date, the high performance semi-polar/non-polar III-nitrides based emitters can be obtained by using the free-standing semi-polar/non-polar GaN substrates [11, 12]. However, the free-standing GaN substrates are very expensive, which makes it much less competitive for the mass production. Conventional GaN ELOG approaches are applied to improve the semi-polar and non-polar GaN crystal quality, which is based on patterning of the as-grown GaN template into micron-scale stripe features with UV lithography, followed by the selective overgrowth on the templates [13-17].

The major drawback of this type of methodology is that the due to the wavelength limit of the UV lithography, both the GaN stripes and the gaps cannot be further reduced down to sub-micron scale. This leads to a non-uniform issue of the overgrown GaN film in terms of the crystal quality, which makes it extremely hard to perform the device fabrication on such surface. In addition, a ~10-20 μm thick overgrown layer has to be grown in order to achieve

an atomically smooth GaN surface. Due to these reasons, the overgrowth of GaN needs to be performed on a nanometre-scaled pattern. Recently, a simple ELOG approach based on the self-organized nano-masks has been performed for the non-polar GaN overgrowth, and the overgrown layer thickness has been reduced significantly to achieve a smooth surface [18, 19]. Our group uses GaN nano-rod structure as a template, which is fabricated from the 2-inch as-grown GaN template by using the self-organized Ni nano-mask approach. The overgrowth of GaN is performed on such semi-polar or non-polar GaN nano-rod template by means of metal organic chemical vapour deposition (MOCVD).

The optimization of the GaN nano-rod template fabrication has been intensively discussed in Chapter 4 and the nano-rods with good uniformity have been achieved. In this chapter, we concentrate on semi-polar and non-polar GaN with a low dislocation density and good surface morphology, achieved by an overgrowth on nano-rod templates. Systematic studies on a variety of growth and fabrication parameters are performed, and optimum growth conditions and nano-rod features are obtained. Structural, optical and electrical characterisations are carried out. Furthermore, InGaN/GaN multiple quantum well (MQW) structures are grown on top of the overgrown GaN films in order to examine their good optical properties.

5.2. Semi-polar GaN Overgrown on Nano-rod Templates

5.2.1. Growth Methodology

The overgrowth of GaN is performed by MOCVD on a 2-inch semi-polar GaN nano-rod template, which is fabricated using the self-organized approach on the as-grown semi-polar GaN template. The schematic diagram of the semi-polar template is illustrated in Figure 5.1 (a), where different GaN orientations are highlighted. The c and a axis are orientated approximately 31.6^{o} and 58.4^{o} from the surface, respectively [20]. Figure 5.1 (b) shows the 3D representation of the semi-polar GaN growth, where the growth rate in the c direction (Ga face) is faster than any other growth orientations [17, 20].

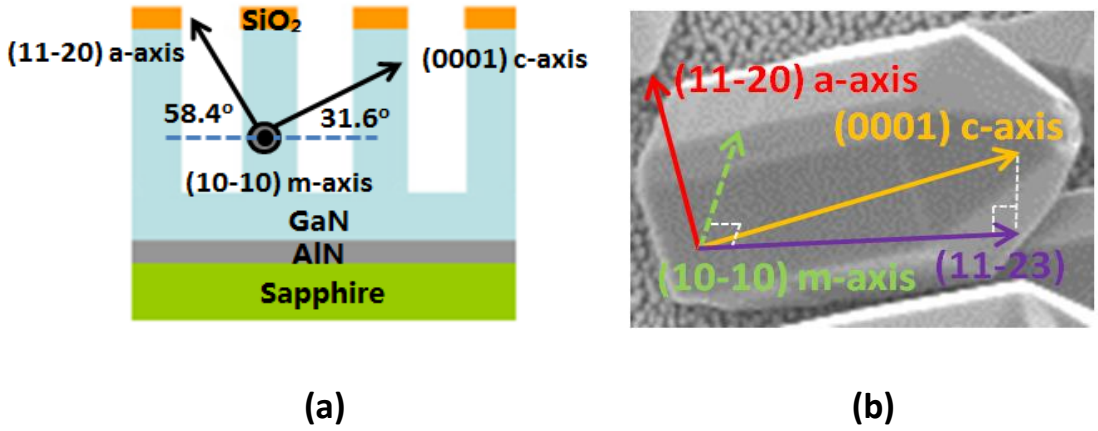

Fig. 5.1: (a) Schematic diagram of semi-polar nano-rods with orientations highlighted and (b) GaN overgrown on the semi-polar GaN nano-rods.

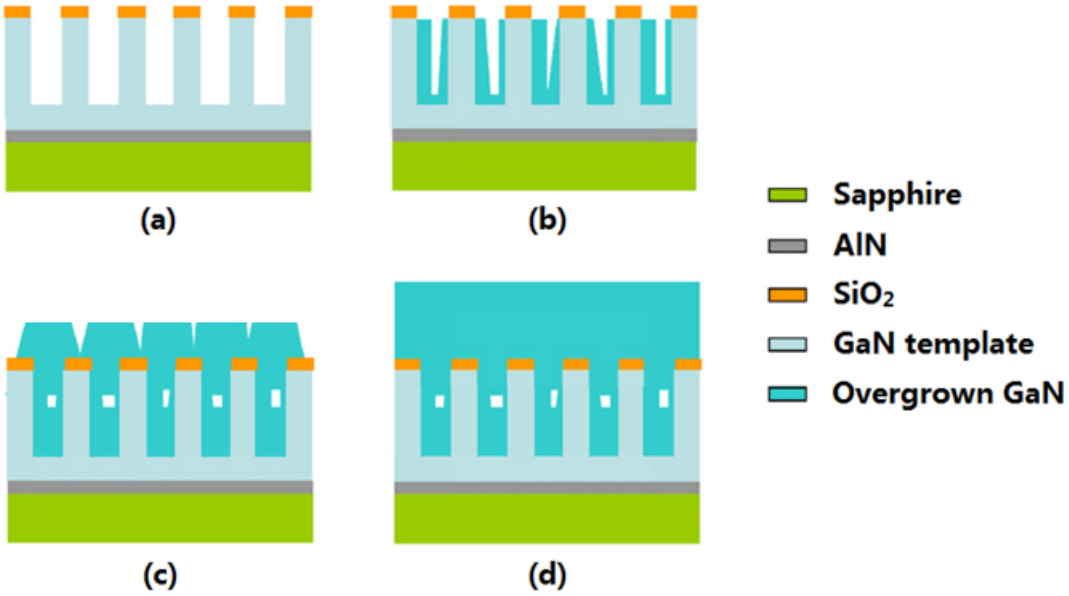

Fig. 5.2: Schematic diagram of growth stages for the GaN overgrowth on a nano-rod template.

Figure 5.2 is the schematic representation of different stages of the GaN overgrowth performed on a nano-rod template. The first stage (Figure 5.2 (b)) involves the GaN growth initiating from both exposed sidewall and bottom part of the nano-rods, where a high ratio of lateral growth rate to vertical growth rate is favoured. When the GaN growing faces on the neighbouring sidewalls meet each other, they start to grow in the vertical direction and reach the top of the SiO_2 nano-masks. After that, the GaN extends laterally and eventually coalesces forming a flat overgrown surface. It is worth highlighting that the SiO_2 is remained

on top of the nano-rod during the MOCVD overgrowth, in order to stop the threading dislocation from penetrating into the overgrown region.

In the study of semi-polar GaN overgrowth, a few growth variables are investigated and optimized in order to achieve the best crystal quality and surface morphology of the overgrown GaN. The standard growth conditions are 1100 ℃, 1800 sccm and 40 sccm for temperature, NH_3 and TMG flow rates, respectively.

(a) Sample Cleaning and Surface Treatment Prior to Overgrowth

Before the sample is put back into MOCVD to perform the overgrowth, the proper surface treatment needs to be performed in order to clean the nano-rod sidewall. Due to the physical bombardment during the ICP etching, different types of particles such as Ni and SiO_2 can be re-deposited on the GaN nano-rod sidewalls and affect the overgrowth. Figure 6.3 presents the cross-sectional SEM image of the overgrown GaN on a nano-rod template without cleaning. Clear boundaries of the GaN nano-rods can be observed, indicating that the GaN growth hardly initiated from the sidewall, which forces the growth from the bottom part of the nano-rod structure. This results in the poor crystal quality and surface morphology of the sample. Based on the discussion above, different wet chemical etchings are applied to clean the GaN nano-rod sidewalls. Following is our standard cleaning procedure of the non-polar and semi-polar nano-rod template prior to the overgrowth:

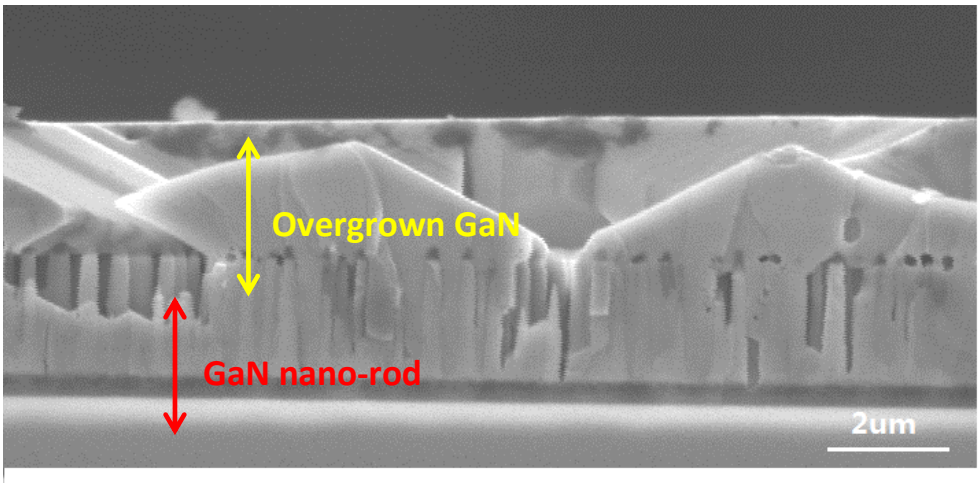

Fig. 5.3: Cross-sectional SEM image of the GaN overgrowth performed on a nano-rod structure without cleaning.

a) Firstly, the sample is soaked into n-butyl, acetone and isopropyl alcohol (IPA) solvents respectively, each for three minutes at room temperature.

b) Next, the sample is put into the boiled concentrated HNO_3 for ~5min to remove the Ni residues.

c) Finally, the sample is finally soaked in the 0.05% KOH solution for ~1min at room temperature. This step is used to remove the residue SiO_2 stuck on the nano-rod sidewall as KOH can react with GaN so that the SiO_2 is peeled off during the reaction.

(b) Effect of Growth Temperature

The growth temperature is one of the most important growth parameters in the GaN growth. Generally, higher growth temperature gives rise to higher GaN desorption rate and hence the low overall GaN growth rate; whereas lower temperature leads to the reduced surface atomic diffusion of the Ga and N atoms and therefore could result in structural defects. The temperature dependency experiments series are performed and the growth temperature is varying between 1080^{o}C to 1120^{o}C, with other growth and fabrication parameters remain constant. The overgrown GaN layer is ~3μm and the SEM images of the overgrown sample surface morphology grown at different temperatures are illustrated in Figure 5.4 (a) – (c), respectively. At 1080^{o}C, a high density of GaN hillock features can be clearly observed on the surface. With the increase of the growth temperature, the density of the hillock becomes much lower and the size becomes smaller; the hillock feature eventually disappears at 1120^{o}C.

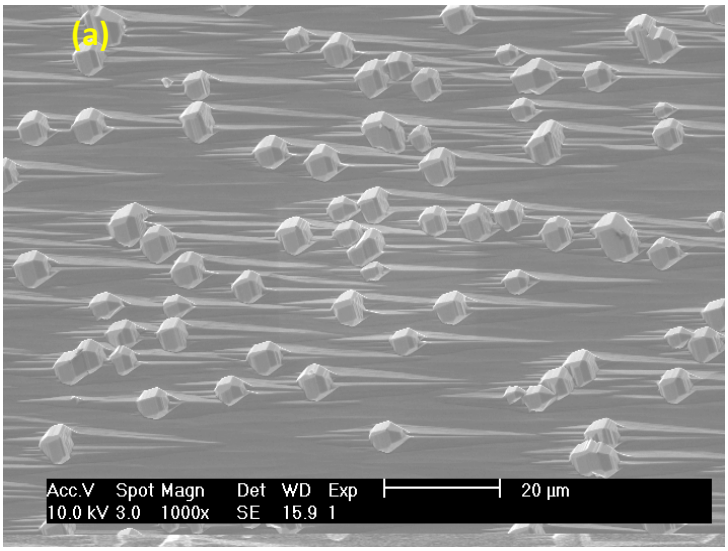

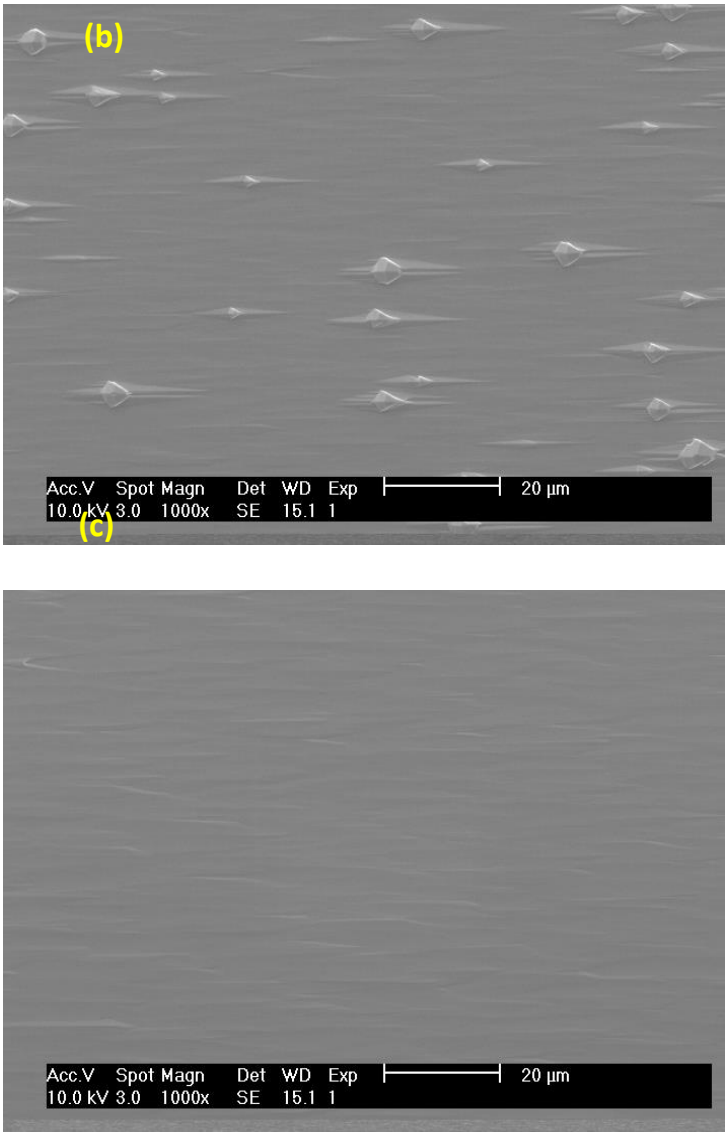

Fig. 5.4: SEM images of surfaces of semi-polar GaN overgrown at (a) 1080^{o}C, (b) 1100^{o}C and (c) 1120^{o}C, respectively.

On the other hand, compared with the sample grown at 1100^{o}C, it can be observed that the sample grown at 1120^{o}C shows stronger stripes. The formation of stripes is due to different growth rate along different orientations. For wurtzite GaN structure, the growth rate along c direction is much higher in comparison to other growth directions, that is, the coalescence along the m direction has not completed when the GaN has achieved the coalescence along the c direction. This leaves some gaps along c direction and hence the stripes are along c direction. Increasing the growth temperature can further enhance the c direction growth rate effectively [21], which explains why the stripe becomes stronger. As a conclusion, the growth

temperature has to be high enough to avoid the hillocks but has to be low enough to mitigate the surface stripes.

The crystal quality of samples is characterized by high resolution X-ray diffraction (XRD). Due to the anisotropic nature of the semi-polar GaN, the XRD rocking curve measurement for our semi-polar overgrown sample is performed along the on axis (11-22) as a function of the azimuth angle. The azimuth angle is defined as 0 when the projection of the incident X-ray beam is parallel to the m-axis of the epilayer. The XRD rocking curve results of the samples above are illustrated in Figure 5.5, in which the full width at half maximum (FWHM) measured at different azimuth angles are displayed. At 1080^{o}C, the sample crystal quality at different azimuth angles does not vary as significantly as the other two samples, which is considered to be due to the existence of the hillocks. It seems that the hillocks can greatly deteriorate the XRD along the [11-23] direction. Besides, hillocks make the device fabrication extremely difficult and thus have to be avoided. Overall, the sample grown at 1120^{o}C turns out to be the best in terms of crystal quality and surface morphology.

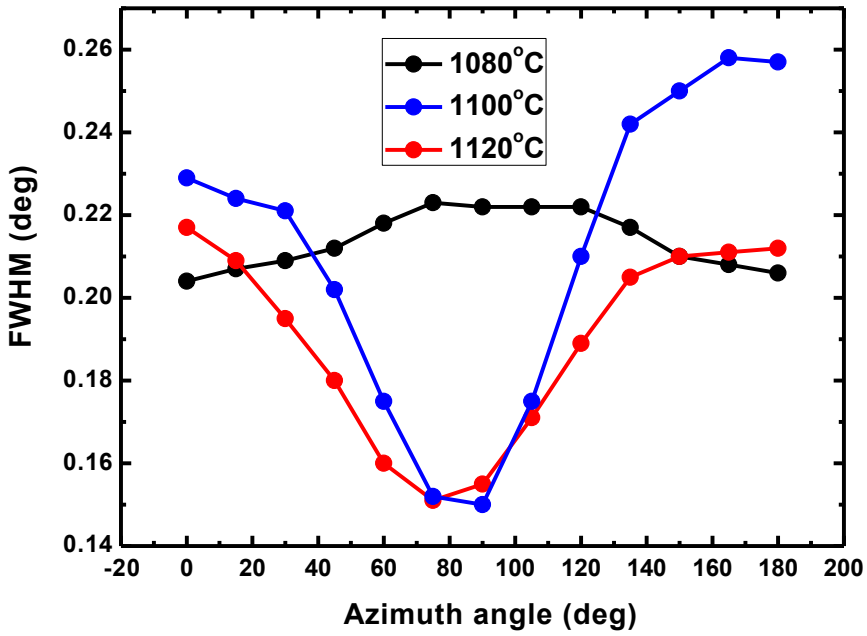

Fig. 5.5: The XRD FWHM of semi-polar GaN grown at different temperatures measured along [10-10] and [11-23].

(c) Effect of Precursor (NH_3 and TMG) Flow Rate

The change of flow rates of the NH_3 and TMG has also found to be effective to the GaN epitaxial overgrowth. The flow rate of the NH_3 is firstly varied between 1800 to 3400 sccm while the TMG flow rate and the other variables remain constant. The growth temperature is set at 1120^{o}C (optimized in the last section). Figure 5.6 shows the SEM images of the overgrown sample surface morphology. At NH_3 = 1800 sccm, the surface has no hillocks but with reasonably strong stripe feature. With the increase of the NH_3 flow rate to 2800 sccm, the stripes become weaker and the surface becomes smoother. A further increase of NH_3 flow rate to 3400 sccm leads to some hillocks on the surface. This is because increasing the V/III ratio (NH_3 flow rate) can decrease the c direction growth rate, and hence the stripes become weaker. However, too high NH_3 flow rate will make the Ga migration more difficult, i.e. shorter diffusion length, leading to the hillock feature.

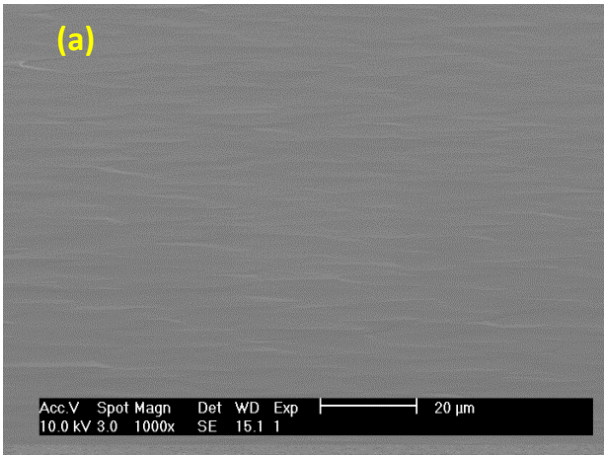

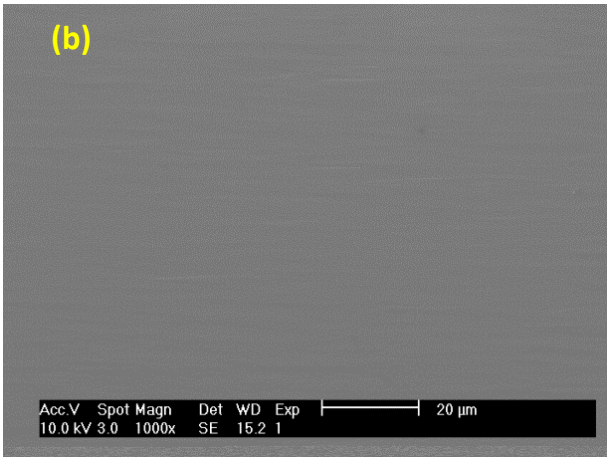

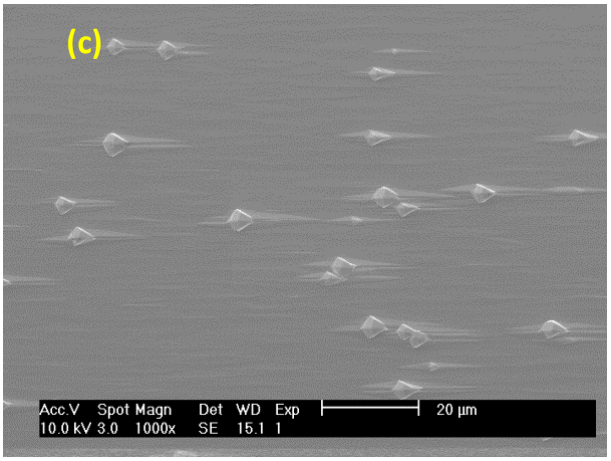

Fig. 5.6: SEM images of surfaces of semi-polar GaN overgrown at (a) 1800 sccm, (b) 2800 sccm and (c) 3400 sccm, respectively.

The crystal quality of these samples grown with different NH_3 flow rates are shown in Figure 5.7. It can be seen that by changing the NH_3 flow rate, the crystal quality of the overgrown GaN does not vary so much.

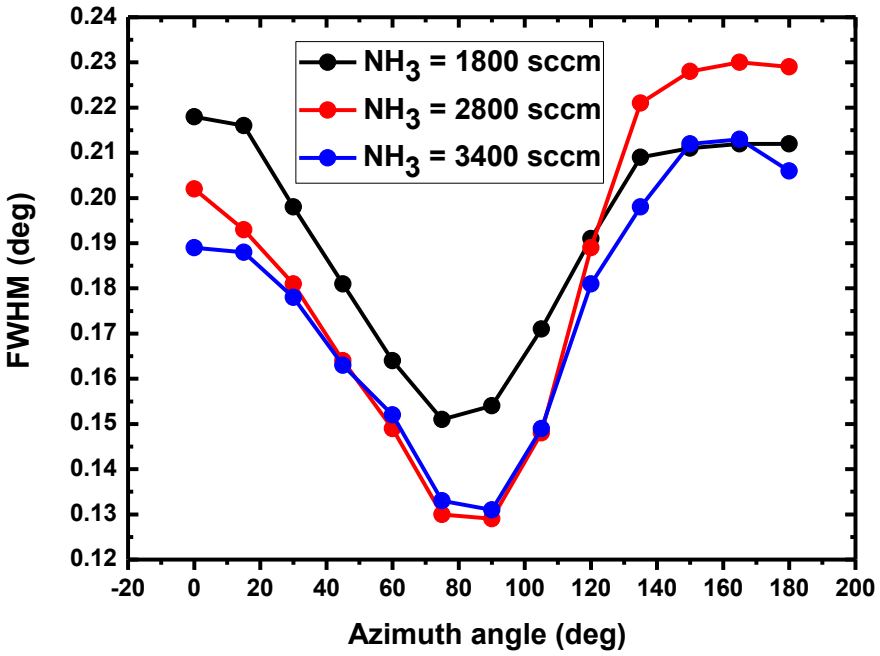

Fig. 5.7: The XRD FWHM of semi-polar GaN grown with different NH_3 flow rates.

The variation of the TMG flow rate yields the similar results. In this experiment series, the TMG flow rate was changed from 30 – 65 sccm while all the other parameters remain constant. It is found that the GaN growth rate is much faster with higher TMG flow rate,

whereas the resultant surface morphology is not good since too high growth rate can cause inhomogeneous coalescence leading to poor surface. In conclusion, the optimum flow rates of the NH_3 and TMG remain at 2800 sccm and 30 – 40 sccm, respectively.

5.2.2. Effect of Templates on the Overgrowth

A few factors about nano-rods are investigated and optimized in order to achieve the best crystal quality and surface morphology of the overgrown GaN.

(a) SiO_2 Remaining on Top of the Nano-rods

The SiO_2 layer, which acts as the mask for the etching of GaN, can either be removed by hydrofluoric acid (HF) or simply remain on top of the GaN nano-rod prior to the overgrowth. These two cases actually lead to completely different growth models. The schematic diagram of the GaN overgrowth with SiO_2 with a thickness of ~200nm on top of nano-rods was illustrated in Figure 5.1, where the growth of GaN initiates from the upper part of the nano-rod sidewall and the average coalescence position is somewhere in the middle of the nano-rods. Figure 5.8 presents the schematic diagram of the nano-rod overgrowth without the SiO_2 cap. The growth of GaN commences from the top and upper sidewall of the nano-rod and the coalescence is achieved at a higher position of nano-rods, which in turn leaves a larger residue voids.

Based on the analysis above, it can be deduced that the SiO_2 theoretically performs an indispensable role in reducing the dislocation density because of two main reasons. First and foremost, the SiO_2 layer can effectively prevent the threading dislocations penetrating from the underlying nano-rod structures to the overgrown GaN; secondly, the SiO_2 layer can force the GaN growth to initiate only from the nano-rod sidewall of the nano-rod such that the lateral growth can effectively bend the threading dislocations in the basal plane and make them annihilate during the coalescence.

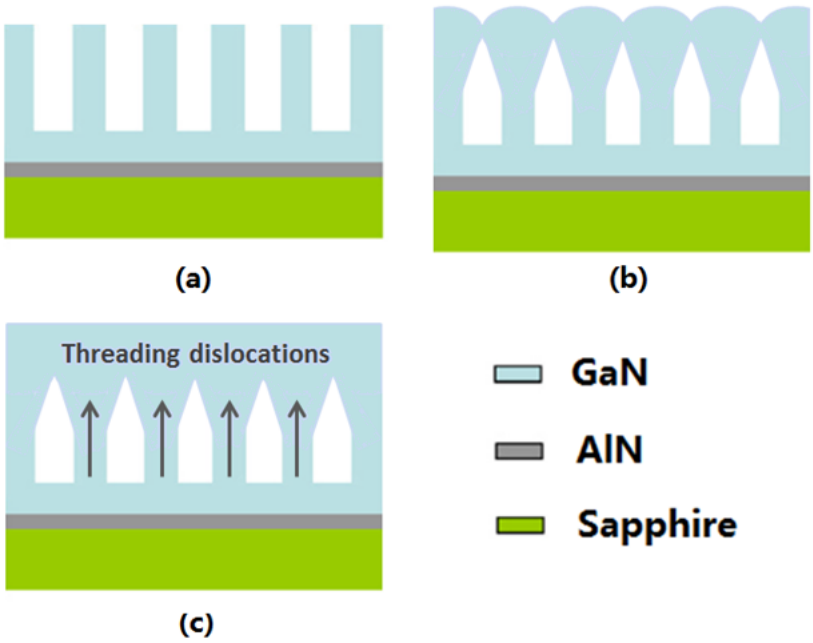

Fig. 5.8: Schematic diagram of the GaN overgrowth on nano-rods without the SiO_2 cap.

(b) Effect of Nano-rod Etching Depth

The etching depths of the semi-polar GaN templates are also modified to do the investigation. Two templates are fabricated using the identical conditions apart from the ICP etching time at 4min and 7min, respectively. The resultant etching depth of the nano-rod is ~1.2μm and ~2μm (etching down to sapphire), respectively. The growth conditions are identical. The XRD results show that the sample crystal quality along c direction has improved from 710 to 600 arc sec. The cross sectional SEM image of the two samples are illustrated in Figure 5.9 (a) and (b). The SiO_2 mask and the residue voids can be seen in both images. The voids are formed when the coalescence of the GaN between the neighbouring nano-rods are achieved, which is due to the fast GaN lateral growth rate. It can be seen that there are very few voids left in Figure 5.9 (a) and their sizes are very small. In a remarkable contrast, the voids formed at the bottom part of nearly each neighbouring nano-rods, and the average sizes of the voids is much larger as shown in Figure 5.9 (b). This is because if the GaN is etched through the mask opening down to the sapphire substrate, the growth of GaN will be forced to initiate from the sidewall as GaN cannot be directly grown from the sapphire substrate. As long as the coalescence is achieved, the residues voids are formed. On the contrary, if the nano-rod etching depth is very shallow, GaN can be grown from both the sidewall and the bottom. In this case, there is a low chance for the voids to be formed. Therefore, there is a higher chance

for the dislocations to extend from the nano-rod gap region right up to the overlying overgrown GaN area, leading to poor crystal quality of the overgrown layer.

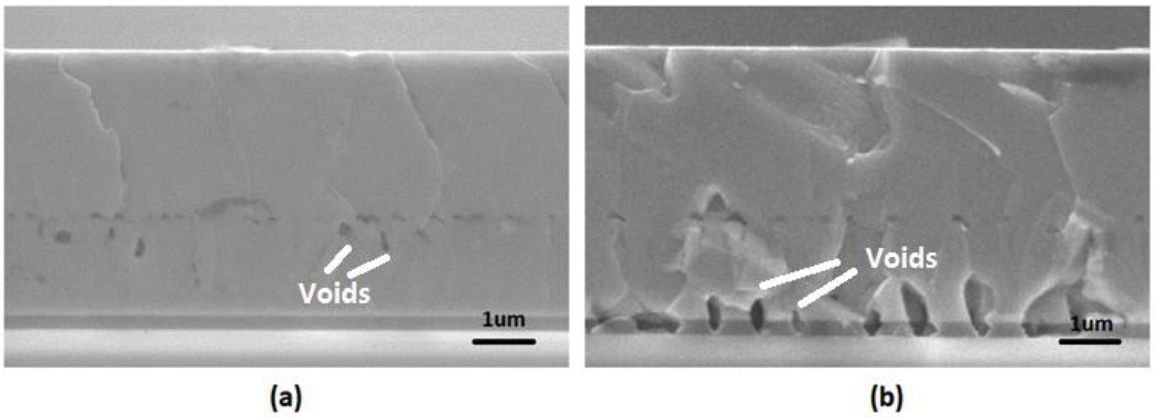

Fig. 5.9: Cross sectional SEM images of semi-polar GaN on nano-rod templates, with ICP etching time at (a) 4 min and (b) 7 min, respectively.

(c) Effect of Nano-rod Size

It is demonstrated that the average nano-rod size is the most predominant parameter that affects the crystal quality of the overgrown GaN. In this experimental series, a number of GaN nano-rod templates with different average nano-rod sizes are prepared for the overgrowth, which is achieved by tuning the Ni deposition thickness (as discussed in Chapter 4). All the rest of the growth parameters remain constant in order to make comparisons. Figure 5.10 presents the XRD FWHM of the samples overgrown on templates with various average nano-rod sizes ranging from ~300 nm to ~1 μm. The FWHMs are measured along both [10-10] **m** direction and the [11-23] **a** direction (azimuth angle at 0^o and 90^o). It can be seen that the crystal quality along both directions show tremendous improvement with increase of the template nano-rod size, where the FWHM reduces from 0.276 ºto 0.151 ºalong [10-10] direction and from 0.142 º to 0.104 º along [11-23] direction, respectively, which clearly demonstrated that template with larger nano-rod size leads to higher crystal quality.

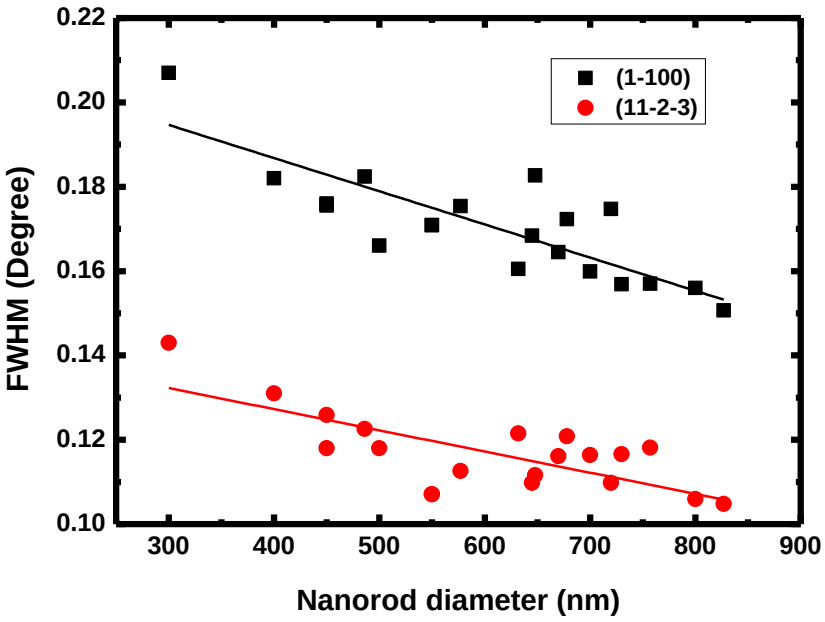

Fig. 5.10: The XRD FWHM of semi-polar GaN overgrown on nano-rod templates with various nano-rod sizes.

It is known that a high density of threading dislocations can be generated during the film coalescence [22], and theoretically reducing the number of the coalescence regions can effectively decrease the threading dislocation density. Therefore, the template with larger average nano-rod size achieves better crystal quality. Moreover, if we observe the diagram more carefully, it can be found that with increase of the average nano-rod thickness, the FWHM along [11-23] direction does not drop further and saturates at ~0.11 º 0.12 º, whereas the FWHM along the [10-10] direction still constantly decreases. It can be deduced that a further increase of the nano-rod size may lead to better crystal quality along [10-10] direction. However, due to the limitation of the self-organized Ni nano-rod fabrication approach, the largest achievable nano-rod size with good uniformity is only ~1 µm.

5.2.3. Structural and Optical Characterization

By optimizing a series of growth and fabrication conditions, the semi-polar overgrown GaN film with superior surface morphology and crystal quality has been achieved. Figure 5.11 is a surface image of the overgrown sample taken by SEM. It is clear that a smooth surface has been achieved within a growth of only 4-5 µm.

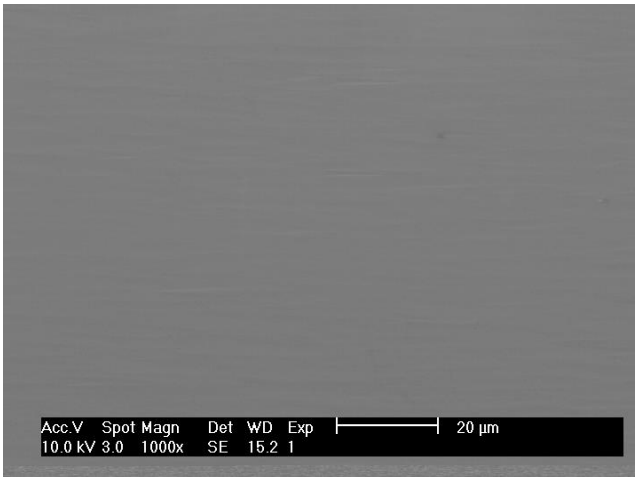

Fig. 5.11: SEM image of surface of overgrown semi-polar GaN.

The crystal quality of samples is characterized by high resolution XRD. The azimuth angle is defined as 0 when the projection of the incident X-ray beam is parallel to the m-axis of the epilayer. In order to make comparison, the same type of XRD measurement is carried out for the standard semi-polar GaN template. Figure 5.12 displays asymmetrical X-ray rocking curve of overgrown and standard non-polar GaN along (11-22) orientation. The FWHM results for both samples are illustrated in Figure 5.13. It is clear that the FWHM has been tremendously reduced from 1350 to 544 arc sec at 0^{o} and 627 to 364 arc sec at 90^{o}, respectively, indicating a much lower dislocation density of the semi-polar overgrown GaN.

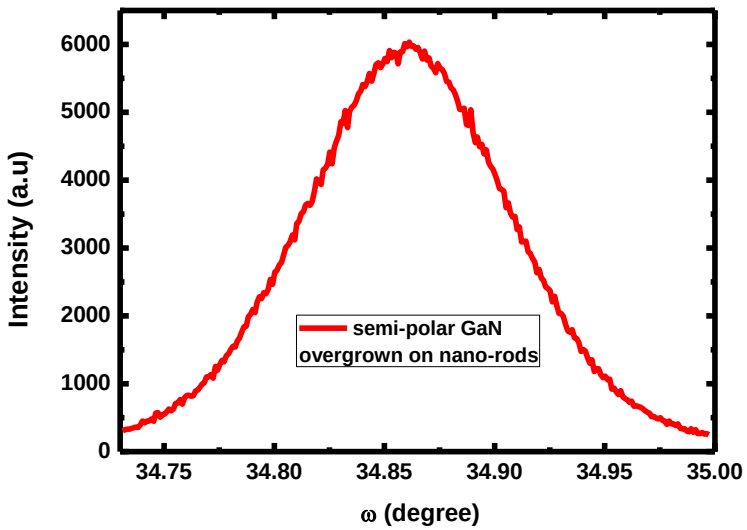

Fig. 5.12: Asymmetrical X-ray rocking curve of overgrown semi-polar GaN along (11-22) orientation.

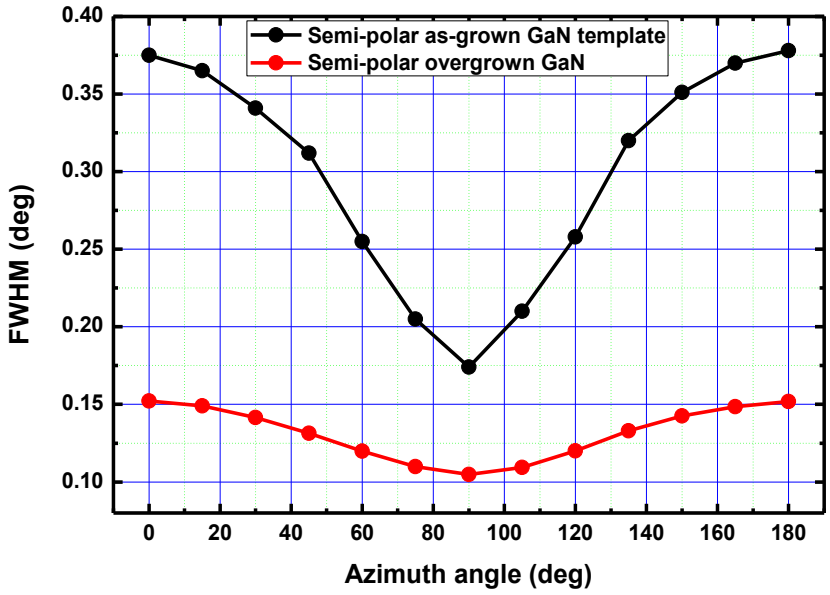

Fig. 5.13: XRD FWHM results for the overgrown semi-polar GaN and the as-grown GaN template as a function of azimuth angle.

Optical property of the overgrown semi-polar GaN was carried out by photoluminescence (PL) measurements using a 325 nm laser diode. As shown in Figure 5.14, the intensity of band edge emission for the overgrown sample is increased compared with standard as-grown semi-polar GaN template, by an enhancing factor of 30. It indicates that the crystal quality of semi-polar GaN is significantly improved due to the overgrowth.

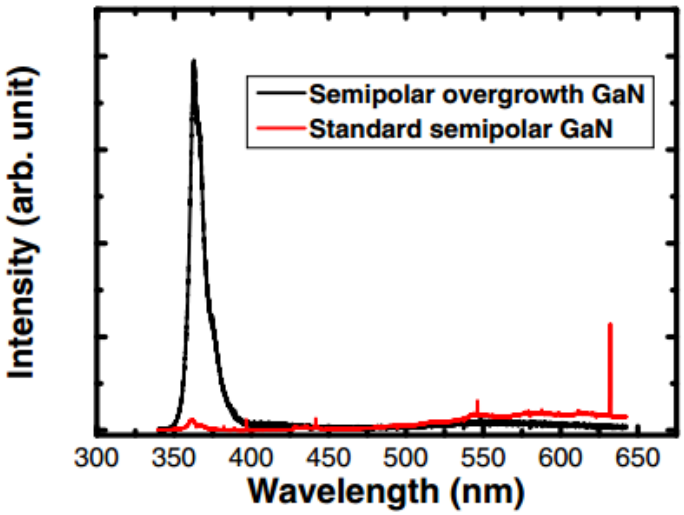

Fig. 5.14: Room temperature PL spectra of the overgrown semi-polar GaN and the as-grown GaN template.

5.2.4. Electrical Property

Electrical properties have been investigated by studying mobility and carrier density. Unlike c-plane GaN, semi-polar GaN exhibit anisotropic nature. Therefore, the dependence of electron mobility on orientation has been measured.

Hall Effect measurements via the Van der Pauw method have performed in order to study the electrical properties. However, the standard Van der Pauw measurements can only allow us to obtain the isotropic in-plane sheet resistance, and thus isotropic carrier mobility. Therefore, the standard Van der Pauw measurements cannot be applied on the measurements of anisotropic semi-polar GaN. In this section, we employed the transmission line model (TLM) method to measure directional dependent sheet resistance, which allows us to obtain electron mobility of semi-polar GaN along different orientations.

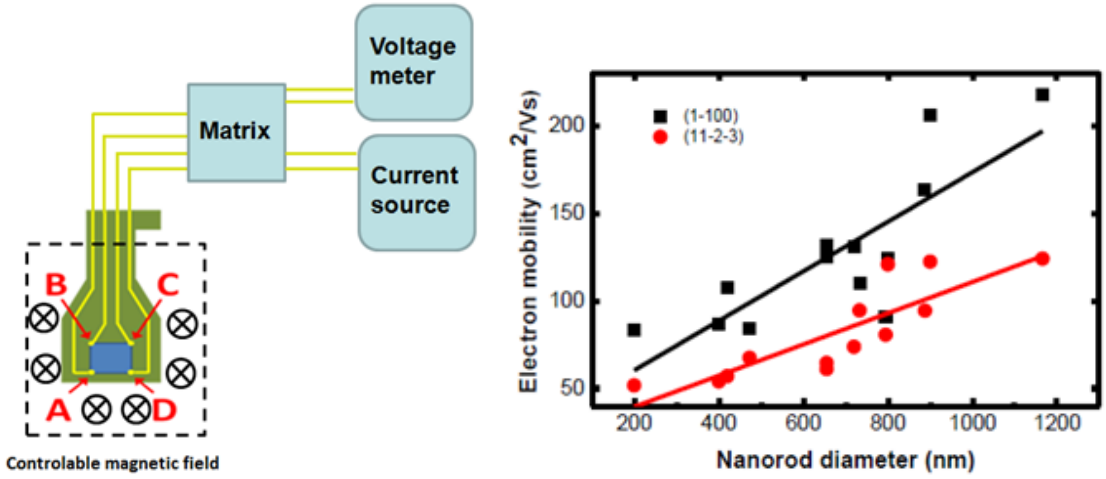

Fig. 5.15: (a) Experimental set-up of Hall measurements; (b) Electron mobility as a function of the nano-rod diameter along different directions.

The free electron sheet density can still be obtained by the standard Hall Effect measurement. The set-up of the experiment is shown in Figure 5.15(a). A sample holder with four contacts is placed in a space with a controllable magnetic field. The four contacts are connected to a matrix box which connects to a voltage meter and a current source. In this study, the applied current is 2 mA and the strength of the magnetic field is 0.56 T.

The directional dependent sheet resistance is measured using the TLM method. TLM patterns along the (1-100) and (11-2-3) directions have been fabricated. Ti/Al/Ti/Au alloy with thickness of 30/100/30/150 nm has been used in order to allows us to achieve good ohmic contacts. By measuring the resistance between each contact, the directional dependent sheet

resistance can be obtained. Equation 1 is used to calculate the directional dependent electron mobility.

$$\mu_{directional} = \frac{1}{q n_s R_{s-directional}}$$

Where $\mu_{directional}$ is directional dependent electron mobility; q is electron charge, n_s is sheet resistance and $R_{s\text{-}direcional}$ is directional sheet resistance.

Figure 5.15(b) shows directional dependent electron mobility along both (1-100) and (11-2-3) directions as a function of nano-rod diameter, performed at room temperature. Furthermore, with increasing nano-rod diameter, the electron mobility can be enhanced from 83 to 228 cm^{-1}/Vs along (1-100) direction and 51 to 124 cm^{-1}/Vs along (11-2-3) direction, respectively. To our best knowledge, the electron mobility as high as 228 cm^{-1}/Vs with an electron concentration of $3.42\times10^{17}cm^{-3}$ is the best report for semi-polar GaN grown on sapphire [23].

5.3. Optical Study of InGaN/GaN MQWs on Semi-polar GaN

In order to demonstrate good quality of the overgrown semi-polar GaN films on nano-rod templates, an InGaN/GaN MQW structure has been grown after the overgrowth to investigate optical performance of the semi-polar MQWs. Figure 5.16 is a schematic figure. The InGaN/GaN MQW structure is composed of 10 period InGaN well and GaN barrier thickness with 2.5 nm and 10 nm, respectively. Meanwhile, identical InGaN/GaN MQW structures are grown under the c-plane InGaN/GaN MQW growth conditions on an as-grown semi-polar GaN and a standard c-plane GaN template in order to make comparisons. Note that the growth conditions for InGaN/GaN QWs are not optimized.

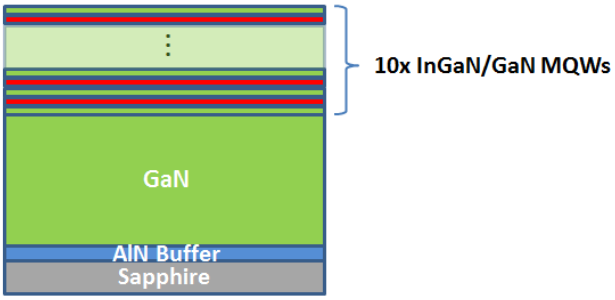

Fig. 5.16: Schematic of an InGaN/GaN MQW sample.

To investigate whether the semi-polar GaN MQWs are partially free of QCSE, excitation power dependent PL experiments are performed by measuring PL spectra at different laser powers. A blue shift in the emission energy with increasing the excitation power is a fingerprint of QCSE in the sample, as high excitation power would mitigate the effect of the energy band bending caused by the QCSE. Figure 5.17 present the excitation power dependent PL spectra of InGaN/GaN MQWs, which were measured at 10K. It can be seen that there is no obvious shift in the peak emission wavelength with increasing the excitation power from 0.5 mW to 15 mW. This demonstrates the small QCSE of the semi-polar InGaN/GaN MQWs.

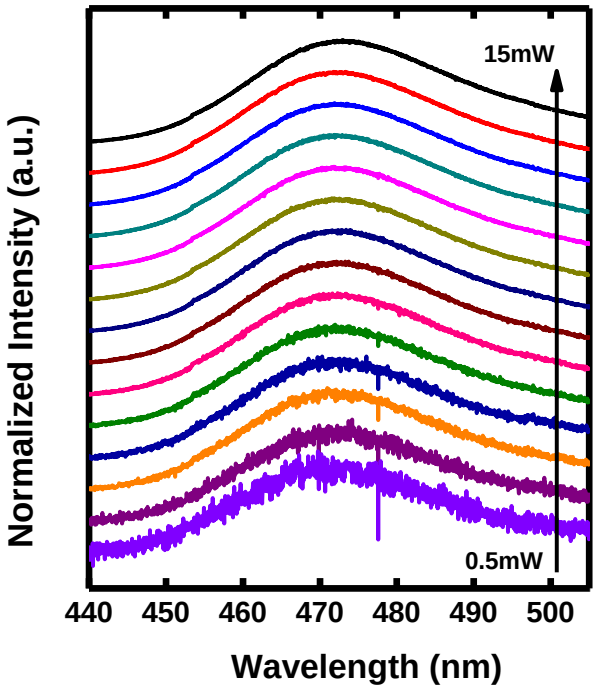

Fig. 5.17: Excitation power dependent PL of InGaN/GaN MQWs on semi-polar overgrown GaN.

Estimation of the internal quantum efficiency (IQE) can be performed by implementing temperature dependent PL measurements. The sample is loaded in a cryostat where the temperature can be reduced down to 10 K. Generally, either photon or phonon is emitted with the recombination of electron-hole pair. Theoretically, there are no thermal vibrations of the electrons at 0 K, thus only the photons can be emitted during the recombination process, which indicates that the IQE is unity at 0K. Therefore, by calculating the ratio between the integrated intensities at 300 K (room temperature) and 10 K, the IQE can be estimated.

Although this method cannot give the accurate IQE value for each sample, but it can provide comparisons of IQEs for different samples as long as they are measured under identical conditions.

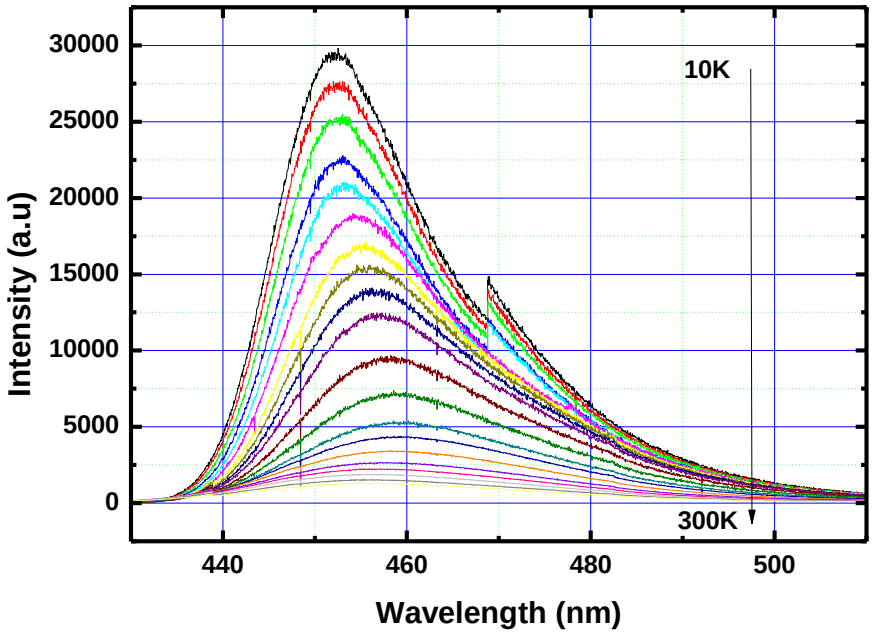

Fig. 5.18: PL spectra of semi-polar InGaN/GaN MQWs measured at temperatures from 10K to 300K.

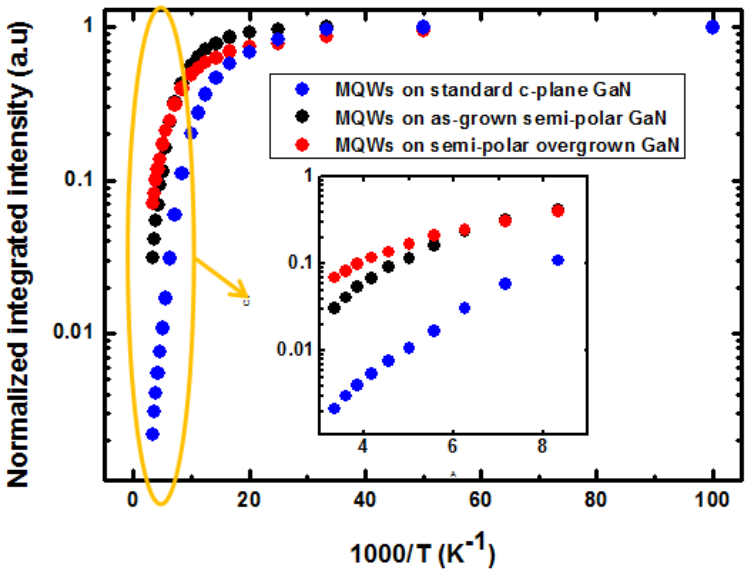

Fig. 5.19: Normalized PL integrated intensity as a function of temperature in an Arrhenius plot.

Figure 5.18 shows PL spectra of semi-polar InGaN MQWs at different temperatures from 10 K to 300 K. The sudden jump at ~467nm is due to the PL CCD. Figure 5.19 presents the normalized integrated intensities of the standard c-plane GaN, as-grown semi-polar GaN template and the semi-polar overgrown GaN, as a function of temperature in an Arrhenius Plot ranging from 10K to 300K. A 375nm diode laser is used as the excitation power source. The results can be seen clearly: compared with the MQWs grown on the standard c-plane sample, the MQWs grown on the as-grown semi-polar GaN have been greatly enhanced. This is predominantly due to the fact that the semi-polar GaN is much less influenced by the QCSE; on the other hand, our semi-polar overgrown GaN demonstrates a further enhancement with a factor of ~5 compared with the as-grown semi-polar template, which is attributed to the massive improvement in crystal quality in our semi-polar overgrown GaN.

5.4. Non-polar GaN Overgrown on Nano-rod Templates

5.4.1. Growth Methodology

The nano-rod template for non-polar GaN overgrowth is fabricated using as-grown (11-20) non-polar GaN grown on the r-plane sapphire substrate. The epitaxial relationship between GaN and sapphire is illustrated in Figure 5.20. Different from the semi-polar GaN template (refer to Figure 5.1a), the (0001) c-axis GaN film is parallel to the sample surface plane.

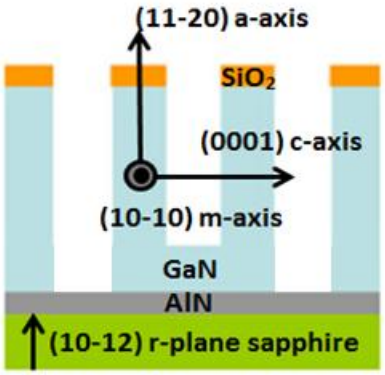

Fig. 5.20: Schematic illustration of the non-polar GaN grown on a nano-rod template.

The non-polar nano-rod template is fabricated using the identical approach as the semi-polar GaN template. Drawing on from experience of the semi-polar overgrowth, the GaN film is etched down to the sapphire substrate in order to force the growth of GaN to initiate only

from the nano-rod sidewall. The average nano-rod size is ~600 nm, and the residue SiO_2 thickness on top of the nano-rod is 200 nm. The growth temperature, pressure and the V/III ratio are 1200^{o}C, 75 Torr and 1600, respectively.

5.4.2. Structural Properties of Non-polar GaN

Figure 5.21 (a) shows the surface morphology of our overgrown non-polar a-plane GaN, taken using SEM. It is clear that the smooth surface has been obtained within the growth of 4-5μm, which is less than the typical thickness obtained by any other conventional ELOG methods. Figure 5.20 (b) shows a typical cross-sectional SEM image of the fully coalesced a-plane GaN film, where two kinds of voids with different sizes have been clearly observed. All the small ones are at the same depth, which is around 2.6 μm above the AlN buffer, i.e., the thickness of the a-plane GaN template. Obviously, the small voids are on the top of the SiO_2 nano-masks, and are formed when the overgrowth extends laterally over the SiO_2 nano-masks to form coalescence. The large voids are ~1.3 μm below the small voids, and the depth is close to the nano-rod length. Having examined the large voids carefully, one can find that those voids locate at the regions between two neighbouring small voids. It means that the large 5 voids are at the regions, which are originally the gaps between nano-rods. Therefore, the formation of the large voids is due to the quick lateral growth from the sidewall of the GaN nano-rods at the initial stage. We have found that the two kinds of voids are always observed in the overgrown a-plane GaN with greatly improved crystal quality. If either of the two kinds of voids disappears, the improvement in crystal quality becomes weak.

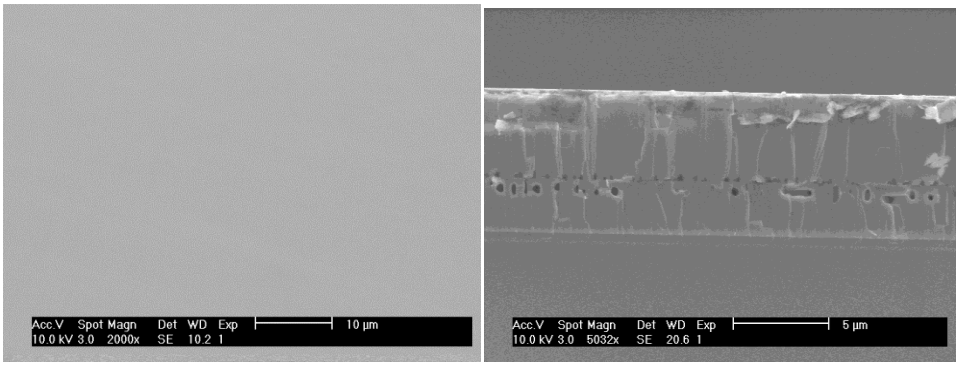

Fig. 5.21: (a) Plan-view and (b) cross-sectional SEM images of the overgrown non-polar GaN.

The XRD is applied to evaluate the overgrown non-polar GaN film crystal quality, which is then compared with a-plane GaN template. The measurement is performed along the (11-20)

direction as a function of the azimuth angle. The azimuth angle is identified as 0 when the projection of the X-ray beam is parallel to the GaN c-axis. The FWHM results of the rocking curves of the standard non-polar template and the non-polar overgrown GaN are shown in Figure 5.22. The FWHM of the standard non-polar template is between 724 and 1188 arc sec. In a remarkable contrast, the FWHM of the overgrown non-polar GaN is significantly reduced from 342 and 460 arc sec.

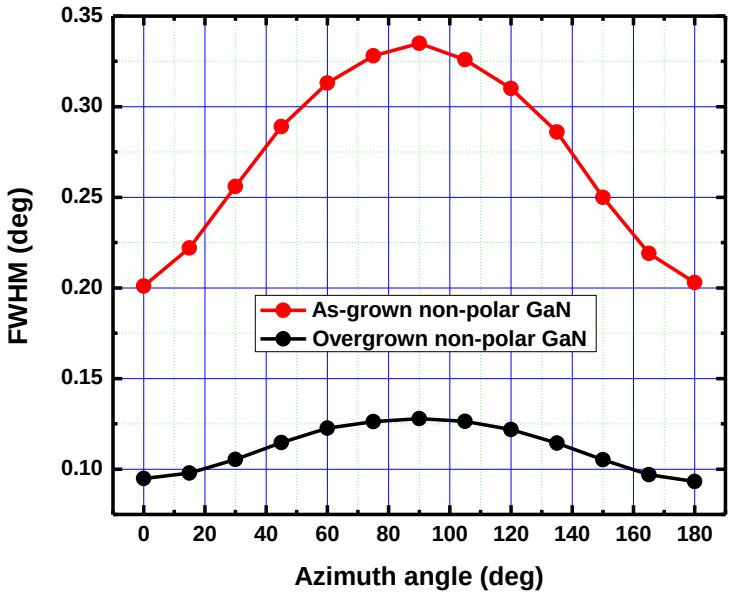

Fig. 5.22: XRD FWHM results as a function of the azimuth angle of standard non-polar GaN template and the overgrown a-plane GaN layer.

In order to provide more evidence to demonstrate the high crystal quality of the non-polar overgrown GaN, the XRD rocking curve measurements are performed along (11-22) and (10-11) asymmetrical directions. The FWHM of the rocking curves along (11-22) and (10-11) of the overgrown non-polar GaN is 392 and 726 arc sec, respectively, which are tremendously improved compared with the non-polar templates (623 and 1534 arc sec).

The results shown above are very close to the current best report, which was achieved by GaN overgrowth based on the conventional UV photolithography [17]. However, with the UV lithography the GaN overgrown layer thickness has to be ~20 μm in order to achieve the smooth surface, as the size and gap of the pattern are both on a micron scale. This is much thicker than that using our self-organized approach (our overgrown GaN thickness is ~5um). This demonstrates the superior crystal quality of our overgrown a-plane GaN, which is also

close to the crystal quality for the c-plane GaN grown on sapphire substrate for fabrication of ultra-high brightness LEDs.

5.5. Optical Study of InGaN/ GaN QWs on Non-polar GaN

In order to demonstrate that the non-polar a-plane overgrown GaN is an excellent candidate for fabricating LEDs, the InGaN/GaN MQWs are grown on the non-polar overgrown GaN to investigate the QCSE and estimate the IQE. The identical InGaN/GaN MQW structure is grown on a standard c-plane GaN in order to make a comparison.

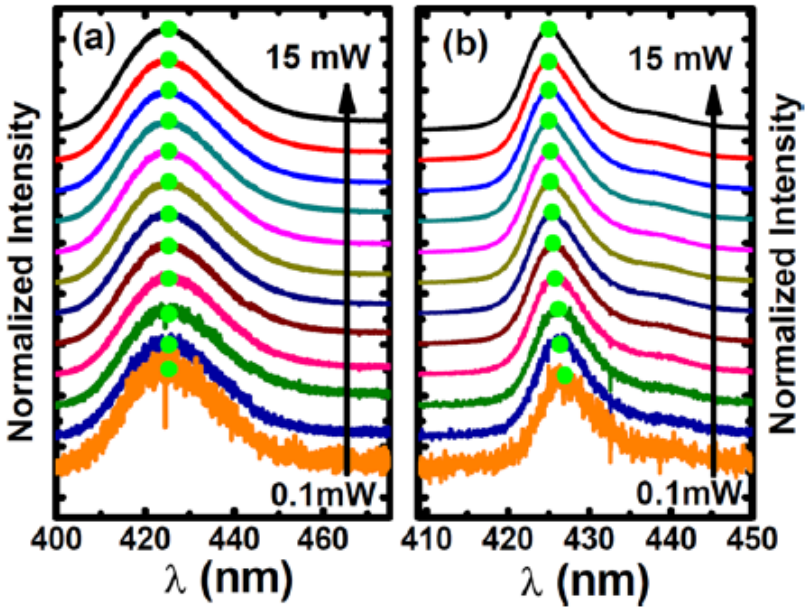

Fig. 5.23: Excitation-power dependent PL measurements of InGaN/GaN MQWs grown on (a) non-polar GaN and (b) c-plane GaN, respectively.

The excitation power dependent PL measurements are performed so as to demonstrate that the non-polar GaN MQWs are free from the QCSE. Figure 5.23 shows the excitation-power dependent PL spectra of InGaN/GaN MQWs grown on the overgrown non-polar GaN and on the c-plane GaN, respectively. Both samples are measured at a temperature of ~10K. There is a clear blue shift for the c-plane InGaN/GaN MQW with the increase of the excitation power, while no shift in the emission wavelength can be observed for the non-polar InGaN/GaN MQW as the excitation power increases, demonstrating that the MQWs grown on non-polar GaN does not suffer from QCSE. Figure 5.24 presents PL spectra of the sample measured at

temperature ranging from 10 to 300K and the Arrhenius plot of the normalized integrated intensity as a function of the temperature. A 375nm diode laser is used as the excitation power source. It can be seen that the IQE of the non-polar InGaN/GaN MQWs is about 12%, showing an enhancement by a factor of 7 compared with the c-plane InGaN/GaN MQWs.

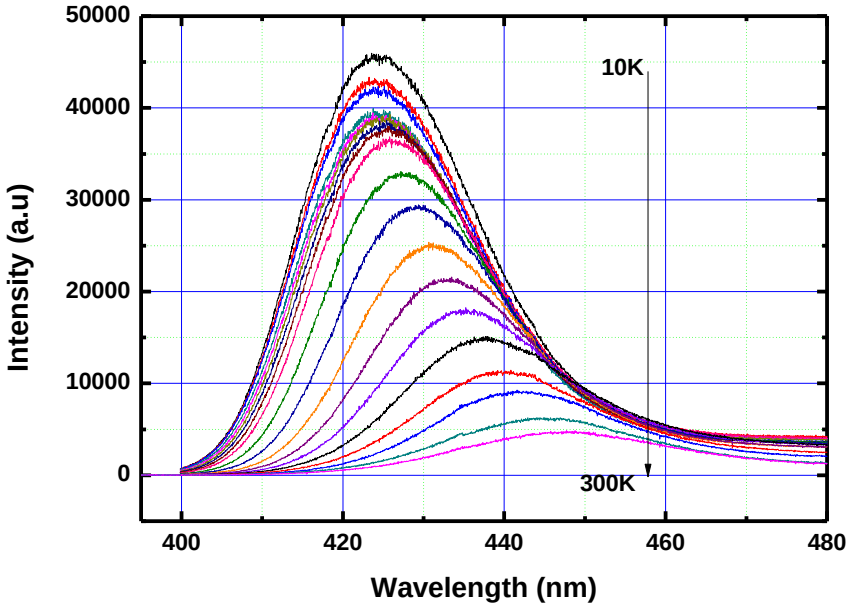

Fig. 5.24 (a): PL spectra of the sample measured at temperature ranging from 10 to 300K for non-polar InGaN/GaN MQWs.

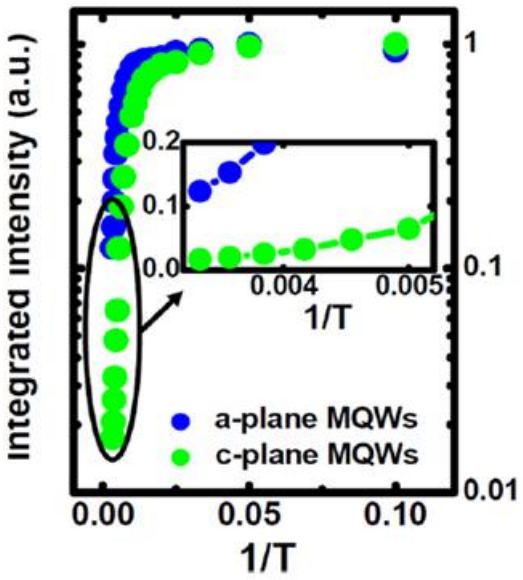

Fig. 5.24 (b): Normalized PL integrated intensity as a function of temperature in an Arrhenius plot, for non-polar and c-plane InGaN/GaN MQWs.

5.6. Mechanism of Defect Reduction in Overgrown Non-polar and Semi-polar GaN

Linear defects such as threading dislocations (TDs) in GaN have been proved to act as non-radiative recombination centres and charge scattering centres, leading to performance degradation of the optoelectronic devices. As mentioned in Chapter 2, one of the major planar defects in both non-polar and semi-polar GaN is basal plane SFs (BSFs), which introduce a quantum-well like cubic GaN region within the wurtzite structure. They serve as the shallow electron traps [24] which normally generate an emission at ~3.41-3.42 eV [24, 25]. Moreover, the partial dislocations bounded to SFs have to be reduced in order to further improve optical performance of either non-polar or semi-polar GaN-based optoelectronics. Therefore, it is extremely important to understand mechanism of defect reduction for further improvement of material quality and thus device performance. In this section, the defects in the overgrown semi-polar GaN films are explored in detail by TEM.

5.6.1. TEM Specimen Preparation

In order to explore mechanism of the significant reduction in the extended defects, cross sectional TEM measurements are performed on the non-polar and semi-polar overgrown samples by Phillips EM 430 TEM.

Figure 5.25 is a schematic diagram of TEM cross-sectional specimen preparation. Two pieces of samples are cut down along a certain direction, and then are stuck by Gatan's G1 epoxy glue, with face to face for the purpose of protecting the epitaxial layer. Two silicon blocking films are added on both sides to prevent the samples from splitting. After baking for about 4 hours at 90 degree, this sandwich structure is transferred onto a plate glass and fixed by wax. Silicon carbide sandpaper with different grit sizes are used to thin it from the top. When its thickness reaches around half, the specimen is turned upside down and thinned it from the other side. As the thickness was about 90um, a Nickel ring was put on the specimen surface and stuck by epoxy glue. With the help of a polishing wheel and diamond paste, specimen was able to be lapped to around 30 μm. After that, it was ion milled to electron transparency by Gatan 600A dual ion mill.

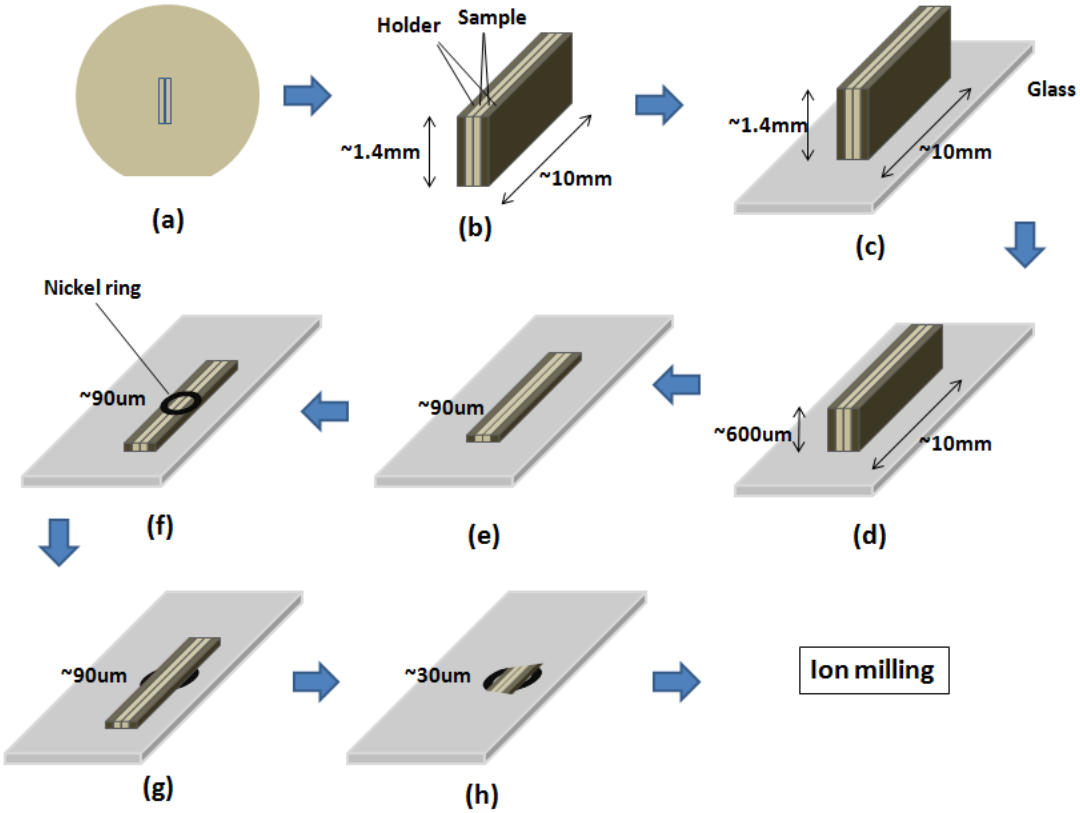

Fig. 5.25: Schematic diagram of TEM cross-sectional specimen preparation.

5.6.2. Defect Reduction in Non-polar Overgrown GaN

Figure 5.26 (a) and 5.26 (b) show the typical cross-sectional TEM images of our overgrown non-polar GaN, taken under two-beam conditions. Figure 5.26(a) was taken with **g**=11$\underline{2}$0 close to the [0001] zone-axis, where the edge **a** TDs, the mixed **a+c** TDs, and the Shockley partial dislocations can be observed. Figure 5.26(b) was taken with **g**=0002 close to the [1$\underline{1}$00] zone-axis, where the screw **c** TDs, the mixed **a+c** TDs, and the Frank partial dislocations can be observed. Even if the original GaN template exists in form of nano-rods at the bottom part with the overgrown GaN in the nano-rod gaps, it can be still seen clearly that the dislocation density in the upper part (i.e., the overgrown GaN) is significantly reduced in comparison with the lower part, which is the original nano-rod template. According to plan-view TEM observation, the dislocation density in the regrown non-polar GaN is in the middle of 10^8 cm^{-2}. As the overgrowth proceeds, the lateral growth extends quickly from the sidewalls of the nano-rods. Due to the nano-rod gap depth of ~1.5 μm, the coalescence takes place quickly,

leaving a lot of voids remained after the overgrowth, which can be observed clearly in Figure 5.26 (a) and 5.26(b).

As observed in Figure 5.26 (a), the original dislocation lines in the nano-rod template move towards free surfaces with the overgrowth. Theoretically, when they are close to free surfaces, the image force induced by image dislocations acts on the inner dislocations and attracts them towards the growth surface. This causes the dislocations to bend. Figure 5.26 (c) is a scanning TEM image, taken at [0001] zone-axis around a void. It can be clearly seen that a lot of threading dislocations redirect to propagate towards the void from the original growth direction. Because the dislocation density in the non-polar template is very high (~10^{10} cm^{-2}), there is a high probability that the bended dislocations encounter each other after their deviation from the original growth direction. As shown in Figure 5.22 (c), these dislocations have been observed to meet each other and then annihilate finally through fusion or forming dislocation loops. Nevertheless, the dislocations in the non-polar GaN can change their line direction only within basal planes, but never deflect out of basal planes [17]. It is also confirmed by our observation that the dislocation bending is observed only in the [0001]-axis cross-sectional view (Figure 5.26 (a) and Figure 5.26 (c)) but never in the [1$\underline{1}$00]-axis cross-sectional view (Figure 5.26 (b) and Figure 5.26 (d)). Figure 5.26 (d) shows a magnified TEM image including three nano-rods taken around [1-100] zone axis, where there is no dislocation bending observed. Moreover, a high density of dislocations is observed in the nano-rods, while there is nearly no dislocation observed in the overgrown areas among and above the nano-rods. Therefore, there are two main pathways for reduction of the dislocation density in our case: enhanced dislocation annihilation due to the line bending in the basal planes; and termination of the dislocations at the free surfaces locally introduced by the voids. Additionally, the SiO_2 (marked by white arrows) was remained deliberately on the top of the nano-rods for the overgrowth, which is different from other reports also using the self-organized Ni nano-mask technique in which SiO_2 was removed prior to growth [18]. The remained SiO_2 plays an important role in both blocking the dislocations and enhancing the lateral growth from nano-rod sidewalls.

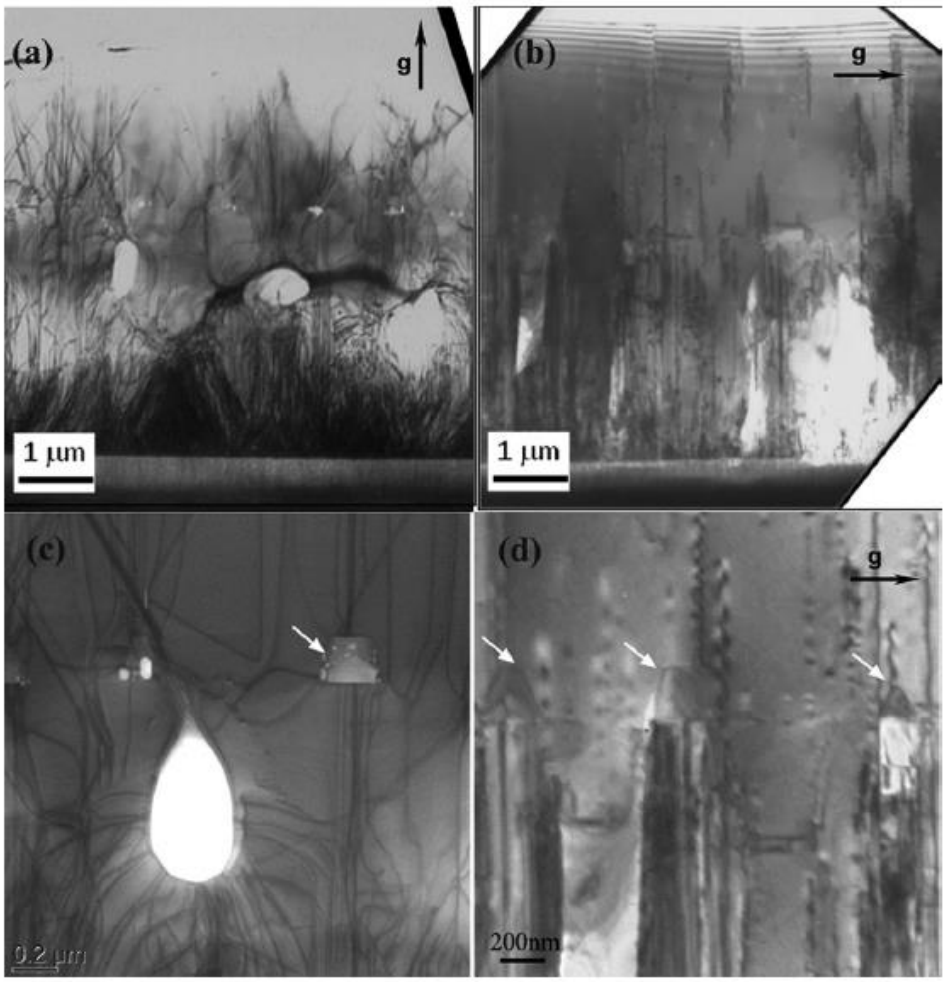

Fig. 5.26: Cross-sectional TEM images of the non-polar overgrown GaN taken close to (a) [0001] zone axis with g=11-20, (b) [1-100] zone-axis with g=0002, (c) [0001] zone axis of magnified TEM images around a void, and (d) [1-100] magnified TEM images around three nano-rods.

It has been reported [16] that the windows of stripes grown from [0001]-oriented stripes in ELOG has a lower dislocation density than from other direction-oriented stripes. It indicates that the growth from [0001]-oriented stripes is more favourable with the TD redirection in basal planes and thus a reduction in dislocation density; while the [1$\underline{1}$00]-oriented stripes has a characteristic of ±[0001] growth, which is not favourable with the TD redirection. However, the advantage of the [1$\underline{1}$00]-oriented stripes is to effectively block BSFs, because the original BSFs lying in basal planes could be impeded through the overgrowth only when the lateral growth proceeds normal to the basal planes. Though the evidence concerning the effect of BSFs on the optical properties of non-polar GaN is inconclusive, a reduction in the BSF density is still expected.

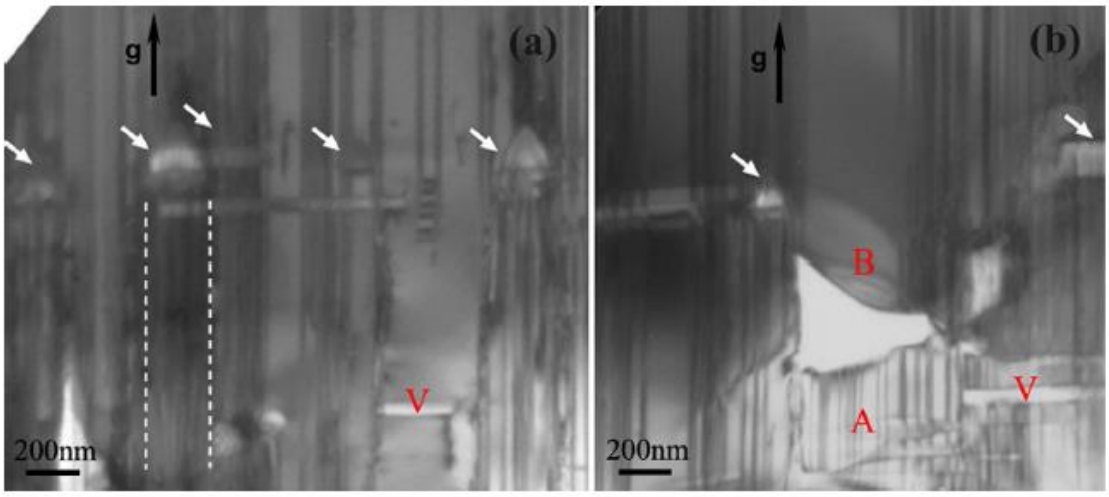

Fig. 5.27: TEM images of the non-polar overgrown GaN, which is taken close to [1-210] under g=10-10 diffraction condition so that BSFs can be observed.

In order to bring the BSFs in the non-polar GaN into contrast, it is necessary to tilt the specimen by ~30° from [1$\underline{1}$00] zone-axis towards [2$\underline{11}$0] or [1$\underline{2}$10] zone-axis during a TEM observation. Figure 5.27 are the TEM images taken under **g**=10$\underline{1}$0 diffraction condition, where the BSFs in form of straight lines perpendicular to the surface can be seen clearly. The BSF density in the overgrown region has been decreased by a factor of 5 to ~1×10^{5}cm^{-1} from ~5×10^{5}cm^{-1} inside the nano-rods. Since the [0001] Ga–face growth is much faster than the [000$\underline{1}$] N-face growth, the coalescence front between nano-rods tends to be close to the N-face side of the nano-rod and thus the BSFs are confined within narrow N-face regions. Therefore, there is nearly no BSFs observed in the nano-rod gaps as shown in Figure 5.27, especially in the right side of the nano-rods which is the Ga-face side. However, occasionally, the overgrowth started from the bottom parts among the nano-rods. As shown in Figure 5.27(b), the BSFs in the original GaN layer propagated with the growth, leading to a high density of BSFs in the region labelled as A. As a contrast, there is nearly no SFs in the region labelled as B. A large void has been observed between region A and region B (partially removed due to specimen thinning), indicating that the GaN in region B is not grown from the underlying GaN in region A but from the sidewalls of the nano-rods. The BSFs are thus blocked out of region B and the area above it. Therefore, in our case, the overgrowth on nano-rods, which starts all around the sidewalls, takes advantage of not only the in-basal-plane growth to reduce the dislocation density, but also the priority [0001] growth to block the BSFs.

5.6.3. Defect Reduction in Semi-polar Overgrown GaN

TEM measurements are also performed for the overgrown semi-polar GaN samples. In the case of the semi-polar GaN grown on a nano-rod template, the dislocations were reduced significantly as well, which is shown in Figure 5.28(a) and 5.28(b). The mechanism for the dislocation reduction is similar to that for the non-polar GaN. However, unlike the non-polar GaN, the BSFs in the semi-polar GaN are tilted to the growth plane with an angle of 58°. Figure 5.28(c) and 5.28(d) are the cross-sectional TEM images of the semi-polar GaN, taken close to [$1\underline{2}\underline{1}0$] zone-axis with **g**=$10\underline{1}0$. This allows us to observe the BSFs clearly in form of declining straight lines. Some BSFs still appear in the region of the gaps between the nano-rods but much fewer in the regions above the nano-rods. One can notice that there are some other voids (marked with red V) observed in the right side of the SiO_2 on the nano-rods. The voids appear in a shape showing a narrow slit tilting by 58° from the surface, namely, tilting along c-direction.

The type of voids has also been observed in the overgrown non-polar GaN, where the c-direction is perpendicular to the growth direction. As shown in Figure 5.27, they emerge in the gap area of nano-rods and lying along the c-direction. It indicates that when the +**c** growing wing advances and then meets with another growing wing, the growth front is actually truncated with {$11\underline{2}$n} planes. The vertical sidewalls of nano-rods could trigger the lateral growth perpendicular to the sidewalls in either the non-polar GaN or the semi-polar GaN. However, the lateral growth in the nano-rod gaps is along ±[0001] direction in the non-polar GaN but not in the semi-polar GaN. Therefore, it is more favourable with the non-polar GaN in blocking BSFs than with the semi-polar GaN. It results in no big change in the BSF density in the gap area of the semi-polar GaN (Figure 5.28). Those formed voids which are close to the remaining SiO_2 in the semi-polar GaN suggest: when the growth front moves towards the area above nano-rods, it tends to proceed along the [0001] direction probably due to the high [0001] growth rate. Finally, this leads to an apparent reduction of the BSFs above the nano-rods.

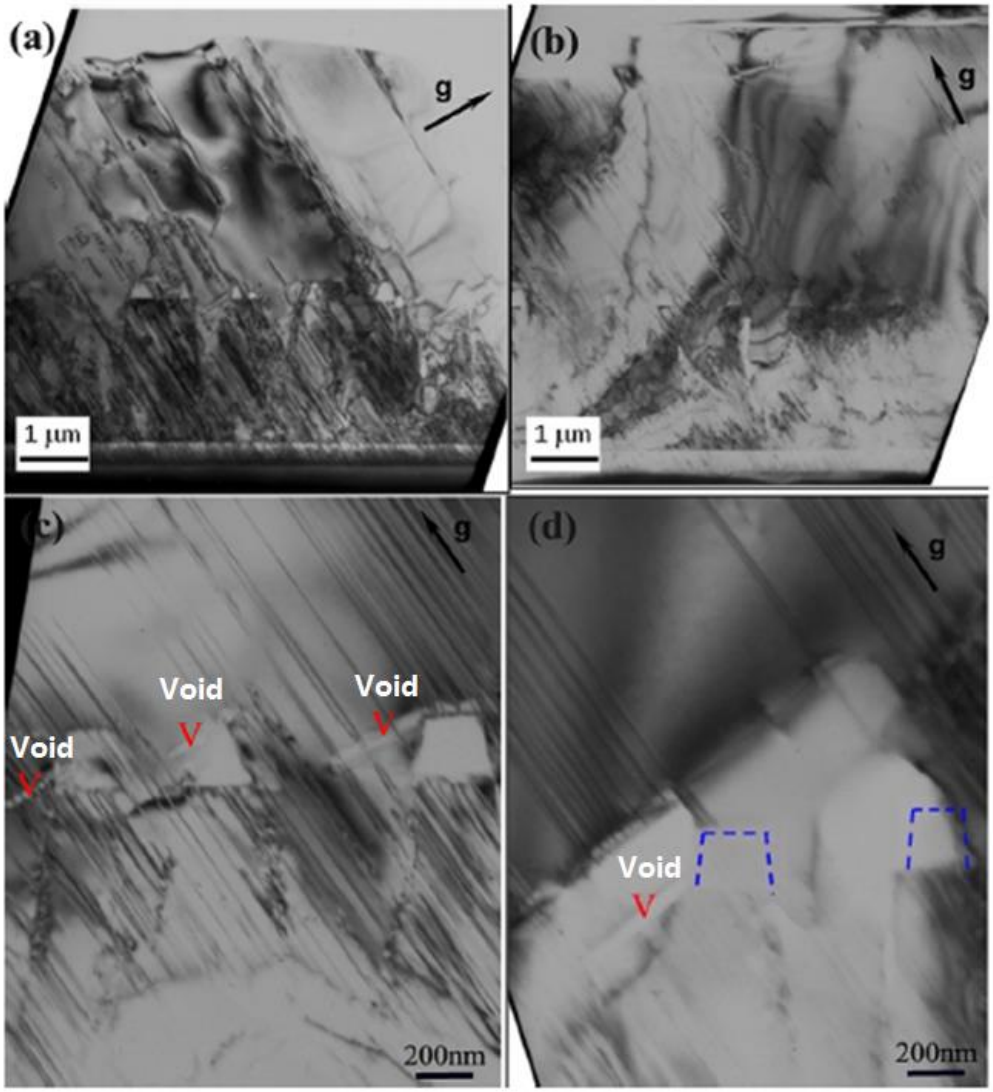

Figure 5.28: TEM images of semi-polar overgrown GaN on standard semi-polar GaN template, taken close to [1-100] zone-axis with (a) g=0002 and (b) g=11-20, respectively; (c) and (d) taken around [-12-10] zone-axis with g=10-10 so that BSF can be observed.

5.7. Conclusions

By using the self-organized Ni approach, we managed to achieve smooth overgrown (11-22) semi-polar and (11-20) non-polar GaN films with very good crystal quality. The XRD results are very close the current best reports achieved by GaN overgrowth based on the conventional UV photolithography. The electron mobility the semi-polar overgrown GaN film is as high as 228 cm^{-1}/Vs with an electron concentration of $3.42\times10^{17}cm^{-3}$, which is the best report for semi-polar GaN grown on sapphire. The InGaN/GaN MQWs grown on the

semi-polar overgrown GaN films exhibit excellent optical property, which is demonstrated by temperature dependent PL measurements with an enhancement factor of 14 compared with the c-plane MQWs, and with a factor of 5 compared with semi-polar as-grown GaN template. The excitation power dependent PL measurements have confirmed that the QCSE in the (11-22) semi-polar MQWs is negligible. For InGaN/GaN MQWs grown on the non-polar GaN film, the excitation power dependent PL measurements also demonstrate that the non-polar GaN MQWs are free from the QCSE. Mechanisms of defect reduction have been explored in detail by TEM observations. The overgrowth on a nano-rod template takes advantages of the omni-directional growth around sidewalls of the GaN rods, which not only significantly reduce dislocations due to the line bending in basal planes, but also effectively block BSFs through priority [0001] growth. The overgrowth technology is proved to be a potentially cost-effective technology to achieve a high quality non-polar and semi-polar GaN exhibiting not only a quick coalescence but also a low defect density with an uniform distribution across a 2-inch wafer.

References

1. M. F. Schubert, J. Xu, J. K. Kim, E. F. Schubert, M. H. Kim, S. Yoon, S. M. Lee, C. Sone, T. Sakong, and Y. Park, Appl. Phys. Lett. **93**, 041102 (2008).
2. A. Avramescu, T. Lermer, J. Müller, S. Tautz, D. Queren, S. Lutgen, and U. Strauβ, Appl. Phys. Lett. **95**, 071103 (2009).
3. S. F. Chichibu, A. C. Abare, M. S. Minsky, S. Keller, S. B. Fleischer, J. E. Bowers, E. Hu, U. K. Mishra, L. A. Coldren, S. P. DenBaars, and T. Sota, Appl. Phys. Lett. **73**, 2006 (1998).
4. P. Waltereit, O. Brandt, A. Trampert, H. T. Grahn, J. Menniger, M. Ramsteiner, M. Reiche, and K. H. Ploog, Nature **406**, 865 (2000).
5. F. Bernardini, V. Fiorentini and D. Vanderbilt, Phys. Rev. B **56**, R10024 (1997).
6. P. Waltereit, O. Brandt, A. Trampert, H. T. Grahn, J. Menninger, M. Ramsteiner, M. Reiche, and K. H. Ploog, Nature (London) **406**, 865 (2000).
7. M. D. Craven, P. Waltereit, J. S. Speck, and S. P. DenBaars, Appl. Phys. Lett. **84**, 496 (2004).
8. A. Chakraborty, B. A. Haskell, S. Keller, J. S. Speck, S. P. DenBaars, S. Nakamura, and U. K. Mishira, Jpn. J. Appl. Phys. **44**, L173 (2005).
9. U. Schwarz and M. Kneissl, Phys. Status Solidi (RRL) **1**, A44 (2007).
10. Y. Kawakami, K. Nishizuka, D. Yamada, A. Kaneta, M. Funato, Y. Narukawa, and T. Mukai, Appl. Phys. Lett. **90**, 261912 (2007).
11. Y. Enya, Y. Yoshizumi, T. Kyono, K. Akita, M. Ueno, M. Adachi, T. Sumitomo, S. Tokuyama, T. lkegami, K. Katayama, and T. Nakamura, Appl. Phys. Express **2**, 082101 (2009).
12. J. P. Liu, J. B. Limb, J.-H. Ryou, D. Yoo, C. A. Horne, R. D. Dupuis, Z. H. Wu, A. S. Fischer, F. A. Ponce, A. D. Hanser, L. Liu, E. A. Preble and K. R. Evans, Appl. Phys. Lett. **92**, 011123 (2008).
13. P. Fini, L. Zhao, B. Moran, M. Hansen, H. Marchand, J. P. Ibbetson, S. P. DenBaars, U. K. Mishra, and J. S. Speck, Appl. Phys. Lett. **75**, 1706 (1999).
14. K. Hiramatsu, K. Nishiyama, M. Onishi, H. Mizutani, M. Narukawa, A. Motogaito, H. Miyake, Y. Iyechika, and T. Maeda, J. Cryst. Growth **221**, 316 (2000).
15. K. Linthicum, T. Gehrke, D. Thomson, E. Carlson, P. Rajagopal, T. Smith, D. Batchelor, and R. Davis, Appl. Phys. Lett. **75**, 196 (1999).

16. B. A. Haskell, F. Wu, M. D. Craven, S. Matsuda, P. T. Fini, T. Fujii, K. Fujito, S. P. DenBaars, J. S. Speck, and S. Nakamura, Appl. Phys. Lett. **83**, 644 (2003).
17. B. Imer, F. Wu, S. P. DenBaars, and J. S. Speck, Appl. Phys. Lett. **88**, 061908 (2006).
18. S. C. Ling, C. L. Chao, J. R. Chen, P. C. Liu, T. S. Ko, T. C. Lu, H. C. Kuo, S. C. Wang, S. J. Cheng, and J. D. Tsay, J. Cryst. Growth **312**, 1316 (2010).
19. S. C. Ling, C. L. Chao, J. R. Chen, P. C. Liu, T. S. Ko, T. C. Lu, H. C. Kuo, S. C. Wang, S. J. Cheng, and J. D. Tsay, Appl. Phys. Lett. **94**, 251912 (2009).
20. X. Ni, Ü. Özgür, A. A. Baski, H. Morkoç, L Zhou, D. J. Smith and C. A. Tran Appl. Phys. Lett. **90**, 182109 (2007).
21. Q. Sun, and J. Han, 'Heteroeppitaxy of non-polar and semi-polar GaN', Springer (2012).
22. D. Iida, M. Iwaya, S. Kamiyama, H. Amano, and I. Akasaki, J. Cryst. Growth **311**, 2887 (2009).
23. S. Jung, S. Lee and H. Kim, Appl. Phys. Lett. **102**, 151603 (2013).
24. C. Stampfl, and C. G. Van de Walle, Phys. Rev. B **57**, R2033 (1998).
25. P. P. Paskov, R. Schifano, B. Monemar, T. Paskova, S. Figge, and D. Hommel, J. Appl. Phys. **98**, 093519 (2005).

Chapter 6

Semi-polar GaN Overgrowth on Micro-rod Templates

6.1. Introduction

In last chapter, an effective overgrowth approach based on nano-rod templates has been presented, and the overgrown GaN crystal quality can be significantly improved by using the self-organized nano-mask approach. The average size of the nano-rod can be achieved from 200 nm to 1 μm. The fast coalescence of the overgrown GaN and smooth surface is achieved. However, there are several limitations and disadvantages by using this technique. Firstly, it is extremely difficult to apply this approach based on larger-sized (3 or 4 inch) sapphire substrate due to the cracking issue during the process of rapid thermal annealing, which makes it less attractive for mass production. Secondly, the largest attainable GaN nano-rod by using the self-organized nano-mask approach is 1 μm, while it has been demonstrated that increasing the average rod size can effectively reduce the coalescence boundary, hence improving the crystal quality. Therefore, other technologies need to be used to further increase the pattern size. In the field of semi-polar/non-polar GaN overgrowth, the mask is normally designed into the periodic stripe pattern with a fixed stripe width and gap. In the early stage, the most common approaches for conventional ELOG are single step ELOG [1, 2] and double step ELOG [3]. Later, a method named Pendeoepitaxy [4, 5] overgrowth and another approach called sidewall ELOG have been developed [6]. However, ELOG approaches have some major drawbacks: poor uniformity in terms of crystal quality due to the limit of conventional photolithography; an atomically flat GaN layer cannot be achieved until the overgrowth layer is ~10-20 μm thick.

In Chapter 4, our practical methodology based on UV mask photolithography for semi-polar GaN growth has been presented. The procedure of template fabrication is simple but effective, and the reproducibility is great. The size of mask pattern is on a micron scale and the diameter of the micro-rod can be accurately controlled. In this chapter, high quality semi-polar GaN films overgrown on the micro-rod GaN templates are presented and

mechanisms in the growth and defect reduction are systematically explored. Furthermore, semi-polar InGaN/GaN multi-quantum well (MQW) samples are investigated in detail to demonstrate that our overgrown semi-polar GaN is a promising candidate for achieving high efficient GaN-based optical emitters.

6.2. Semi-polar GaN Overgrown on Micro-rod Templates

Before the overgrowth, similar to the self-organized nano-rod template, proper surface treatment needs to be performed on the micro-rod template to ensure that the sidewall is sufficiently clean. As the inductively coupled plasma (ICP) etching involves some physical bombardment, some impurities from the etching might remain on the sidewalls of the GaN nano-rods and influence the overgrowth. Therefore, certain chemical solutions are used to remove these impurities to expose the GaN sidewall. Firstly, the hot concentrated HNO_3 acid is applied to remove the Ni. Diluted HF solution cannot be used to remove oxides as it can also remove the SiO_2 masks on top of the nano-rod. Therefore, the diluted KOH solution is used instead. Although it is known that the KOH cannot directly react with SiO_2, it acts as the catalyst and can react with GaN micro-rods. The template is soaked in the 0.05% KOH solution for ~1 min at room temperature, such that the GaN is removed to some degree. The reaction equation is shown as follows:

$$2GaN + 3H_2O \xrightarrow{KOH} Ga_2O_3 + 2NH_3.$$

The other advantage of this step is to heal the sidewall surface, as the dry etching may damage the surface.

6.2.1. Effect of Pattern Orientation on the Overgrowth

After KOH etching, the semi-polar micro-rod template fabricated using the methodology described in section 4.3, is then loaded into low pressure metal organic chemical vapour deposition (MOCVD) for the overgrowth, with the growth temperature, V/III ratio and pressure at 1120^{o}C, 1600 and 75 Torr, respectively. Note that the SiO_2 masks remain on top of micro-rods. The overgrowth on the mask pattern mainly includes three main stages: the

GaN lateral growth from the exposed Ga and N face sidewalls until the surface coalescence; the coalesced face grows vertically and reaches above the mask window; the growing face extends laterally over the wing region and finally achieves the second coalescence.

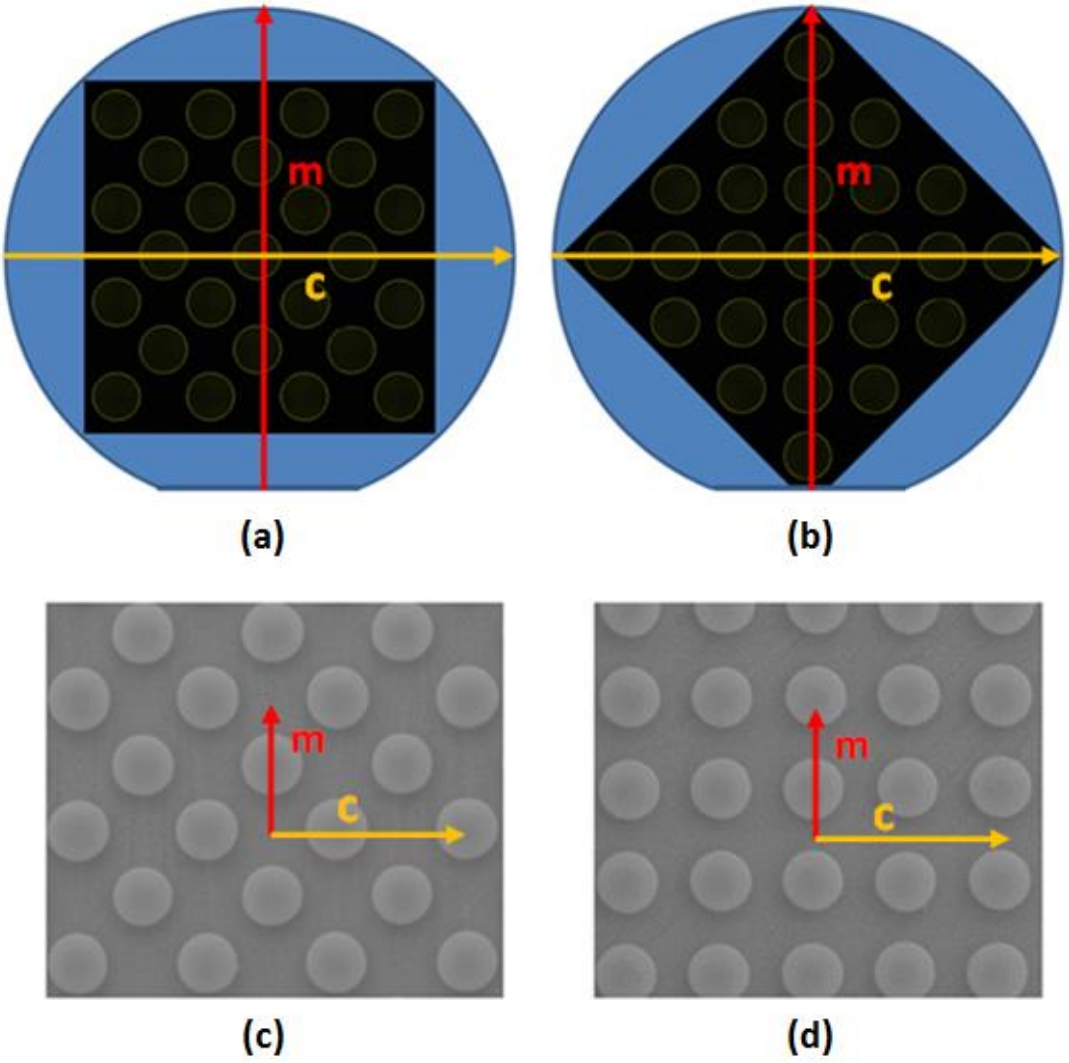

Fig. 6.1: (a) – (b) The mask orientation with respect to the sample orientation cut, and (c) – (d) SEM images of the pattern morphologies.

In order to investigate the pattern orientation dependence of the overgrowth of the semi-polar GaN, the mask is patterned across the two-inch template with two different orientations. For Sample A, the mask edge intersects the orientation cut of sapphire substrates with 45 °while Sample B is patterned with the mask edge parallel to the orientation cut. The schematic drawing of the two conditions are illustrated in Figure 6.1 (a) and (b), where the c and m directions are highlighted. The c direction is parallel to the sample orientation cut and m direction is perpendicular to the sample orientation cut. Figure 6.1 (c) and (d) present

scanning electron microscope (SEM) images of the resultant mask morphologies. The rest of the fabrication conditions for Sample A and B are identical in order to make comparisons. Due to the anisotropic nature of the GaN growth rate along different orientations, it is expected that these two pattern arrangements will lead to completely different results.

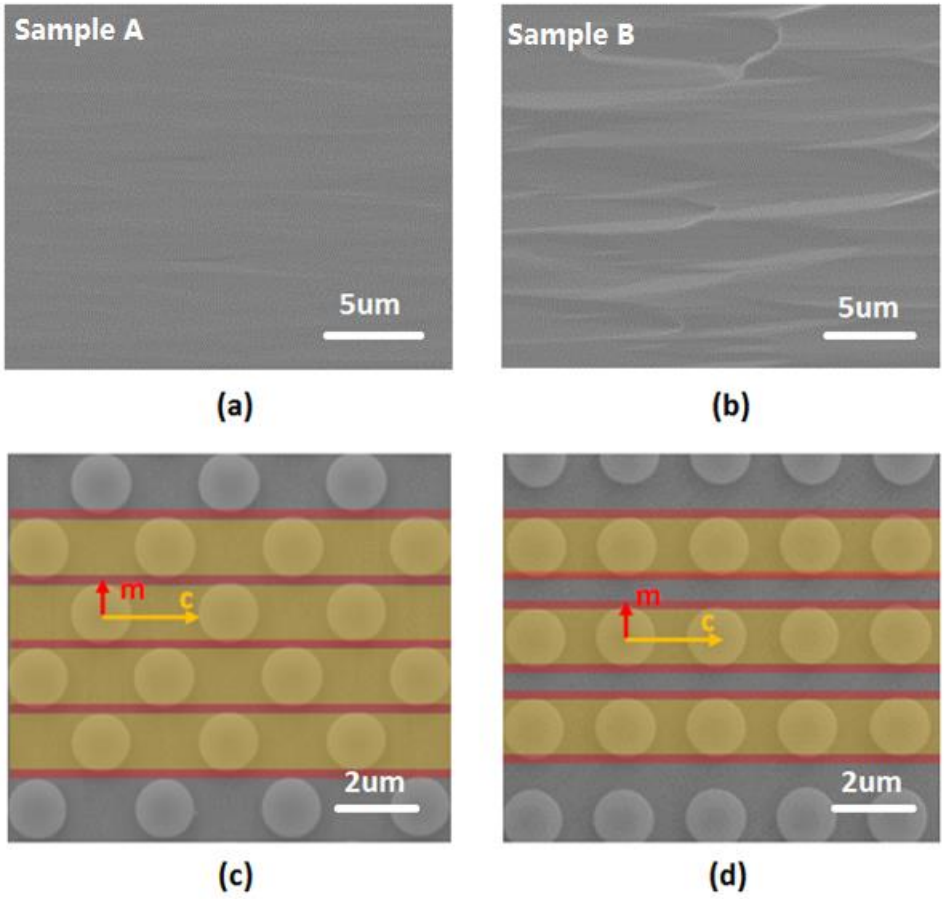

Fig. 6.2: SEM images showing surface morphologies of (a) Sample A, and (b) Sample B; corresponding schematic illustration of (c) Sample A, and (d) Sample B.

Figure 6.2 (a) and (b) show the surface morphologies of Sample A and B measured by SEM. It can be clearly seen that the Sample A has much smoother surface than Sample B, and the stripes of sample B are much stronger than Sample A. Figure 6.2(c) and (d) illustrate the growth models for both samples: as the growth rate along c direction is much faster than that along m direction, the full coalescence of Sample A requires sufficient growth rate along **c** direction and a relatively slower growth rate along **m** direction. Therefore, the growth model is consistent with the mask pattern arrangement where the gap distance along **c** direction is longer than that along **m** direction, which leads to a smooth surface. On the other hand for Sample B, due to same gap distances along two directions but anisotropic growth nature, the coalescence along m direction is not completed yet when the coalescence along the **c**

direction is completed. This leaves a growth gap along **c** direction, which makes the coalescence more difficult. This explains why Sample B has a rougher surface than Sample A.

Figure 6.3 shows the Atomic force microscopy (AFM) image of the semi-polar GaN with a scan area of $1 \times 1\ \mu m^2$, respectively, where the stripe-like pattern on the sample surface can be observed, which demonstrates that the GaN growth rates in different orientations have strong anisotropic feature. In order to investigate the surface flatness, the root mean square (RMS) roughness is calculated. The RMS roughness is defined as the standard deviation relative to the average surface height, which is normally used to measure the temporal changes or spatial difference of a surface. The RMS value of the surface roughness of our semi-polar overgrown GaN with $1 \times 1\ \mu m^2$ image is equal to 1.44 nm, respectively, the typical value of the semi-polar GaN grown on the sapphire substrate.

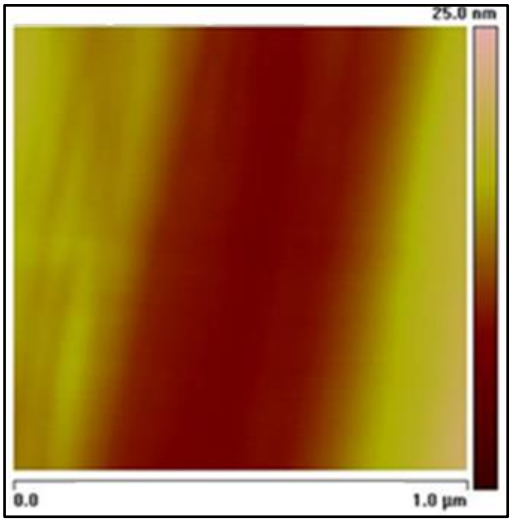

Fig. 6.3: $1 \times 1\ \mu m^2$ AFM image of overgrown semi-polar GaN sample.

The X-ray diffraction (XRD) rocking curve measurement of Sample A and B are performed along the symmetrical on-axis (11-22) direction as a function of azimuth angle. The azimuth angle is defined as $0°$, where the projection of the X-ray beam onto the sample surface is parallel to the $(10\underline{1}0)$ (that is, **m**) direction, and $90°$ is defined where the incident beam is perpendicular to the $(10\underline{1}0)$ direction. As an example, Figure 6.4 shows the on-axis XRD rocking curve at the azimuth angle of $0°$ for the overgrown semi-polar GaN on a 1.5 µm micro-rod template, showing a full width at half maximum (FWHM) of $0.116°$. Figure 6.5 illustrates the FWHM of the XRD rocking curves of Sample A and B measured along (11-22) direction as a function of azimuth angles ranging from $0°$ to $180°$. The FWHM rocking curve

result of Sample B is between 508 and 587 arc sec. As a contrast, The FWHM of Sample A has been significantly reduced to 410 and 475 arc sec. This result is among the best report where ELOG techniques are applied (as introduced in Section 2.7) and the overgrown GaN layer is 20 μm (our overgrown GaN film is only 4~5 μm).

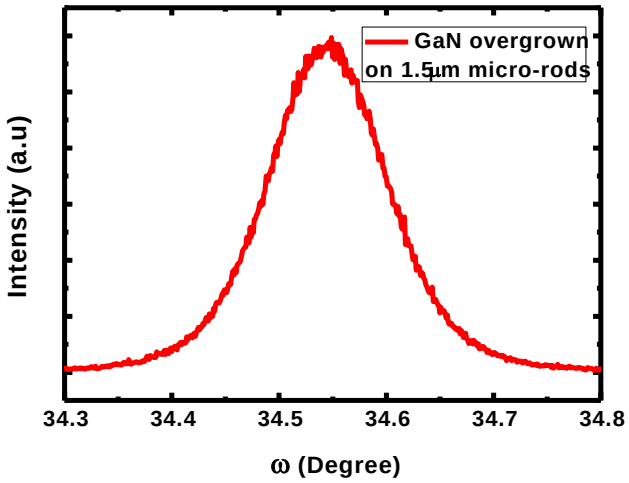

Fig. 6.4: XRD rocking curve of semi-polar GaN overgrown on a 1.5 μm micro-rod template measured along on-axis (11-22).

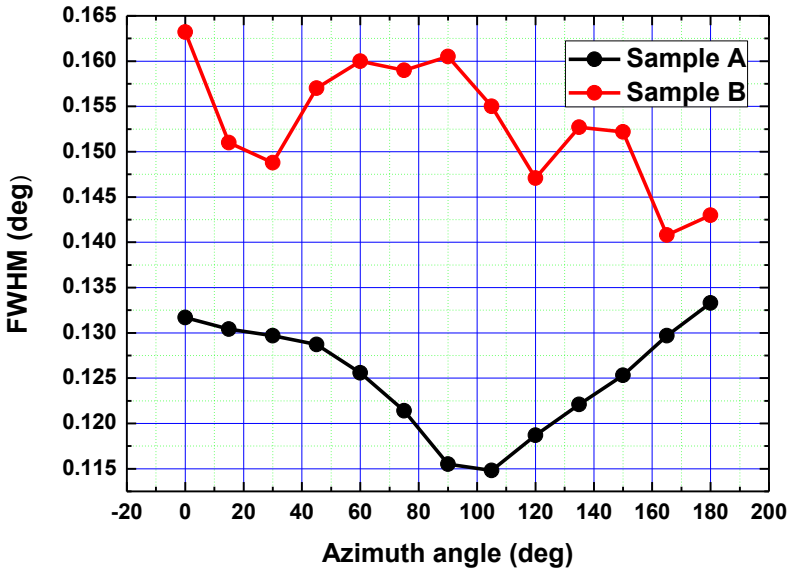

Fig. 6.5: The XRD FWHMs of Sample A and B measured at azimuth angles ranging from 0^{o} to 180^{o}.

The off-axis XRD rocking curve measurements have also been carried out along asymmetrical (0002) and (10-10) of the two semi-polar overgrown samples in order to

accumulate more evidence. The FWHM results of the XRD rocking curves along (0002) and (10-10) of Sample A are 626 and 497 arc sec, respectively, which are tremendously reduced from 688 and 670 arc sec for Sample B. The off-axis XRD results of Sample B are also comparable to the best reports using conventional ELOGs.

6.2.2. Effect of Micro-rod Size on Structural Properties

Drawing on the experience of the overgrowth based on the self-organized nano-masks, it is known that the crystal quality of overgrown GaN layer improves significantly with increase of the rod size, due to reduction of the number of coalescence boundaries. Therefore, in order to investigate effect of micro-rod size on the crystal quality, new masks with same circular array pattern but different sizes are manufactured, where the circles are 2.5 μm and 3 μm in diameter, respectively. Figure 6.6 shows the plan-view SEM images of the semi-polar templates based on the 1.5 μm, 2.5 μm and 3 μm masks. The diameter can be accurately controlled and the pattern has very good shape and uniformity.

The same fabrication methodology is conducted on as-grown semi-polar GaN templates by using the 2.5 μm and 3 μm masks. These two micro-rod templates are then re-loaded into the MOCVD to perform the overgrowth, under the identical growth conditions as the 1.5 μm micro-rod template.

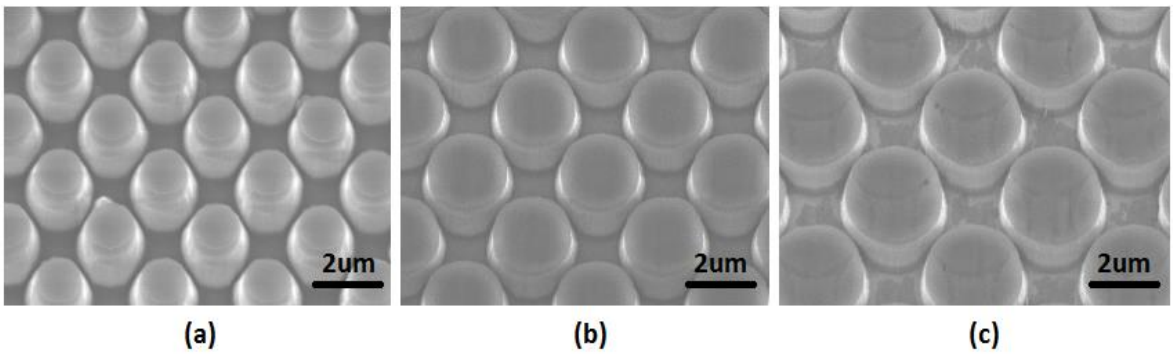

Fig. 6.6: Plan-view SEM images of semi-polar micro-rod templates fabricated based on (a) 1.5, (b) 2.5 and (c) 3 um masks, respectively.

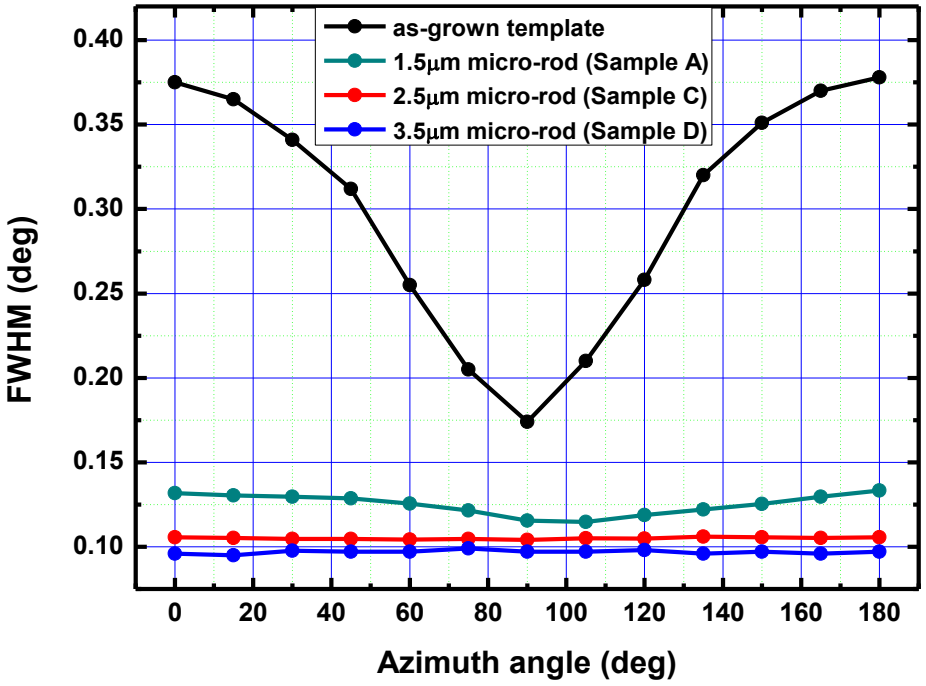

Fig. 6.7: The XRD FWHMs of as-grown semi-polar template and overgrown GaN samples on the 1.5, 2.5 and 3 μm micro-rod templates, measured at azimuth angles ranging from 0^o to 180^o.

The crystal quality of overgrown GaN samples based on 2.5 and 3 μm masks (Sample C and D) are studied by XRD measurements. Figure 6.7 illustrates the FWHM results of on-axis XRD rocking curves for Sample A, C and D as a function of azimuth angle. The FWHM of standard semi-polar template are also included in order to make comparisons. The FWHM of the XRD rocking curve for the template is between 1350 and 630 arc sec, respectively. The XRD FWHM for Sample A based on 1.5 μm mask is between 461 and 428 arc sec, a massive reduction in the dislocation density compared with that of the template. The XRD FWHMs for Sample C and D are between 382 and 392 arc sec and 342 and 350 arc sec, respectively. It can be seen that the FWHMs for Sample C and Sample D are narrower than those for Sample A across the whole azimuth angle range. However, those of Sample C and D are quite close to each other with azimuth angle ranging from 0^o to 180^o, indicating that the crystal quality has almost reached a saturation point.

Off-axis	Sample A (1.5μm)	Sample C (2.5μm)	Sample D (3.0μm)
(0002)	0.191 º	0.174 º	0.146 º
(0004)	0.187 º	0.170 º	0.125 º
(0006)	0.256 º	0.192 º	0.132 º
(10-10)	0.187 º	0.138 º	0.102 º
(20-20)	0.170 º	0.134 º	0.098 º
(30-30)	0.132 º	0.107 º	0.094 º

Tab. 6.1: FWHM results of off-axes XRD for Sample A, C and D.

The XRD measurements are also performed along asymmetrical (0002), (0004), (0006) and (10-10), (20-20), (30-30) off-axis in order to accumulate more evidence. Table 6.1 illustrates all the XRD FWHM results of Sample A, C and D along the asymmetrical axes. A massive improvement in the crystal quality has been achieved for Sample D, which is based on the 3 μm mask; the sample based on 2.5 μm mask (Sample C) is better than that based on 1.5 μm mask (Sample A). This is very consistent with the on-axis XRD measurements. It indicates that the crystal quality of the semi-polar GaN further improves significantly with increase of the micro-rod size.

6.2.3. Characterization of Optimized Overgrown Semi-polar GaN

Through a series of experiments on optimization, high-quality semi-polar GaN has been achieved on templates with 3 μm micro-rods. Figure 6.8 is an optical microscopy image (×1000), showing a smooth surface achieved within a 4-5 μm overgrowth, with a pattern underneath.

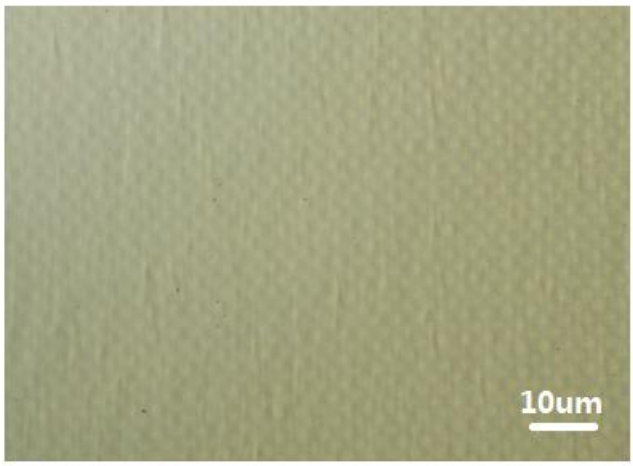

Fig. 6.8: Optical microscopy image of overgrown semi-polar GaN.

XRD measurements are carried out on the optimized sample to demonstrate the crystal quality. As shown in Figure 6.9, the XRD rocking curve along (11-22) demonstrates a very narrow FWHM of 347 arc sec (~0.0963 º). Figure 6.10 and Figure 6.11 illustrate the decrease of on-axis and off-axis FWHM values with optimization, respectively. It can be seen, after optimizing, the on-axis FWHM values finally drop down to below 0.1 º (red circles in Fig.6.10) across the whole range of Azimuth angle from 0 ºto 180 º, which are among the best reports using ELOG approaches.

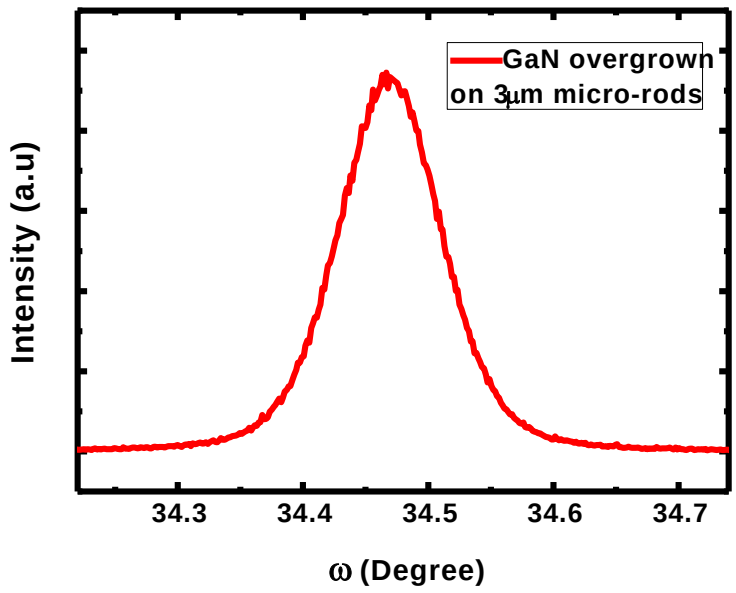

Fig. 6.9: On-axis XRD rocking curve of overgrowth GaN on a 3 μm micro-rod template.

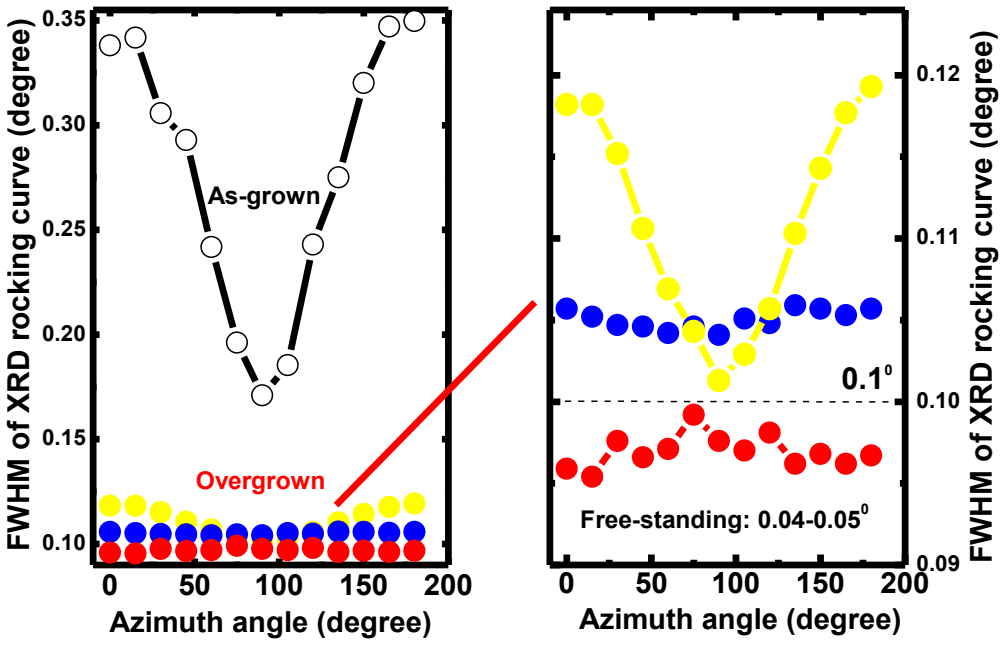

Fig. 6.10: Decrease of on-axis XRD FWHMs through optimization of overgrown semi-polar GaN.

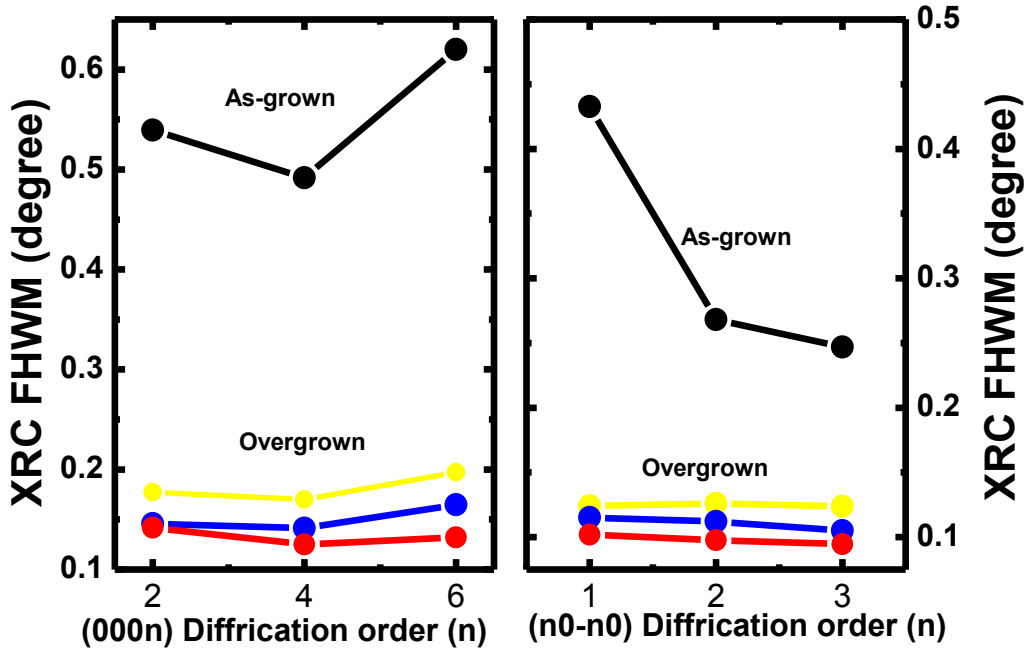

Fig. 6.11: Decrease of off-axis XRD FWHMs through optimization of overgrowth semi-polar GaN.

It is known that the XRD FWHMs for the semi-polar GaN grown on free-standing GaN are about 0.04-0.05°. It is still a long way to go in order to compete with the 300 μm

free-standing GaN. However, it is worth mentioning that the free-standing GaN substrate is very expensive and extremely hard to obtain, and it is only perfect for demonstrating the great nitride-based device performances whereas not available for the mass production. Figure 6.12 shows the free-standing GaN with a very small area of $1 \times 1 cm^2$. Our semi-polar GaN wafer with very smooth surface across a 2-inch wafer, as shown in Figure 6.12, demonstrates a very promising result for mass production of semi-polar GaN based devices.

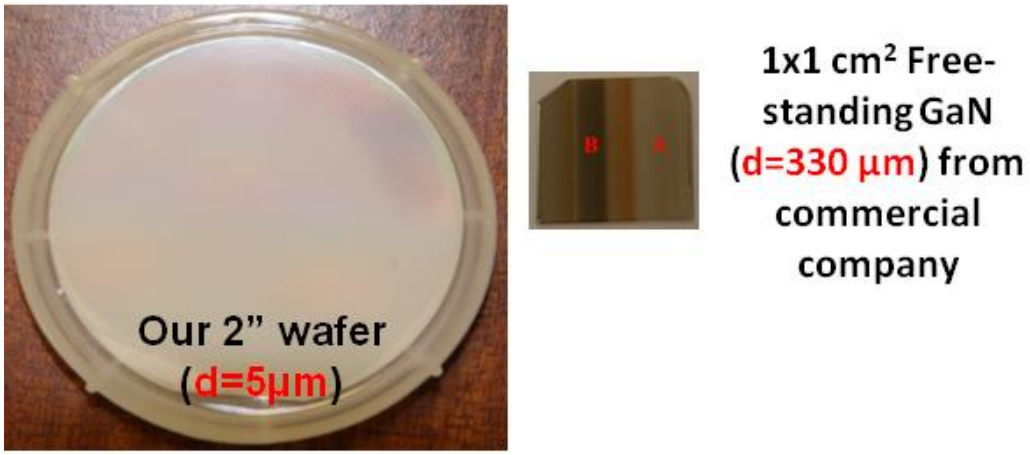

Fig. 6.12: Photos of our 2-inch semi-polar GaN and of $1 \times 1 cm^2$ free-standing GaN.

The optical performance is evaluated on the sample by photoluminescence (PL) at 10K, using a 325 nm He-Cd laser with a laser power of 10 mW. Figure 6.13 shows the PL spectra of the sample, which has two strong emission peaks and other very weak emissions at longer wavelengths. The emission at 356 nm (~3.47eV) is ascribed to the recombination of the donor-bound exciton D^oX (near band edge emission NBE) [7]. The strong emission at 363 nm (~3.43eV) is related to recombination of excitons bound to the basal stacking faults (BSFs) [8, 9], and the intensity has been normalized in order to compare with the NBE peaks. The emissions at 369 nm (3.35 eV) and 376 nm (3.29 eV) are associated with the prismatic stacking fault (PSF) and the partial dislocation (PD), respectively [9]. The material quality improvement due to defect reduction can be assessed by evaluating the intensity ratio between the NBE and defect-related emission in each semi-polar GaN sample. Normally for semi-polar GaN, the intensity of the NBE is much lower than that of the BSF-related emission. For our sample here, the ratio I_{NBE}/I_{BSF} between the NBE and the BSF emissions is about 2.8, indicating that the BSF density has been significantly reduced in our semi-polar overgrown GaN.

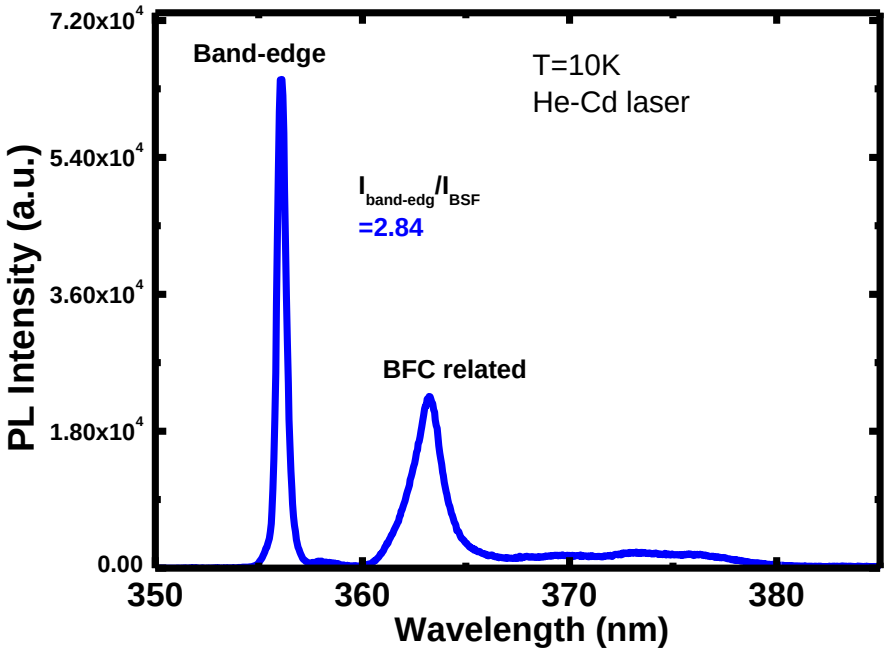

Fig. 6.13: Normalized PL spectra of overgrown semi-polar GaN measured at 10K.

6.2.4. Uniformity in a 2-inch Wafer of Semi-polar GaN

Since the non-uniformity in the crystal quality is a serious issue for usual semi-polar GaN grown using conventional ELOG approaches, the uniformity in the crystal quality of our samples has been investigated across the whole 2-inch wafer by measurements of XRD rocking curves. Figure 6.14 is a schematic figure of a 2-inch wafer, where 5 typical positions are measured, labelled as A, B, C, D and E, respectively. Table 6.2 presents the FWHM values of XRD rocking curves along (11-23) and (1-100) for the 5 positions. The largest difference among the FWHMs for different positions are only 0.0063 º (~13 are sec) and 0.0065 º(~23 arc sec) for measurements along (11-23) and (1-100), respectively.

In conclusion, with our good quality micro-rod templates, we have achieved the 2-inch wafer semi-polar GaN with high crystal quality, smooth surface morphology, good uniformity and high reproducibility.

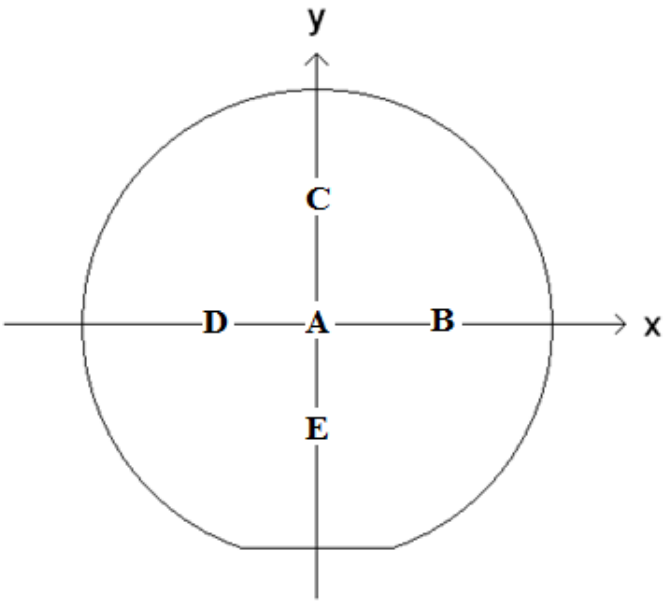

Fig. 6.14: Schematic figure of a 2-inch wafer, where 5 positions labelled as A – E are measured by XRD to investigate the uniformity in crystal quality.

	Coordinate (X,Y) (mm)	**FWHM along (11-2-3)**	**FWHM along (1-100)**
A	**(0, 0)**	**0.0963 º**	**0.0972 º**
B	**(10, 0)**	**0.0999 º**	**0.1007 º**
C	**(0, 10)**	**0.0941 º**	**0.0988 º**
D	**(-10, 0)**	**0.1004 º**	**0.1021 º**
E	**(0, -10)**	**0.0978 º**	**0.1037 º**

Tab. 6.2: The FWHM results of XRD rocking curves measured on 5 positions on the wafer, as labelled in Fig.6.14.

6.3. Study of Growth Mechanism and Defect Suppression in Overgrown Semi-polar GaN

In order to further investigate the overgrowth model and mechanism in defect reduction, a systematic study of the GaN overgrowth on our semi-polar micro-rod templates fabricated based on the UV photolithography is performed, where different growth times at 1000, 2000 and 3000 sec are carried out, respectively. SEM experiments are performed to check the surface morphology of the samples from different perspectives (top and cross-section). Transmission electron microscope (TEM) experiments are carried out to observe the defects and their reduction using Philip EM430. The TEM specimens are prepared as detailed in section 5.6.

6.3.1. Growth Mechanism

The overgrowth process can be divided into three primary stages, which are identified as 'side, up and over', respectively [11]. The detailed growth model is set up and is illustrated as follows.

The first stage 'side' is identified as the GaN growth primarily from the exposed sidewalls. From Figure 6.15 (a), the micro-rod can be clearly observed and the growth of GaN is initiated along the **c** or **a** direction. The **c**-growth facet has the arrowhead shape whilst the **a**-growth facet is wider. By measuring the length of the growing wings, it can be calculated that the estimated growth rate of the GaN along **c** and **a** direction are 1.2 and 0.7 nm/s, respectively. And the growth along **m** direction is almost negligible. The key point of this step is that the GaN growth from the bottom needs to be suppressed in order to prevent the threading defects penetrating to the overlying structures. Therefore, the etching of GaN has to be through the AlN film and down to the sapphire substrate.

The second stage is defined as 'up', when the GaN growing faces tend to move upwards and eventually reach above the SiO_2 masks after the first coalescence finishes. Figure 6.15(c) and (d) show the surface and cross-sectional morphologies after 2000 sec growth. In this stage, the first coalescence has completed and the growing face has started to move up. This leaves voids among the adjacent micro-rods. The voids extend from the sapphire substrate up to the

top of the GaN micro-rods, confirming that the growth is initiated from the exposed sidewalls rather than bottom.

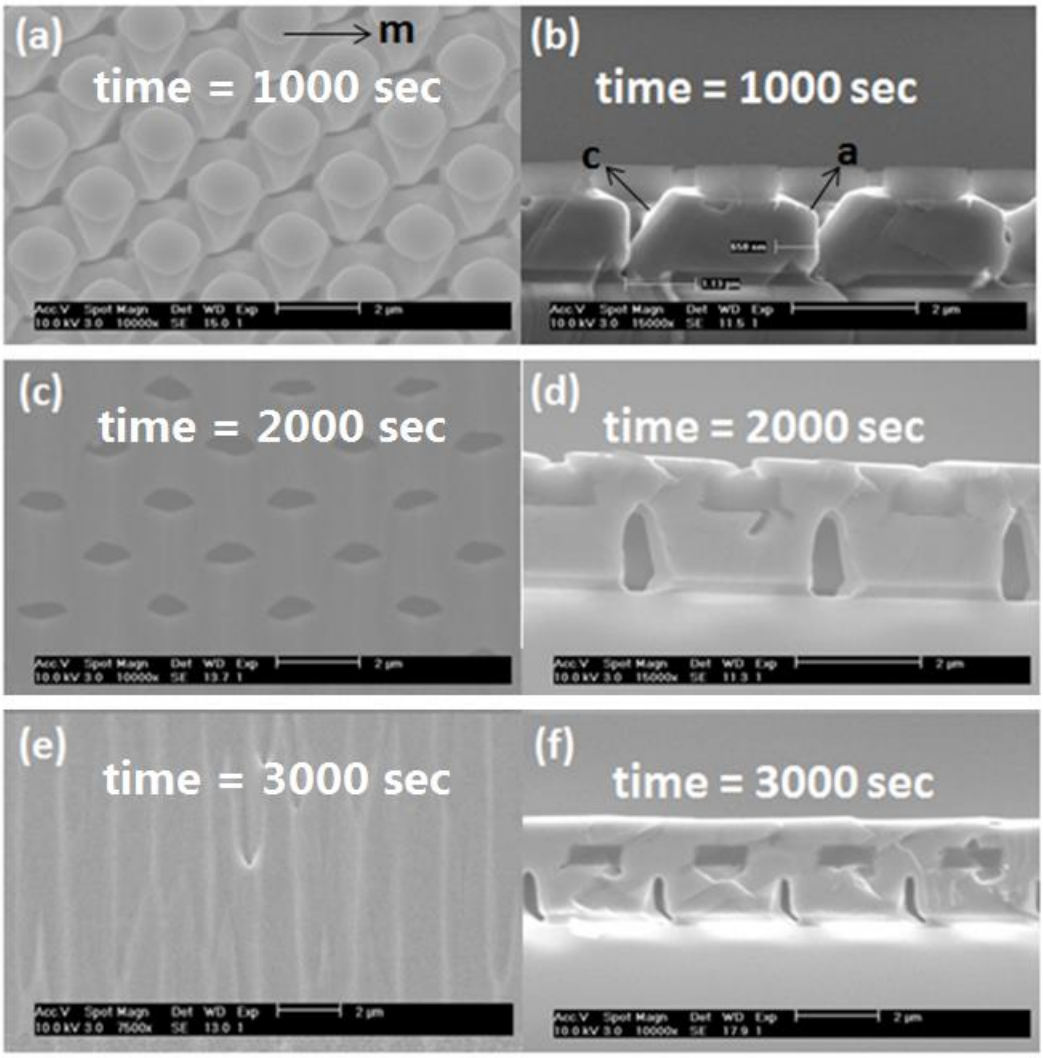

Fig: 6.15: Top-view and cross-sectional SEM images of semi-polar GaN overgrown for 1000, 2000 and 3000 sec, respectively.

The third stage is named as 'over', meaning the growth extends laterally over the SiO_2 masks and eventually achieves the second coalescence. Figure 6.15(e) and (f) present the surface and cross-sectional images after 3000 sec growth, at which the full coalescence is completed. This leaves another small triangle residue voids on top of the SiO_2 masks. Due to the anisotropic growth rate, stripe features perpendicular to **m** direction can be observed on the surface. During this three-stage process, the full coalescence of GaN can be obtained within only ~ 1 μm, and the atomically flat layer can be obtained within 4-5 μm thickness. This is much faster than that using conventional ELOG approaches, where the overgrown GaN layer has to be ~10-20 μm thick in order to obtain the smooth surface.

6.3.2. Mechanism of Defect Reduction

Figure 6.16 are cross-sectional TEM images of the semi-polar GaN grown for 1000 sec, taken around [1-100] zone-axis. A thin layer of nickel is deposited on the sample to protect the GaN films from damaging during the process of Ion-milling thinning. Due to different imaging conditions, the dislocations and BSFs can be observed in image (a) and (b), respectively. It is observed that the film at the right-side of micro-rods is thicker than that at the left side, which agrees well with the SEM image of Figure 6.15 (a). Actually, the right side film of micro-rods in Figure 6.16 is grown along +**c** wing, while the left side film is grown along +**a** direction of GaN. It leads to that the growth facet at the right side appears as c-planes and the one at the left side as a-planes. Furthermore, the pre-existing BSFs in micro-rods are observed with their line direction parallel to the c-planes. It is known that the BSFs lying on basal planes could be impeded through the growth along the +**c** direction. Therefore, no BSFs are present in the film of the +**c** wing overgrown form the micro-rod sidewalls, whereas the pre-existing BSFs extend into the overgrown film at the left side where the growth is along **a** direction. It indicates that the first stage growth is of significant importance for the crystal quality of the overlying GaN film, because at first stage can the pre-existing defects be impeded from propagating by the +**c** growth and make the crystal free of defects dominant in the overgrown film. Therefore, the micro-rods and sidewalls should be very clean for the initial growth.

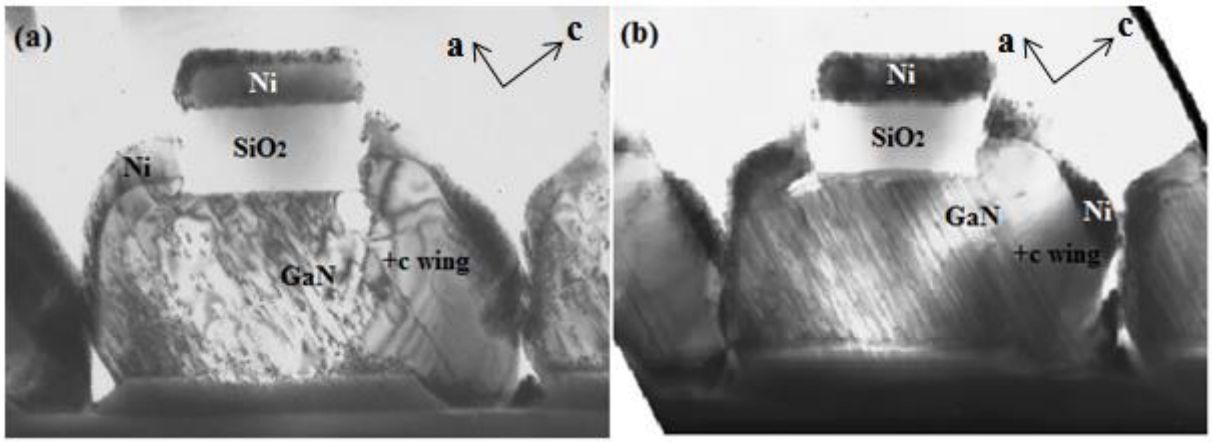

Fig. 6.16: Cross-sectional TEM images of the semi-polar GaN grown for 1000 sec on a micro-rod template, taken around [1-100] zone-axis with (a) **g**=11-22; (b) **g**=10-10

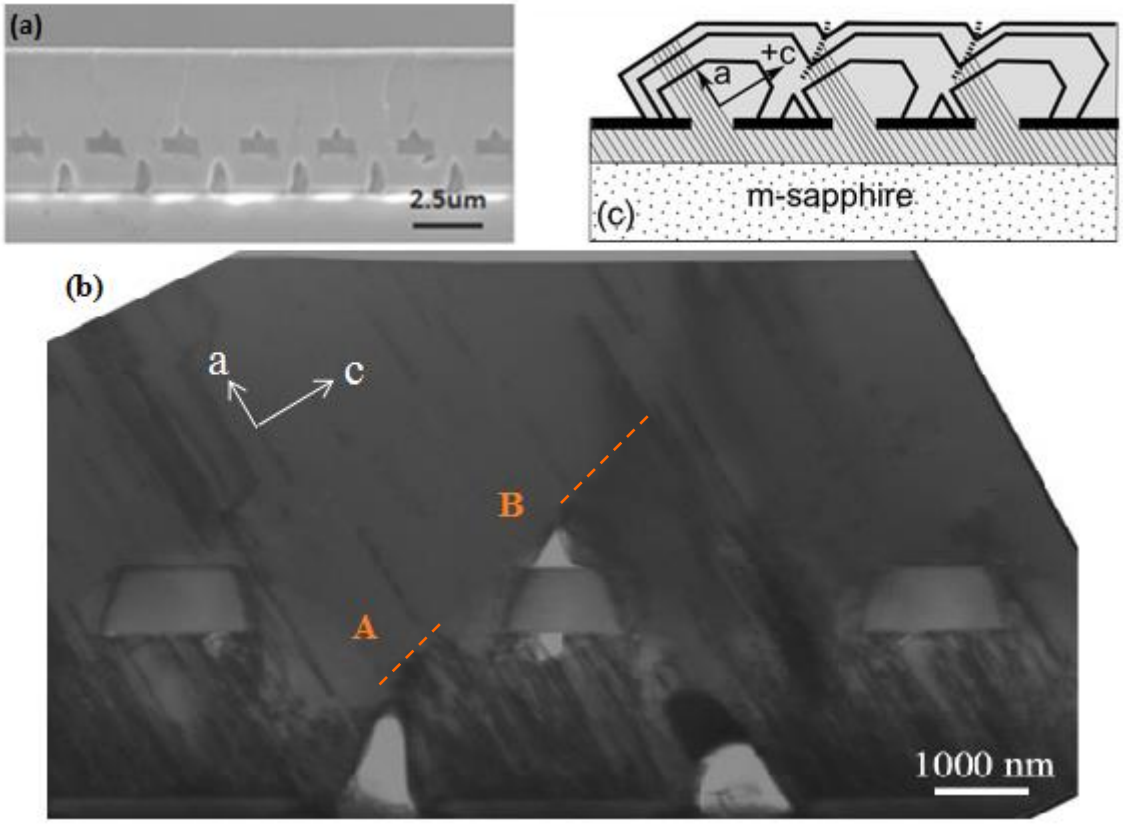

Fig. 6.17: (a) Cross-sectional SEM image, (b) cross-sectional TEM image of the semi-polar GaN on a micro-rod template, and (c) schematic illustration of the GaN overgrowth model, where grey parallel lines represent the BSFs.

Since the lateral growth rate along m ([1-100]) direction is very slow, the major contribution of first coalescence is from the **c** lateral growth and **a** lateral growth. Figure 6.17 (a) shows a cross-sectional SEM image of the overgrown semi-polar GaN observed along [1-100] direction, in which different orientations are highlighted. The total overgrowth time is 7000 sec (~ 4 μm thick overgrown layer), our standard growth time for the overgrowth on semi-polar templates. The larger residue voids are formed between adjacent micro-rods and smaller voids are on top of the SiO_2, both of which result from the lateral growth.

Figure 6.17 (b) shows a cross-sectional TEM image of the semi-polar GaN grown on the micro-rod templates, where **c** and **a** direction are highlighted. The GaN micro-rods fabricated from the as-grown GaN template can be distinguished which all have a high density of defects. Each GaN micro-rod is caped with SiO_2, which effectively prevents the overgrowth initiating from the top part of micro-rods, hence tremendously reducing the defects. In the +**c** wing, the film is free of defects, whilst defects extend into the new film at left side of micro-rods, which is grown along **a** direction. It is in agreement with observation of the

growth at first stage in Fig.6.14. The first coalescence occurs in Region A. Due to the faster growth rate along the **c** direction than **a** direction, the a-facets can be effectively buried by the adjacent +**c** facets, leading to blocking of defects from propagating to the up-growing GaN film. The dashed line represents the coalescence front between the neighbouring **c**-facet and **a**-facet. As the growth progresses, the coalesced crystals extend over the SiO_2 masks and eventually coalescence second time at the dashed lines in Region B. Similar to the first time coalescence, the **a**-facet crystal is buried by the adjacent **c**-facet crystal as well at the second coalescence. Therefore, the +**c** growth rate needs to be fast enough to enable that the **c**-facet crystal can effectively bury the neighbouring **a**-facet crystal.

The mechanism of reduction in the BSFs and related defects is illustrated in Figure 6.17 (c). BSFs are represented by grey parallel lines, which are inclined by ~58^o from the horizontal direction. The +**c** lateral growth leads to the crystal free of defects, while pre-existing BSFs and part of dislocations extend with the +**a** lateral growth. Terminating of the **a**-growth crystal by the adjacent **c**-growth crystal thus blocks the propagation of the BSFs and other defects to the coalesced film. It is worth noting that the process of blocking defects at the coalescence front is involved in both coalescence procedures in our three-stage overgrowth. It leads to an efficient reduction in the extended defects, and hence significant improvement in the crystal quality.

6.4. InGaN/GaN MQWs on Overgrown Semi-polar GaN

6.4.1. InGaN/GaN MQWs with Different Emission Wavelengths

In order to demonstrate good crystal quality of our overgrown semi-polar GaN films, 5 periods of InGaN/GaN MQWs are grown by MOCVD on the semi-polar GaN, as illustrated in a schematic in Figure 6.18(a). A systematic study has been carried out on the MQWs with different long emission wavelengths (from yellow to orange). Figure 6.18(b) is a TEM image of the QWs, showing a well thickness of 3.8nm and a barrier thickness of 5.8 nm.

Note that the MOCVD growth conditions are not optimized for the semi-polar InGaN/GaN MQWs. Figure 6.19 shows PL spectra of semi-polar and c-plane MQW samples grown under identical conditions. It is found that the emission wavelength of the c-plane MQWs is about 460 nm while the semi-polar MQWs emit at ~540 nm. It confirms the report [10] that semi-polar GaN-based quantum wells exhibit a much higher indium incorporation compared

with the QWs grown on c-plane GaN, which can be attributed to the lower indium chemical potential. Due to larger In atoms than Ga atoms, a strain-induced repulsive interaction exists between incorporated In atoms on the surface, which is weaker on the (11-22) surface compared with the c-plane surface [11]. Consequently, indium will incorporate in higher concentrations on the (11-22) surface than on the c-plane surface.

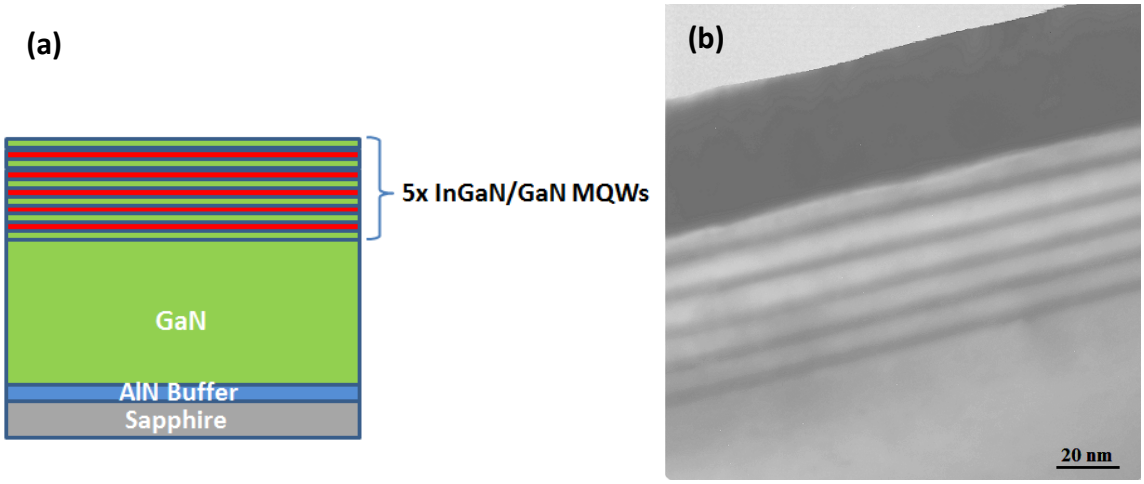

Fig. 6.18: (a) Schematic of an InGaN/GaN MQW sample; (b) TEM image of InGaN/GaN QWs.

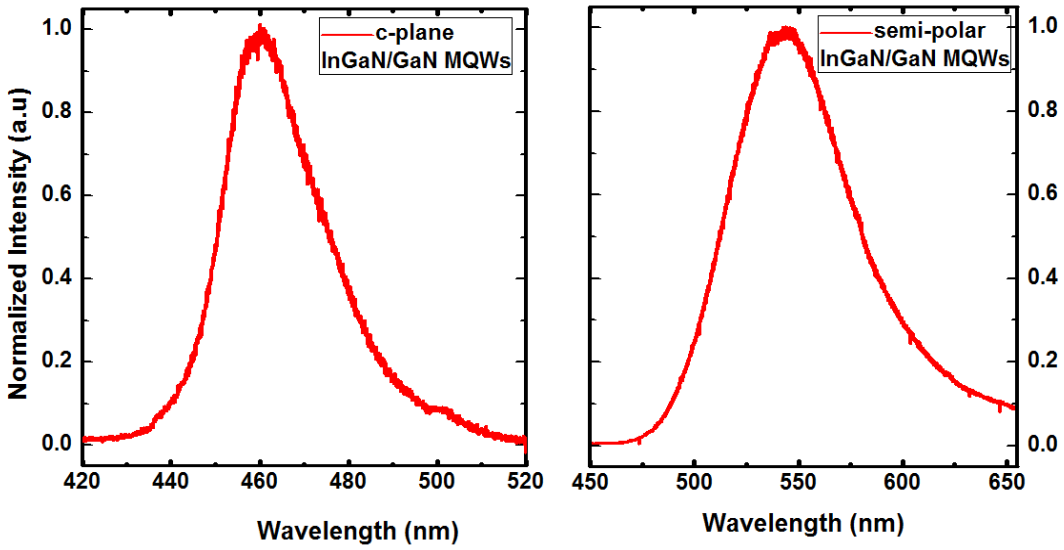

Fig. 6.19: PL spectra of semi-polar and c-plane MQW samples grown under identical conditions.

Figure 6.20 displays room temperature PL spectra of MQWs grown at different temperatures on semi-polar GaN, where a 375 nm diode laser with 10 mW excitation power is used. The PL emission wavelength ranges from ~495 to 590 nm, which is from green to orange on a

spectrum. It is worth mentioning that the PL emission is still very strong even at a long wavelength of 590 nm. This demonstrates excellent crystal quality of our semi-polar overgrown GaN grown on our high quality semi-polar micro-rod template.

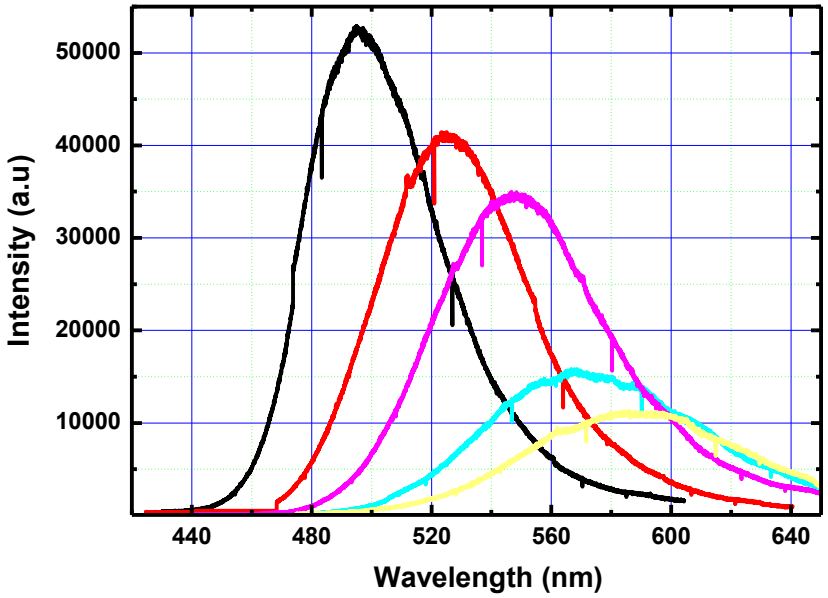

Fig. 6.20: Room temperature PL spectra of MQWs with different emission wavelengths.

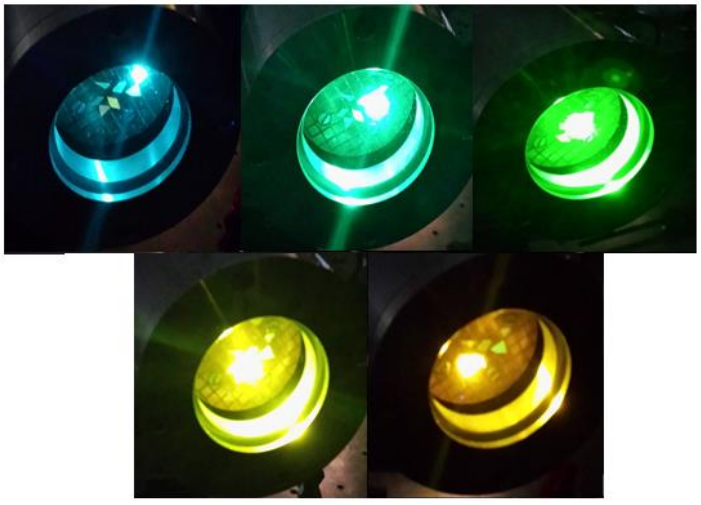

Fig. 6.21: Photos of PL emissions from the InGaN/GaN MQW samples measured at 10K.

The low temperature PL measurements are also performed on these InGaN/GaN MQW samples. All these samples are loaded into a cryostat, in which a high vacuum condition can

be achieved. The temperature in the cryostat can be reduced down to ~10 K. The 375 nm diode laser at 10 mW is used. Figure 6.21 presents the PL emission photos of the samples taken at ~10 K. The emissions with different wavelengths including blue, dark green, bright green, yellow and orange, and with strong emission intensity can be clearly seen. This confirms that our high quality semi-polar GaN is a very good candidate for fabrication of the nitride-based LEDs, especially for green and yellow spectrum region, which are great challenges for the present optical emitters.

6.4.2. QCSE and Internal Quantum Efficiency

As expounded in Chapter 2, there exists a large internal electrical field in InGaN/GaN MQWs, which is induced by the large lattice mismatch. This electric field causes the tilting of the energy band of the QWs and results in lower probability of the radiative recombination of electrons and holes. The band tilting will give rise to a red-shift in the emission wavelength. All these phenomena are defined as the quantum confined Stark effect (QCSE). As a result, internal quantum efficiency (IQE) and optical efficiency are hence reduced. Due to higher indium concentration in the QWs, it is becoming worse when the emission is moving toward longer wavelength such as green or yellow spectral region, generating so-called “green gap” phenomenon.

To investigate whether the semi-polar GaN MQWs are partially free of QCSE, excitation power dependent PL experiments are performed by measuring PL spectra at different laser powers. A blue shift in the emission energy with increasing the excitation power is a fingerprint of QCSE in the sample, as high excitation power would mitigate the effect of the energy band bending caused by the QCSE. Figure 6.22 shows PL spectra measured at excitation powers ranging from 0.1 mW to 15 mW, for four InGaN/GaN MQW samples with wavelengths at 492 nm, 510 nm, 532 nm and 564 nm, respectively. With increase of the excitation power by a factor of 150, a shift in the emission wavelength is observed for all the samples, showing that QCSE still exists in the semi-polar QW samples.

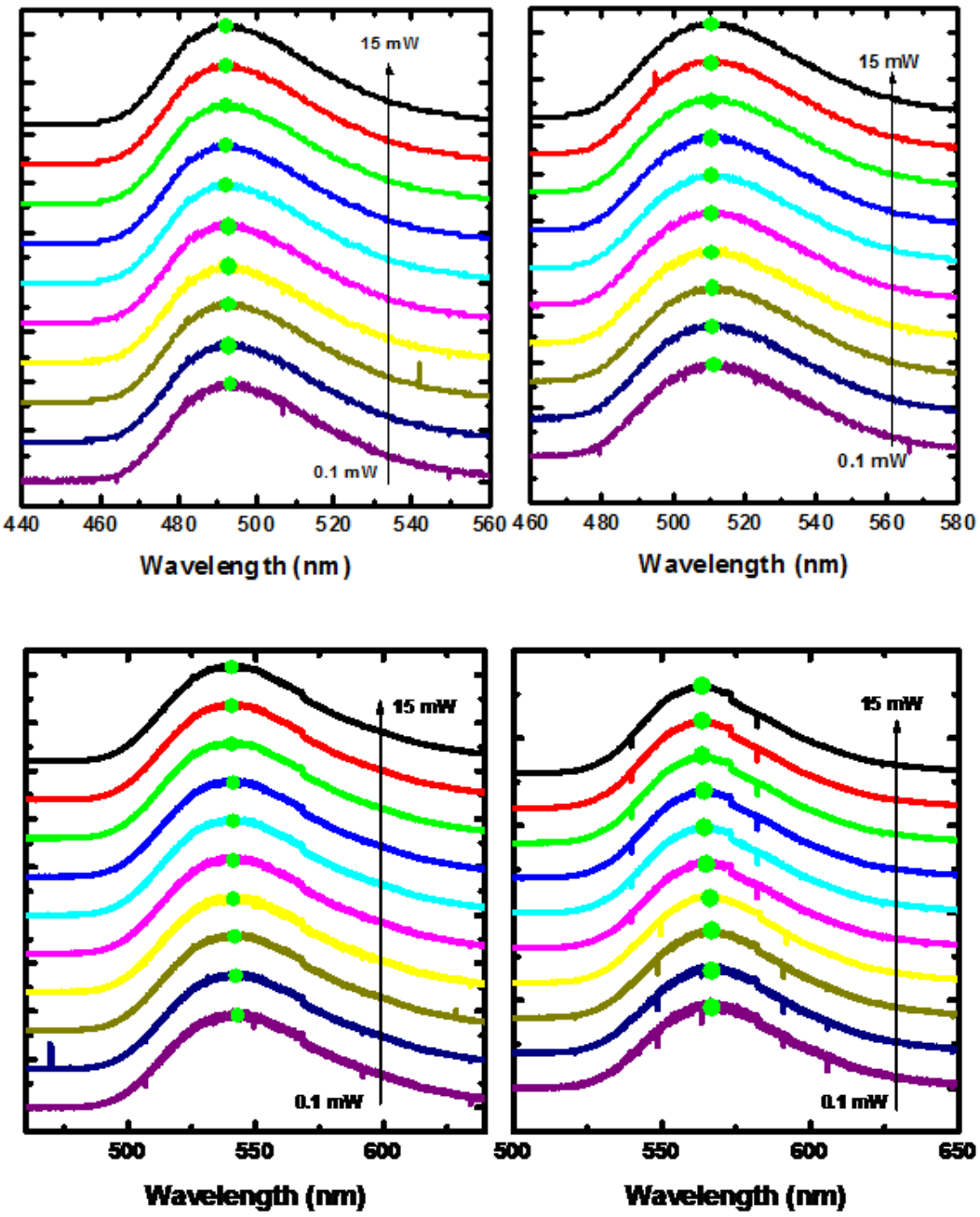

Fig. 6.22: PL Spectra measured at excitation powers ranging from 0.1 mW to 15 mW, for semi-polar InGaN/GaN MQWs with emission wavelengths at 492 nm, 510 nm, 532 nm, and 574 nm, respectively.

Figure 6.23 lists the wavelength shift as a function of excitation power for a series of QW samples with different emission wavelengths. It can be found that the shift becomes larger with increase of the emission wavelength, indicating stronger QCSE for longer wavelength. This is because the strain-induced internal electronic field in the QWs is increased due to larger lattice mismatch for InGaN/GaN QWs with longer wavelengths. According to a

summary in Figure 6.24, with increasing power by a factor of 100, the blue shifts are only 1-4 nm for the MQWs from green to orange emission, which are relatively quite small in comparison with c-plane QW samples. It confirms that the QCSEs in our overgrown semi-polar InGaN/GaN MQWs are very weak.

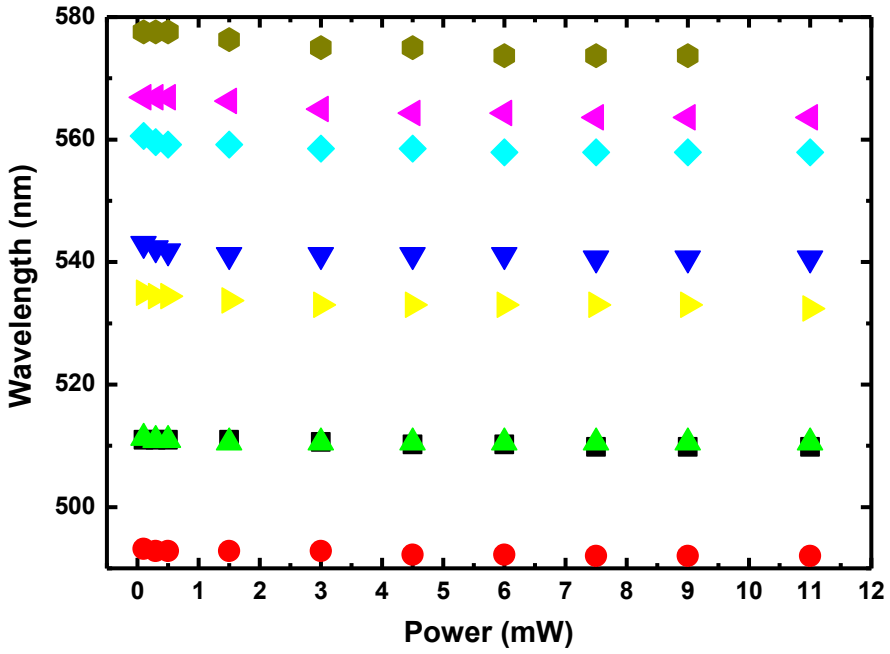

Fig. 6.23: The wavelength shift as a function of excitation power for each InGaN/GaN MQW sample.

	Wavelength shift 1.7E4 – 1.6E2 mW/cm²
Green to Orange	492.0-493.2 (1.2nm)
	509.8-511.0 (1.2nm)
	510.5-511.3 (0.8nm)
	532.4-535.0 (2.6nm)
	540.6-543.0 (2.4nm)
	557.9-560.6 (2.7nm)
	563.9-566.3 (2.7nm)
	573.7-577.6 (3.9nm)

Fig. 6.24: Summary of wavelength shifts for each sample from green to orange spectrum.

As discussed above, the internal electrical field induced QCSE in InGaN/GaN MQWs causes a significant reduction in optical efficiency especially when optical emitters are moving toward longer wavelength such as green and yellow spectral region. In order to estimate the internal quantum efficiency (IQE), the temperature dependent PL measurements are performed on all the InGaN MQW samples. The IQE at room temperature (300K) can be roughly estimated if it is assumed to be 100% at 10K, a standard and commonly used approach. Figure 6.25(a), 6.26(a), 6.27 (a) and 6.28(a) show PL spectra measured at different temperature ranging from 10 to 300K, while Figure 6.25(b), 6.26(b), 6.27(b) and 6.28(b) show Arrhenius plots of normalized integrated intensity as a function of the temperature from 10 to 300K. The IQEs for samples with emission wavelengths at 492 nm, 510 nm, 532 nm and 564 nm are estimated to be 10%, 9.6%, 9.3% and 8%, respectively. Though the IQE slightly decreases with the increase of emission wavelength due to the increased QCSE, the IQE values remain around 10% within green and yellow spectrum region. It indicate that our high quality semi-polar GaN is a very promising approach to achieve high efficiency optical emitters in green and yellow spectrum range.

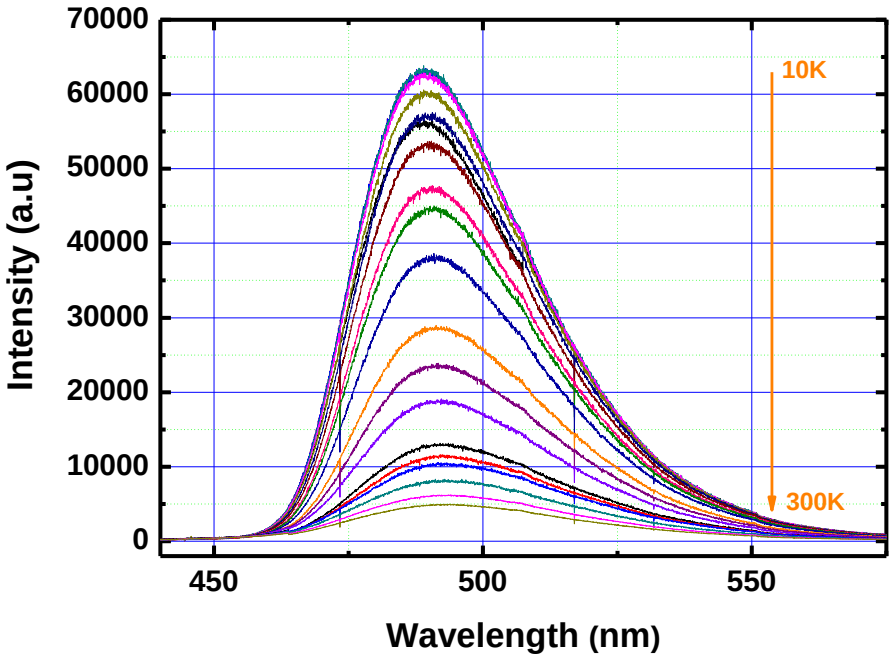

Fig. 6.25 (a): PL spectra of the sample measured at temperature ranging from 10 to 300K for InGaN/GaN MQWs with emission wavelength at 492 nm.

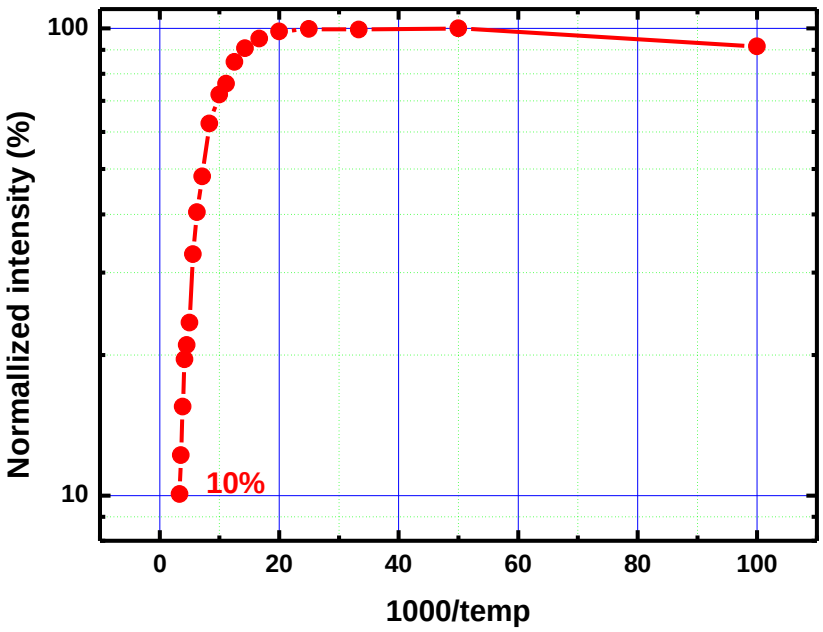

Fig. 6.25 (b): Arrhenius plot of the normalized integrated intensity as a function of the temperature from 10 to 300K, for InGaN/GaN MQWs with emission wavelength at 492 nm.

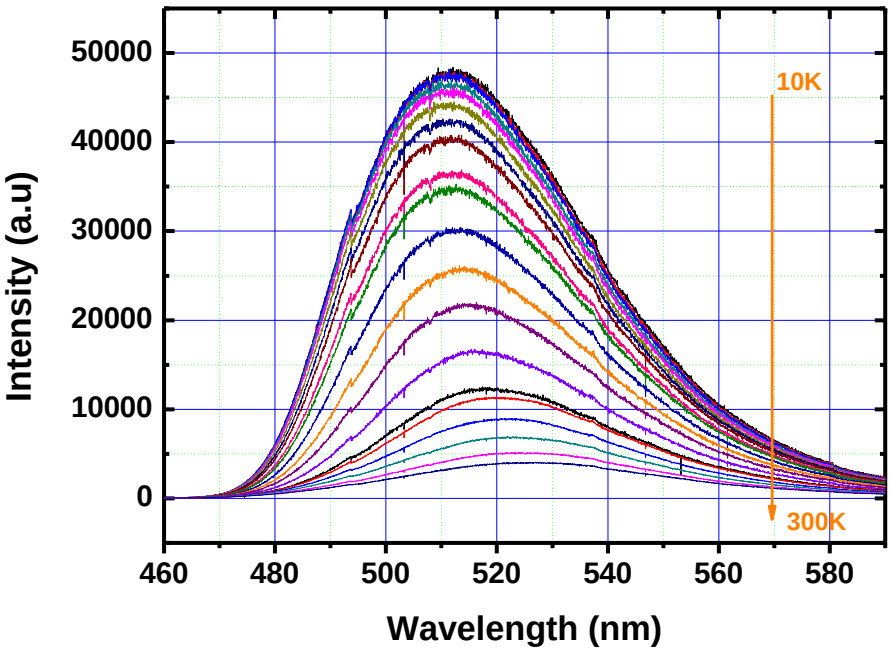

Fig. 6.26 (a): PL spectra of the sample measured at temperature ranging from 10 to 300K for InGaN/GaN MQWs with emission wavelength at 510 nm.

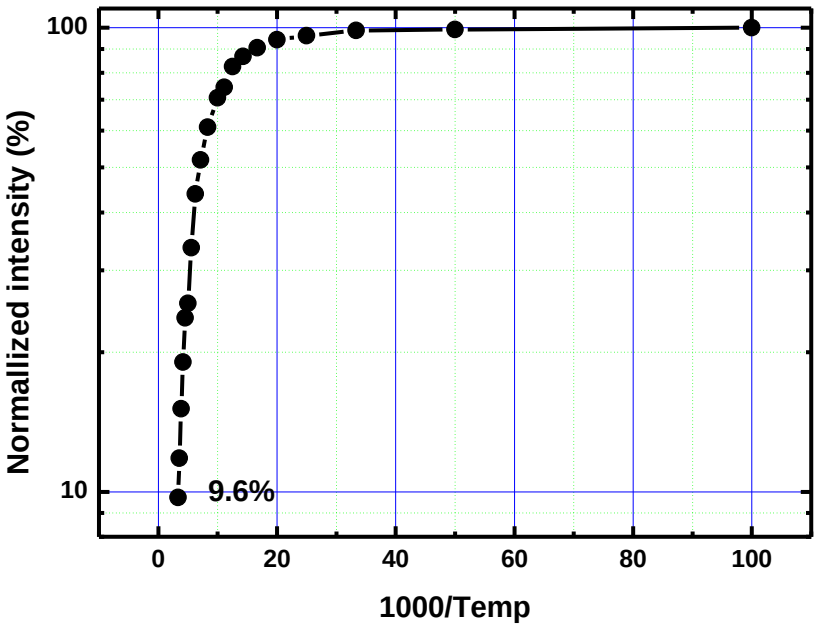

Fig. 6.26 (b): Arrhenius plot of the normalized integrated intensity as a function of the temperature from 10 to 300K, for InGaN/GaN MQWs with emission wavelength at 510 nm.

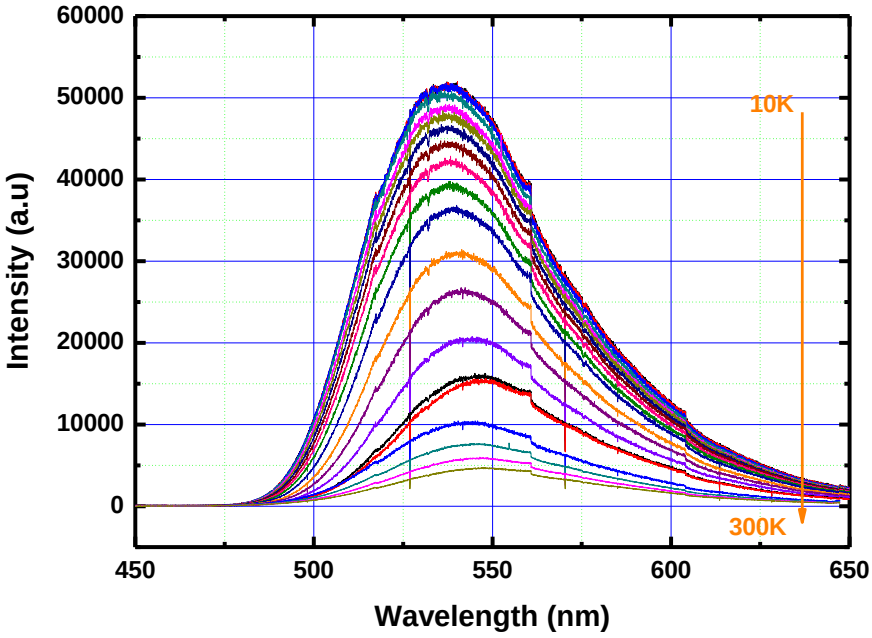

Fig. 6.27 (a): PL spectra of the sample measured at temperature ranging from 10 to 300K for InGaN/GaN MQWs with emission wavelength at 532 nm.

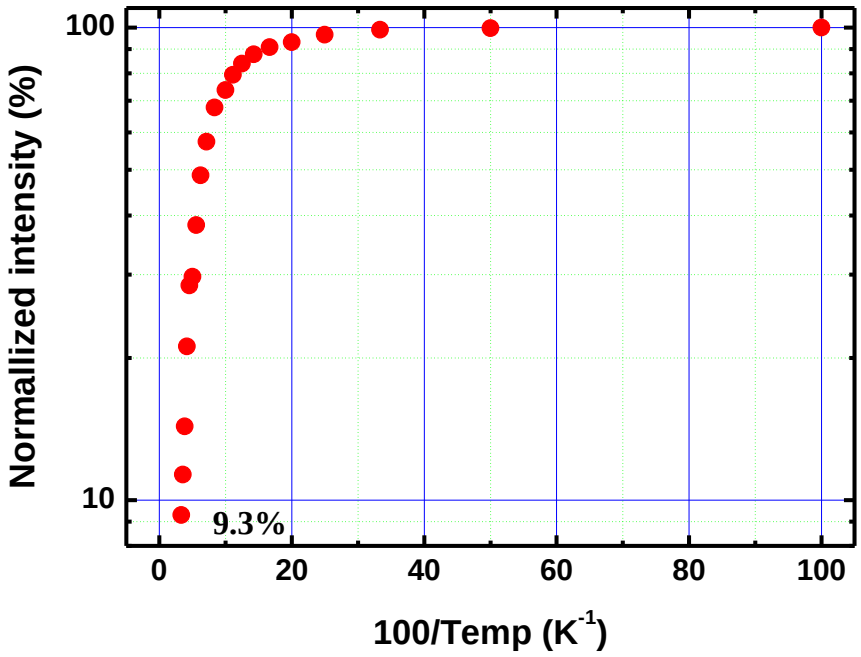

Fig. 6.27 (b): Arrhenius plot of the normalized integrated intensity as a function of the temperature from 10 to 300K, for InGaN/GaN MQWs with emission wavelength at 532 nm.

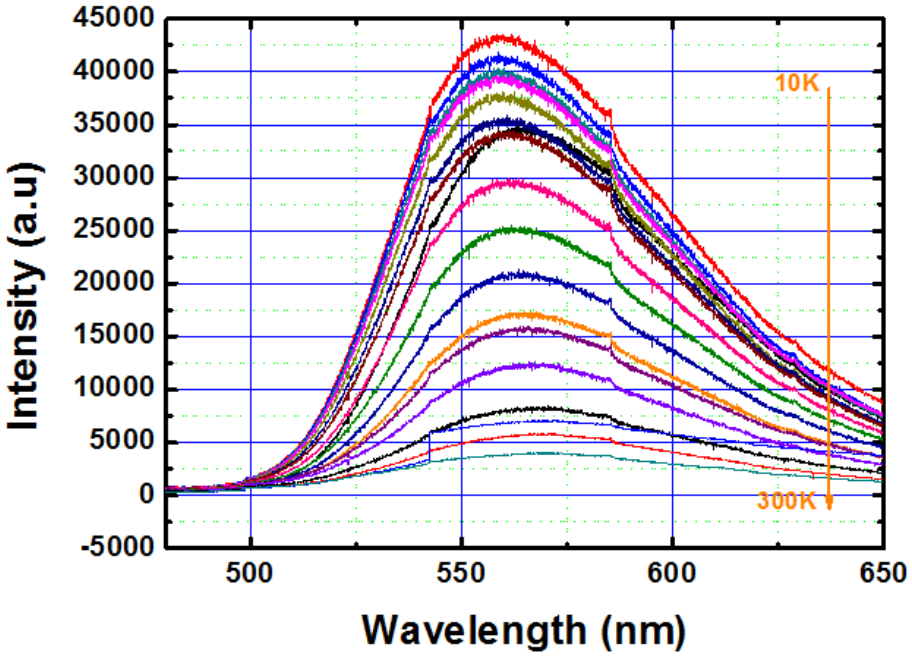

Fig. 6.28 (a): PL spectra of the sample measured at temperature ranging from 10 to 300K for InGaN/GaN MQWs with emission wavelength at 564 nm.

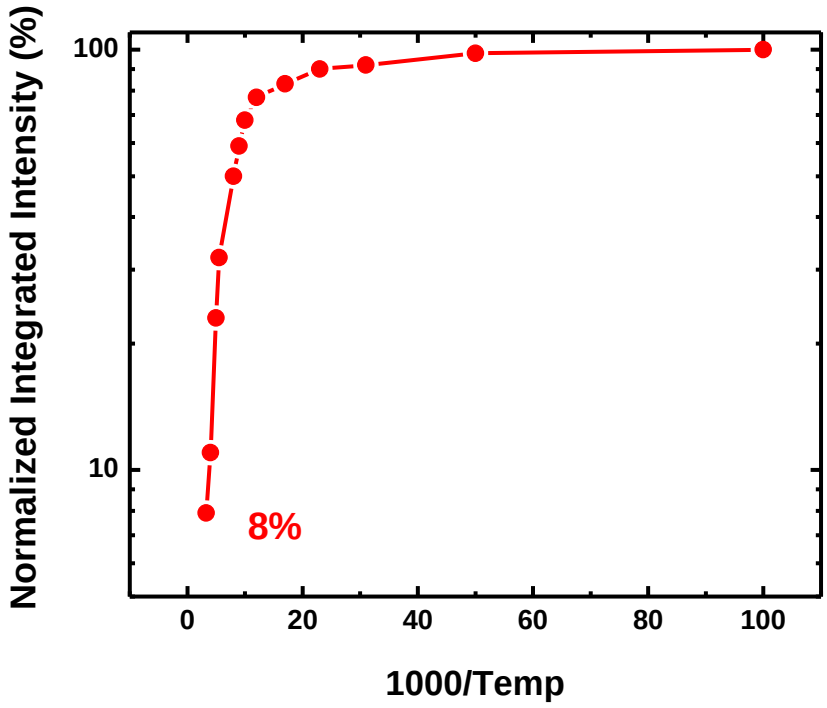

Fig. 6.28 (b): Arrhenius plot of the normalized integrated intensity as a function of the temperature from 10 to 300K, for InGaN/GaN MQWs with emission wavelength at 564 nm.

6.5. Conclusions

High quality semi-polar GaN films has been achieved by the overgrowth on micro-rod templates, which are fabricated using UV lithography as described in section 4.3. Due to anisotropic growth rate, the pattern orientation plays an important role in the overgrowth of semi-polar GaN. The crystal quality of semi-polar GaN films improves with increasing the micro-rod size. SEM and AFM images show flat and smooth surface of samples, which are achieved by an overgrowth within 4-5 μm thickness. After a series of optimization experiments, XRD results are among the best reports of semi-polar GaN achieved using ELOG approaches, and a good uniformity in the crystal quality across 2-inch wafer has been demonstrated. PL measurements at 10K show a very strong band emission with intensity of 2.8 times compared to the BSF-related emission, indicating the defects are significantly reduced due to the overgrowth on micro-rod templates. Moreover, the mechanism of defect reduction is discussed in detail through TEM and SEM observations on a series of samples

grown with 1000 sec, 2000 sec and 3000 sec. Furthermore, InGaN/GaN MQWs are grown on the high quality semi-polar GaN films, which emission wavelength ranges from green to orange in the spectrum. Experiments of excitation power dependent PL and temperature dependent PL are carried out to investigate QCSEs and IQEs in these QW samples. It is found that the QCSE becomes stronger and the IQE is slightly reduced with increase of emission wavelength. However, the QCSEs are confirmed to be very weak and the IQE remains around 10% even for the semi-polar MQWs with orange emission. It indicates that our approach to achieve high quality semi-polar GaN is a very promising technology to realize high efficiency optical emitters in the visible spectrum of longer wavelengths.

References

1. M.D. Craven, S.H. Lim, F. Wu, J.S. Speck, and S.P. DenBaars, Appl. Phys. Lett. **81**, 1201 (2002).
2. B. A. Haskell, F. Wu, M. D. Craven, S. Matsyda, P. T. Fini, T. Fujii, K. Fujito, S. P. DenBaars, J. S. Speck, and S. Nakamura, Appl. Phys. Lett. **83**, 644 (2003).
3. C. Chen, J. Zhang, J. Yang, V. Adivarhan, S. Rai, S. Wu, H. Wang, W. Sun, M. Su, Z. Gong, E. Kuokstis, M. Gaevski, and M.A. Khan, Jpn. J. Appl. Phys. **42**, L818 (2003).
4. K. Linthicum, T. Gehrke, D. Thomson, E. Carlson, P. Rajagopal, T. Smith, D. Batchelor, and R. F. Davis, Appl. Phys. Lett. **75**, 196 (1999).
5. T. S. Zheleva, S. A. Smith, D. B. Thomson, K. J. Linthicum, P. Rajagopal, R. F. Davis, J. Electron. Mater. **28**, L5 (1999).
6. B. Imer, F. Wu, S. P. DenBaars, and J. S. Speck, Appl. Phys. Lett. **88**, 061908 (2006).
7. P. Corfdir, P. Lefebvre, J. Levrat, A. Dussaigne, J.-D. Ganière, D. Martin, J. Ristić, T. Zhu, N. Grandjean, and B. Deveaud-Plédran, J. Appl. Phys. **105**, 043102 (2009);
8. P. de Mierry, N. Kriouche, M. Nemoz, and G. Nataf, Appl. Phys. Lett. **94**, 191903 (2009).
9. R. Liu, A. Bell, F. A. Ponce, C. Q. Chen, J. W. Yang, and M. A. Kahn, Appl. Phys. Lett. **86**, 021908 (2005).
10. Y. Narukawa, M. Ichikawa, D. Sanga, M. Sano, and T. Mukai, J. Phys. D: Appl. Phys. **43**, 354002 (2010).
11. J. E. Northrup, Appl. Phys. Lett. **95**, 133107 (2009).

Chapter 7

Conclusion and Future Work

7.1. Conclusion

In this work, two simple but cost-effective approaches for fabrication of nano-rod and micro-rod arrays on non-polar/semi-polar GaN templates grown on sapphire have been developed, which are fabricated based on the self-organized nano-masks and UV lithography approaches, respectively. Both the nano-rod and micro-rod arrays with good uniformity, high reproducibility and accurately controlled size have been achieved.

For the self-organized approach, the insertion of the Au film has greatly improved the shape, uniformity and reproducibility of the Ni masks. The overgrowth of GaN has been performed on the semi-polar and non-polar GaN nano-rod arrays by MOCVD, leading to great improvement in crystal quality. This is confirmed by XRD rocking curve and TEM measurements. In addition, a quick coalescence of GaN with only ~1μm is achieved, and a smooth surface morphology has been obtained with a 4-5um overgrown layer. The size of the self-organized nano-masks has been successfully controlled by varying the Ni layer thickness, and the systematic study of the dislocation density as a function of the mask size has been performed. It has been found that with the increase of the mask size, the crystal quality of the overgrown film improves tremendously. The mechanism for defect reduction in the non-polar/semi-polar GaN overgrown on nano-rod templates has been investigated by TEM studies in detail. The overgrowth initiates from the sidewalls of the GaN nano-rods, which reduces dislocations density due to the line bending in basal planes and the BSF because of the priority [0001] growth. InGaN/GaN MQWs have been grown on the high-quality semi-polar and non-polar overgrown GaN. The temperature dependent PL measurements demonstrate a huge improvement in the IQE compared with that grown on the non-polar/semi-polar as-grown templates, due to the massive reduction in the extended defects. Excitation power dependent PL measurement has demonstrated that non-polar InGaN/GaN MQWs are free of QCSE, and the QCSE in the semi-polar InGaN/GaN MQWs is significantly reduced.

The micro-rod array template based on photolithography technique is evolved from the self-organized nano-rod template and can achieve a larger pattern size and better uniformity. Therefore, compared to the overgrowth based on self-organized nano-rod template, the photolithography approach leads to further reduction of the extended defects. Micro-rod arrays with different sizes (1.5 μm, 2.5 μm and 3 μm) have been successfully fabricated on as-grown semi-polar GaN, which serves as the templates for GaN overgrowth. It has been demonstrated that with increasing micro-rod diameter both the dislocation density and basal stacking faults have been reduced dramatically. The mechanism of the defect reduction of the micro-rod overgrowth is investigated by TEM. The reduction of the dislocations is through two main pathways: dislocation annihilation due to line bending in the basal plane; and termination of dislocations at the free surfaces by voids and SiO_2 masks. The BSF has been also significantly reduced owing to the fast [0001] growth, terminating the BSF from penetrating to the overlying structure. InGaN/GaN MQWs with high indium composition have been grown on the high quality overgrown GaN samples, leading to high intensity PL emission ranging from green to orange. It has been found that the IQE is slightly reduced with the increase of emission wavelength, but the IQE remains around 10% even for the semi-polar MQWs with orange emission. This demonstrates that our semi-polar GaN overgrown approach is a good candidate for realizing high performance optical emitters in long wavelength spectral region.

7.2. Future Work

7.2.1. GaN Overgrowth Using Different Masks

A detailed study of the GaN overgrowth on 2-inch semi-polar micro-rod arrays with respect to different pattern sizes (1.5um, 2um and 3um) has been performed in Chapter 6. It has been demonstrated that the dislocations and basal stacking faults of the overgrown GaN can be reduced with increasing the nano-rod size, due to decrease in the number of the coalescence regions [1]. Therefore, micro-rod arrays masks with larger pattern sizes (e.g. 3.5um, 4um, and 4.5um etc.) are designed for fabrication of the GaN micro-rod templates, in order to further improve the crystal quality.

Moreover, different mask patterns for fabrication of the micro-rod arrays are also designed aiming to investigate the extended defects, which are shown in Figure 7.1. Figure 7.1 (a) shows the circular array with the same circle size (3um) but reduced gap (3um → 1um) as the original mask pattern. This may further improve the crystal quality since the dislocations are mainly reduced in the wing region (over the SiO_2 mask region) [2]. Figure 7.1 (b) is the striped feature and its window and wing width are both 3um. The mask is aligned such that the projection of c/a-axis GaN is perpendicular to the stripe. This is designed so that the GaN growth along m direction can be effectively avoided and the growth is only initiated from the preferred c and a directions.

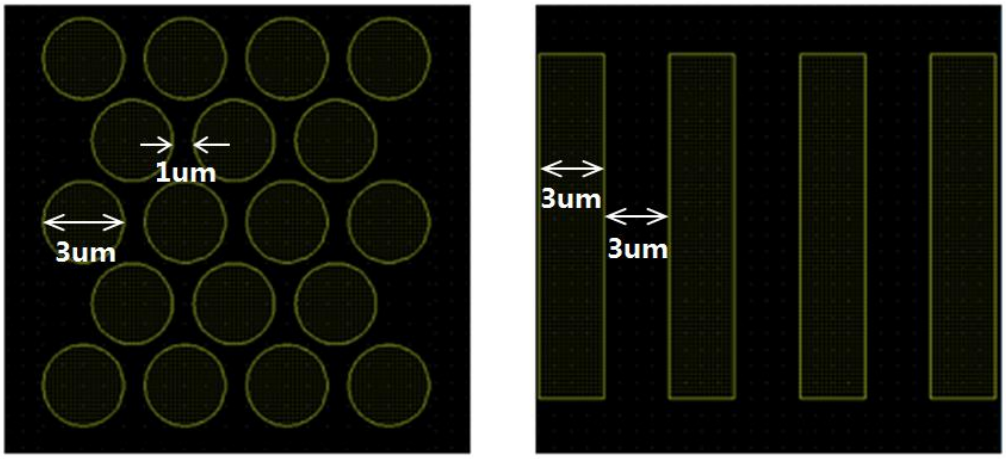

Fig. 7.1: (a) modified circular array mask pattern, and (b) striped pattern for micro-structure fabrication.

7.2.2. Semi-polar InGaN/GaN MQW LEDs

When device-quality GaN is achieved, LED structures will be grown on it by means of MOCVD targeting to achieve high optical performances LEDs emitting at longer wavelength in the visible spectral range. The schematic diagram of the GaN LED structure is illustrated in Figure 7.2. The n-type (Si doped) GaN is directly grown on our high quality GaN film by MOCVD. The p-type GaN is Mg doped and the active InGaN/GaN quantum well layer is sandwiched between n- and p-type GaN. When the LED structure is grown, the p-type

contact is deposited and the sample is etched by ICP so that n-type GaN is exposed in order to make n-contacts.

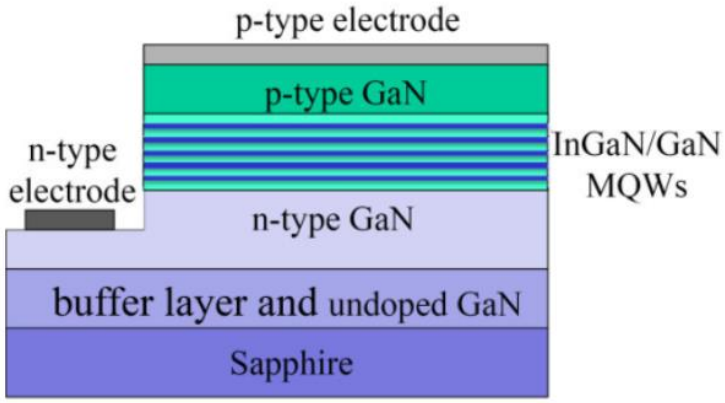

Fig. 7.2: Schematic structure of InGaN/GaN MQW LEDs [3].

7.2.3. Switching to Larger Sapphire Substrates

The most competitive substrate for growth of GaN wafers is the sapphire substrate due to its low price, good chemical and thermal stability. Over recent years, the upstream LED chip manufacturers are gradually switching from 2-inch to 4 and 6-inch sapphire wafer in order to achieve mass production. This is expected to lead to 20%-30% on cost reduction compared with that using 2-inch sapphire [4], since the sapphire substrate prices have reduced while sapphire material remains stable.

References

1. D. Iida, M. Iwaya, S. Kamiyama, H. Amano, and I. Akasaki, J. Cryst. Growth **311**, 2887 (2009).
2. B. M. Imer, F. Wu, S. P. DenBaars, and J. S. Speck, Appl. Phys. Lett. 88, 061908 (2006).
3. http://openi.nlm.nih.gov/detailedresult.php?img=3442964_1556-276X-7-282-1&req=4
4. http://www.ledinside.com/news/2014/1/manufacturers_move_towards_4_inch_led_wafer_production_in_2014